DISCOVERY POTENTIAL OF QUANTUM BLACK HOLES IN ADD MODEL WITH THE CMS DETECTOR

A THESIS SUBMITTED TO
THE GRADUATE SCHOOL OF NATURAL AND APPLIED SCIENCES
OF
MIDDLE EAST TECHNICAL UNIVERSITY

BY

HALİL GAMSIZKAN

IN PARTIAL FULFILLMENT OF THE REQUIREMENTS
FOR
THE DEGREE OF DOCTOR OF PHILOSOPHY
IN
PHYSICS

AUGUST 2011

Approval of the thesis:

DISCOVERY POTENTIAL OF QUANTUM BLACK HOLES IN ADD MODEL WITH THE CMS DETECTOR

submitted by **HALİL GAMSIZKAN** in partial fulfillment of the requirements for the degree of
Doctor of Philosophy in Physics Department, Middle East Technical University by,

Prof. Dr. Canan Özgen
Dean, Graduate School of **Natural and Applied Sciences**

Sinan Bilikmen
Head of Department, **Physics**

Prof. Dr. Meltem Serin
Supervisor, **Physics Department**

Examining Committee Members:

Prof. Dr. Ali Ulvi Yılmazer
AÜ, Eng. Physics

Prof. Dr. Meltem Serin
METU, Physics

Prof. Dr. Mehmet Zeyrek
METU, Physics

Prof. Dr. Müge Boz
Hacettepe Ü., Eng. Physics

Prof. Dr. Altuğ Özpineci
METU, Physics

Date:

I hereby declare that all information in this document has been obtained and presented in accordance with academic rules and ethical conduct. I also declare that, as required by these rules and conduct, I have fully cited and referenced all material and results that are not original to this work.

Name, Last Name: HALİL GAMSIZKAN

Signature :

ABSTRACT

DISCOVERY POTENTIAL OF QUANTUM BLACK HOLES IN ADD MODEL WITH THE CMS DETECTOR

Gamsızkan, Halil
Ph.D., Department of Physics
Supervisor : Prof. Dr. Meltem Serin

August 2011, 120 pages

With the long awaited start-up of the LHC, TeV scale physics is now in reach of the particles physicists to explore. There are many questions about the nature to be answered, and many more theories to be tested trying to answer them.

The ADD model of extra dimensions is one such model, written to address the large mass hierarchy between the two fundamental energy scales in nature, the electroweak and the Planck scales. ADD model predicts stronger gravity at sub-millimeter distance scales, which would then lead to an interesting physical object to be produced at proton collusions at the LHC: Tiny quantum black holes.

In this thesis we study the discovery potential of CMS for quantum black hole events for proton-proton collusions at $\sqrt{s} = 14$ TeV. Our study details the trigger response of CMS, various criteria and methods for background rejection, affect of experimental uncertainties on measurements, for different model parameter values.

Keywords: ADD Model, Extra Dimensions, Black Holes, CMS, LHC

ÖZ

ADD MODELİ KUANTUM KARA DELİKLERİN CMS DEDEKTÖRÜ İLE KEŞFEDİLME POTANSİYELİ

Gamsızkan, Halil
Doktora, Fizik Bölümü
Tez Yöneticisi : Prof. Dr. Meltem Serin

Ağustos 2011, 120 sayfa

LHC'nin uzun süredir beklenen açılışıyla, TeV enerjilerinde fizik yapmak artık parçacık fizikçileri için mümkün hale gelmiş bulunuyor. Doğa'ya dair cevaplanması gereken pek çok soru, ve bu sorulara verdikleri cevapların sınanması gereken daha da çok kuram bulunuyor.

ADD ek boyut modeli de bu kuramlardan biri olup doğadaki bilinen iki temel enerji ölçeği –elektrozayıf ve Planck ölçekleri– arasındaki büyük farkı açıklayabilmek amacıyla yazılmıştır. ADD modelinin milimetre'den küçük mesafelerde kütleçekim kuvvetinin güçlendiği varsayımı LHC'deki proton çarpışmalarında ilginç bir fiziksel nesnenin üretimi sonucunu beraberinde getirir, yani kuantum kara deliklerin.

Bu tezde $\sqrt{s} = 14$ TeV enerjide proton-proton çarpışmaları için CMS dedektörünün kuantum kara delik olaylarını keşif potansiyeli çalışılmıştır. Çalışmamız farklı model parametresi değerleri için CMS tetikleyicisinin davranışı, fon olaylarının reddedilmesi için çeşitli kriter ve yöntemler, deneysel belirsizliklerin ölçümlere etkisi gibi başlıkları kapsar.

Anahtar Kelimeler: ADD Modeli, Ek boyutlar, Kara delikler, CMS, LHC

Aileme ve tüm sevdiklerime ithaf olunur..

ACKNOWLEDGMENTS

This thesis wouldn't exist without the help and support of many people, including Mehmet Zeyrek, Albert de Roeck, Meltem Serin, Sezen usta, Çiğdem Kanberoğlu and the CMS collaboration, both past and present members. Thank you, each and every one of you.

I also would like to thank METU Department of Physics for their support in my studies, TAEK for supporting my visits at CERN, CERN for being a home, a school and an excellent place to do research, and the METU NCC campus for being the most welcome and quiet home in the final stage of my thesis studies.

Pek çok insanın katkısı olmadan bu tez ortaya çıkamazdı; bunlardan en önemlileri Meltem Serin, Mehmet Zeyrek, Albert de Roeck, Sezen usta, Çiğdem Kanberoğlu, ve CMS kolaborasyonunda bulunan ve bulunmuş kişilerdir. Her birinize ayrı ayrı teşekkür ederim.

Ayrıca çalışmalarıma verdikleri destek için ODTÜ Fizik Bölümüne, yine desteğiyle CERN ziyaretlerimi mümkün kılan TAEK'e, hem bir ev, hem bir okul hem de kusursuz bir araştırma ortamı sağladığı için CERN'e, ve tez çalışmalarımın son aşamalarını gerçekleştirirken bana samimi ve huzurlu bir ortam sağlayan ODTÜ KKK'ya teşekkürü bir borç bilirim.

TABLE OF CONTENTS

LIST OF TABLES

TABLES

LIST OF FIGURES

FIGURES

CHAPTER 1

STANDARD MODEL, AND BEYOND

20^{th} century particle physicist has witnessed many exciting discoveries about the nature of space-time and watched a far from boring subatomic world unfold with it's many mysteries before them. There have been many attempts to completely describe the universe in the most fundamental way. They all have failed for one reason or another, yet they still did broaden our perspectives and inspired our further studies.

As of the 2010's, the picture as we see the subatomic universe is as follows. A seemingly complete set of elementary particles have been discovered. Concerning the dynamics of interactions, very powerful tools have been developed (Gauge principle) and the very successful theory of Quantum Electrodynamics (QED) has been formulated, which is also a unified theory of electromagnetic and weak interactions. QED also served as a basis for writing theories for other interactions like Quantum Chromodynamics (QCD). Quick summaries of the particle content, interactions and symmetries of the standard model (SM) can be seen on Fig.1.1(a), Fig 1.1(b) and Table 1.1.

Electroweak (EWK) theory led to a great excitement perhaps mostly with correctly predicting the existence of the neutral and massive Z boson, even with it's mass. It's widely accepted that the mass terms of massive bosons in the Lagrangian of EWK theory have been generated with their interaction with the Higgs field and the "spontaneous symmetry breaking" mechanism. Quanta of the Higgs field, the Higgs particle, has eluded all the searches at Tevatron, and the first fb^{-1} data of the LHC [2, 3]. It would be fair to say that discovering the Higgs particle is currently the highest priority task of experimental physicists.

The standard model is very successful, but it's still a theory of "almost everything"; for it has it's problems and missing pieces too. The major shortcomings and problems of the SM can be listed as follows:

- There are 29 numerical constants (most of them being the fermion masses) in SM that cannot be calculated from first principles.
- SM has shortcomings in the cosmology sector: The apparent matter-antimatter imbalance in the universe, the nature of dark matter and dark energy cannot be explained within SM.
- Standard model has no successful field theory of gravitational interaction, or any unification schemes between gravity and other fundamental interactions.
- Existence of two largely different energy scales, with a huge desert of new physics in between; namely the hierarchy problem.

Among these shortcomings, the hierarchy problem is the starting point for this thesis study.

1.1 Hierarchy of Scales

According to the SM, nature seems to have two distinct fundamental energy scales. First is the Planck scale

$$M_{\mathrm{Pl}} = G^{-1/2} = 1.2 \times 10^{16}\ \mathrm{TeV} \tag{1.1}$$

where G is Newton's constant[1,2]. Obviously the large value of M_{Pl} is a direct consequence of gravity being a very weak force compared to the other fundamental forces.

The second fundamental energy scale in the nature is the electroweak (EWK) scale, $M_{\mathrm{EW}} \sim 1$ TeV, which is the characteristic energy scale of EWK interactions.

At this point two questions may be raised:

1. Why is there a huge hierarchy ($M_{\mathrm{Pl}}/M_{\mathrm{EW}} \sim 10^{16}$) between two physical energy scales? Stated another way, why is gravity so much weaker than EWK interactions?

---

[1] This value is also the energy equivalent of Planck mass $m_p = 2.2 \times 10^{-8}$ kg, or the energy of a photon whose wavelength is the Planck length $l_p = 1.6 \times 10^{-35}$ m. Such a photon would immediately become a black hole, rendering it impossible to probe a distance this small.

[2] We'll be using Planck units throughout the thesis. In this system of units the speed of light c, the Planck constant $\hbar$ and the Boltzmann constant k_{B} are taken to be unity: $c = \hbar = k_{\mathrm{B}} = 1$

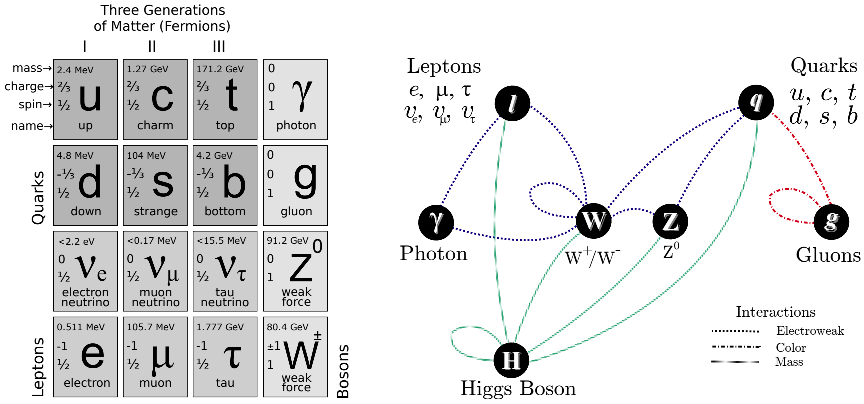

(a) (b)

Figure 1.1: (a) Particle content, and (b) interactions of the standard model [1]. The known elementary particles are split into three categories: leptons, quarks and bosons. Both leptons and quarks have a three family pattern. Lepton families consist of a charged lepton and the corresponding neutrino. Quark families consist of two quarks of different mass, flavor and charge. Each quark and lepton family is the former one's copy, only heavier. Leptons and quarks are fermions with spin 1/2. Concerning the bosons, there is the (to be discovered) spin zero Higgs particle, and three spin one particles which are also interaction mediators. Among the interaction mediators, gluon and photon are massless, while $W^{\pm}$ and Z^0 bosons are massive, and only $W^{\pm}$ carries electric charge. Charged particles undergo electromagnetic interaction, which is mediated by photons. Quarks and gluons undergo strong interaction, which is mediated by gluons. All particles can interact weakly (some weak interactions of Z^0 have been omitted in (b) for simplicity), but only charged particles (and the neutrinos as the third element of the interaction vertex) interact via the charged $W^{\pm}$ bosons because these bosons mediate charge during the interaction.

2. Why are there two distinct energy scales in the nature anyways?

These questions, especially the first one is linked with an open problem in Higgs physics.

In the SM, electroweak symmetry is a broken symmetry, and the Higgs mechanism is responsible for the symmetry breaking. According to this mechanism there's a complex scalar field having nonzero vacuum expectation value (VEV), which is the Higgs field. All massive particles except the Higgs boson acquire mass by interacting with this field.

The Higgs potential is written as (see Fig. 1.2)

$$V = m_{\mathrm{H}}^2|H|^2 + \lambda|H|^4, \tag{1.2}$$

where m_{H} is the Higgs mass, and H is the Higgs field. When $\lambda > 0$ and $m_{\mathrm{H}}^2 < 0$, this potential

Table 1.1: Symmetries of the standard model [1].

Symmetry	Lie Group	Symmetry Type	Conservation Law
Poincaré	Translations×SO(3,1)	Global	Energy, Momentum, Angular momentum
Gauge	SU(3)×SU(2)×U(1)	Local	Color charge, Weak isospin, Electric charge, Weak hypercharge
Baryon phase	U(1)	Global (Accidental)	Baryon number
Electron phase	U(1)	Global (Accidental)	Electron number
Muon phase	U(1)	Global (Accidental)	Muon number
Tau phase	U(1)	Global (Accidental)	Tau number

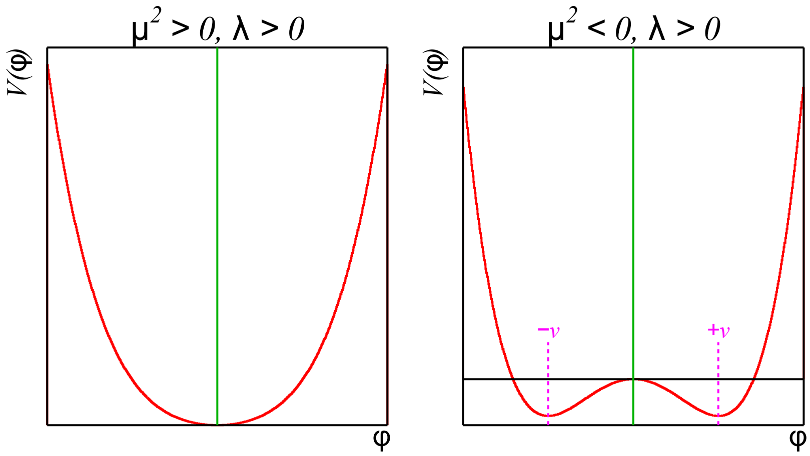

Figure 1.2: The Higgs potential $V(\phi)$ and the appearance of nonzero VEV with spontaneous symmetry breaking. [4]

has the following nonzero VEV:

$$\langle H \rangle = \sqrt{-m_{\mathrm{H}}^2/2\lambda}\,. \tag{1.3}$$

From experimental measurements on weak interactions, it is known that m_{H}^2 is raughly of the order of $-(100\,\mathrm{GeV})^2$.

The problem appears when the quantum corrections to the own mass of the Higgs particle m_{H}^2 are calculated. Consider the fermionic corrections as shown on Fig.1.3 (a). It's corresponding term in the Lagrangian is $-\lambda_f H\bar{f}f$, which eventually results in the following correction term for each fermion f [5]:

$$\delta m_{\mathrm{H}}^2 = -\frac{|\lambda_f|^2}{8\pi^2}\Lambda_{\mathrm{UV}}^2 + \ldots \tag{1.4}$$

where λ_f is the coupling of fermion f to the Higgs field. Remember that this is the parameter that determines a particle's mass, and hence the largest contribution comes from the top quark

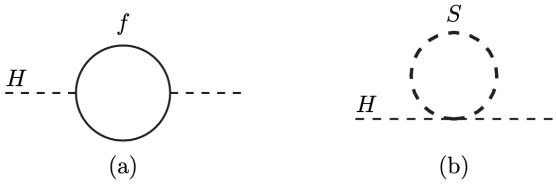

Figure 1.3: One-loop quantum corrections to the Higgs mass parameter m_H^2 for a fermion f (a), and a scalar S (b).

term as the top quark is the heaviest fermion having $\lambda_f \approx 1$. Λ_{UV} is the momentum cutoff needed to regulate the loop integral. It is taken at the value beyond which the EWK theory is no longer valid. As there is no physical theory along "the great desert" up to the Planck scale energies, it's the Planck scale that should be taken as the validity limit of the SM, which is $M_{\mathrm{Pl}} \sim 10^{16}$ TeV. Note that even Grand Unified Theory (GUT) scales are close to M_{Pl}, having values $M_X > 10^{12}$ TeV.

If Λ_{UV} is of the order of M_{Pl}, then the quantum correction to m_{H}^2 is at least 30 orders of magnitude larger than the expected value $m_{\mathrm{H}}^2 \sim -(100\,\mathrm{GeV})^2$ itself, which is considered as an unnatural situation. Notice that such a situation isn't really a problem in a renormalizable theory, because these contributions can be removed with counterterms. However removing these contributions in the present case requires an extreme fine-tuning to arrange the counterterms in the perturbation theory, which makes physicists seek if there are better explanations for this situation.

There are a number of models and scenarios trying to address the hierarchy problem: Supersymmetry (for a review see [5]) and extra dimensions scenarios like ADD [6, 7] or Randall-Sundrum [8, 9] are among the most popular ones. ADD approach to the problem is the possibility that the Planck scale being an effective scale, with the fundamental scale actually having a much lower value. SUSY on the other hand postulates new particles, whose contributions in the loop diagrams of Higgs mass correction cancel out the unnatural contribution terms. This thesis focuses on ADD type extra dimensions, however supersymmetry is also an important BSM theory and deserves a brief review before we proceed.

SUSY is the symmetry between bosonic and fermionic elementary particles. According to SUSY, each particle has a supersymmetric partner (superpartner, or spartner). Fermions have bosonic, and bosons have fermionic spartners, usually having 1/2 less spin. As there is no

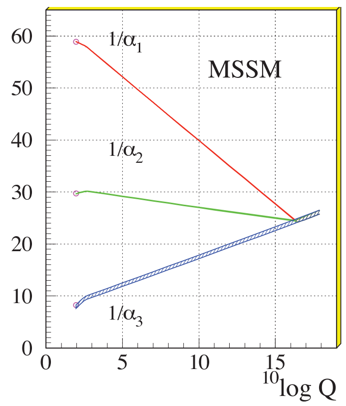

Figure 1.4: Unification of gauge couplings as foreseen by the minimal supersymmetric extension to standard model (MSSM) [10]. In the above, α_1, α_2 and α_3 are EWK, gravitational and color couplings.

record of observation of spartners, SUSY assumes that their masses must be least at the TeV scale. Contributions to the quantum corrections of Higgs mass coming from sparticles have opposite signs with their SM partners, and these can be set to exactly cancel the large contribution terms, giving nominal values for Higgs mass.

SUSY is a popular candidate for BSM physics, however the large number of free parameters in the theory renders experimental searches a challenging task. Still, it predicts unification of gauge couplings regardless of the values of these free parameters (Fig. 1.4), yet another reason for the popularity of SUSY. The lightest one in the particle spectrum of *R*-parity ("SUSYness") conserving SUSY models is considered as a candidate for dark matter by many physicists. SUSY also seems to be a critical symmetry for string theories. In conclusion, SUSY is one of the major BSM theories being searched at the LHC.

The main interest of this thesis will be the ADD type large extra dimensions. We will start our ADD discussion with reviewing the major concepts of extra dimension theories. The idea of the existence of extra dimensions is not a new one. It's a common situation to see this approach to the nature of spacetime in the same context with gravity, and the situation here is no exception.

1.2 Theories with extra dimensions

The idea of the existence of extra dimensions, and that they might be the key to unification of fundamental forces was born at the beginning of the 20^{th} century, with the Kaluza-Klein theory. It was an attempt to unify gravity with electromagnetism.

When the existence of extra dimensions is postulated, why no one has ever observed them needs to be explained. Both common sense and the experimental searches made to date show that we live in a 3 + 1 dimensional universe, therefore they must be hidden from the observations made to date.

A good place where extra dimensions could hide is very short distances. They may have eluded observation due to limitations in our experimentation; maybe we couldn't go up to energies high enough to probe their tiny distance scales. The three spatial dimensions we are familiar with are infinite, but there could exist "finite" extra dimensions, dimensions that are like closed loops, having a topology technically called "compactified".

An extra dimension theory must also succesfully relate the observed gauge and gravitational couplings to the underlying theory. Therefore finding where the extra dimensions are hiding is not enough, consistency with existing phenomena must also be shown.

We will continue with the Kaluza-Klein theory to demonstrate major features of extra dimension theories.

1.3 Kaluza-Klein Theory

Kaluza-Klein (KK) theory [11,12] was born in 1921 as an attempt to marry electromagnetism and gravity. The model introduces one extra spatial dimension, and the photon field originates from the fifth component of a five dimensional metric tensor ($g_{\mu 5}$).

Basic structure of the Kaluza-Klein spacetime has been shown on Fig. 1.5. The universe is the direct product of the Minkowski spacetime and 1-circle manifolds, $M_4 \times S_1$. All matter and gauge fields are defined on this "cylinder".

Consider a massless scalar field Φ in 5 dimensional KK space-time. If the spacetime has a

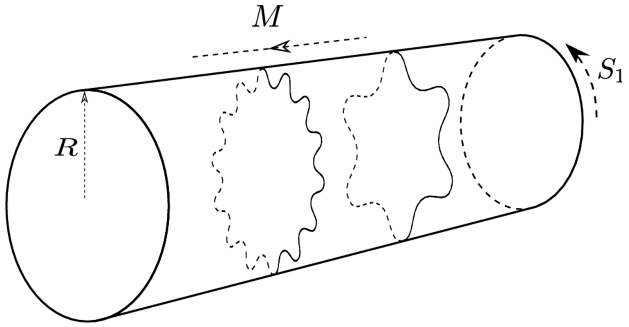

Figure 1.5: Structure of spacetime in Kaluza-Klein theory [10]. Universe is the direct product of a four dimensional manifold M, which is the familiar four dimensional Minkowski spacetime, and a 1-circle S_1. This means that one circle is assigned to every space point as the extra dimension, and the cylinder above shows the spacetime topology for a single infinite spatial dimension (a line). The extra dimension has compactification radius R. Standing waves in the middle of the "cylinder" are nonzero Kaluza-Klein modes.

compact dimension, component of the field on this dimension has to be periodic:

$$\Phi(x_\mu, x_5) = \Phi(x_\mu, x_5 + 2\pi r), \qquad \mu = 0, 1, 2, 3 \tag{1.5}$$

where x_μ are the four spacetime coordinates, x_5 is the extra dimension coordinate and r is the compactification radius of the extra dimension. Because of this periodicity, the field can be expanded in Fourier series:

$$\Phi(x_\mu, x_5) = \sum_{k=-\infty}^{k=\infty} \phi_k(x_\mu) e^{ikx_5/r}. \tag{1.6}$$

ϕ being a real function implies $\phi_{-k} = \phi_k^*$. ϕ_k also have no x_5 dependence, therefore each is a seperate 4-dimensional scalar field. They are called the Kaluza-Klein modes, or excitations. The whole spectrum of modes is called the KK tower. Two modes with $k \neq 0$ have been depicted on Fig. 1.5.

The wave equation for Φ in five dimensions is written as

$$\left(\partial_\mu^2 - \frac{\partial^2}{\partial x_5^2}\right)\Phi(x_\mu, x_5) = 0. \tag{1.7}$$

Substituting the expansion (1.6) for Φ we see that each mode satisfies the Klein-Gordon equation for a particle of mass $m_k = |k|/r$:

$$\left(\partial_\mu^2 + \frac{k^2}{r^2}\right)\phi_k(x_\mu) = 0. \tag{1.8}$$

The important result at hand here is all the excitations being massive four-dimensional fields, except for the $k = 0$ mode, which remains massless. In conclusion, a massless scalar field Φ

on KK spacetime manifests itself in 3 + 1 dimensional spacetime as an arbitrary combination of one massless particle and a tower of infinitely many massive particles.

One of the interesting features of the KK theory is that it allows the representation of particles with different spin with a single higher dimensional field, hence unifying them. For example, let's consider Einstein's gravity in 5 dimensions. the fundamental field in this theory is the five dimensional metric g_{MN}. It can be written as the sum of a small perturbation around the flat spacetime, η_{MN}:

$$g_{MN} = \eta_{MN} + \frac{h_{MN}}{(2M_5^{3/2})} \tag{1.9}$$

with h_{MN} being the 5-dimensional graviton. It's a symmetric tensor and for massless fields it has the following form [13]

$$h_{MN} = \left(\begin{array}{c|c} h_{\mu\nu} & A_\mu \\ \hline & \phi \end{array} \right) \tag{1.10}$$

in which it is decomposed into representations of the 4-dimensional Lorentz group. Here one findes three different representations:

- A symmetric spin-2 tensor field $h_{\mu\nu}$ ($0 \leq \mu, \nu \leq 3$). This field is interpreted as the 4-dimensional graviton.
- A massless spin-1 vector field: $A_\mu = g_{4\mu} = g_{\mu 4}$ ($0 \leq \mu \leq 3$). This field is naturally interpreted as the photon.
- A massless spin-zero scalar field: $\phi = g_{44}$ (named "radion")

Let's demonstrate the emergence of electromagnetism in this theory. Einstein-Hilbert action in five dimensions is written as

$$S = \int \mathrm{d}^5x \sqrt{-g}\, M_{(5)}^3 R^{(5)}, \tag{1.11}$$

where g is the determinant of the metric g_{MN}, $R^{(5)}$ is Ricci scalar and $M_{(5)}$ is the fundamental Planck scale, all in five dimensional KK spacetime. Power of $M_{(5)}$ is chosen so as to keep S dimensionless.

Using the decomposition of metric as described above together with the familiar definition $F_{\mu\nu} = \partial_\mu A_\nu - \partial_\nu A_\mu$, the action (1.11) becomes [14]

$$S = \int d^4x(M_{(5)}^3 2\pi r)\left[R^{(4)} - \frac{1}{4}F_{\mu\nu}F^{\mu\nu} + \frac{1}{2}\partial_\mu\phi\partial^\mu\phi\right] \tag{1.12}$$

where the first term in brackets is four dimensional gravity, second is a gauge field with coupling $g^2 = (M_{(5)}2\pi r)^{-1}$ (electromagnetism) and the third is a massless scalar field (radion) that couples only with gravity. The gravity term allows one to relate the effective and fundamental scales:

$$M_{(4)}^2 \equiv M_{\mathrm{Pl}}^2 = (2\pi r)M_{(5)}^3 \tag{1.13}$$

One thing to note here for future reference is the linear dependence of the effective scale $M_{(4)}$ to the radius of extra dimension r; for the same M_{Pl}, larger the extra dimension radius is, lower the fundamental scale.

As no KK modes have been observed so far, it is possible to set limits on the radius of KK type extra dimensions. If they exist, energy needed to excite these modes must be higher than currently accessible energies, rendering us and everything around us being made up of zero modes. As KK mode masses are proportional to $1/r$, a heavy excitation requires that the r is small. For the first excitations to be created at the TeV scale, an upper limit on r can be written as

$$r \lesssim (\mathrm{TeV})^{-1} \sim 10^{-17}\,\mathrm{cm} \tag{1.14}$$

Despite the exciting results it led to, Kaluza-Klein theory had it's problems too. Firstly the gravitationally interacting scalar field ϕ it predicted (radion) was unexpected. Moreover the coupling strength became unity only when $L^{-1} \sim M_{(5)}$, and the theory had the chirality problem with fermions. KK theory's importance was in it's demonstrating the possibility that a suitably compactified higher dimensional gauge theory may successfully unify gravity with other gauge interactions.

Concerning the present day theories, the idea of extra dimensions is a vital part of all string theories. String theory constitutes a basis for the ADD model with which we will continue our discussion on extra dimensions.

1.4 Large Extra Dimensions

ADD model of large extra dimensions [6] is an extra dimension model built on ideas from string theory to explain the gauge hierarchy.

String theory is a group of extra dimension theories that start with postulating that the elementary particles are extended objects called strings, instead of being pointlike objects. Excitations of these strings are observed as the particle spectrum of the physical world. Conformal anomaly dictates that string theory has 6 extra compact spatial dimensions, while the M-theory (which is a unification of string theories) is built on 7 extra dimensions. This of course is possible in a superstring theory, which is string theory incorporated with SUSY[3]. SUSY in fact is a crucial symmetry for string theory, because it allows incorporation of the fermions into the theory (which is a good thing!).

There are different string theories that are based on closed strings, or a mixture of open and closed strings. Our interest here will be Type I theories with closed strings and open strings with ends on branes.

Branes are subsurfaces of the whole space[4]. The specific type of branes, on which the open ends of strings end with Dirichlet type boundary conditions are called D-branes (Fig.1.6). Note that the extra dimensions can either be transverse, or parallel (with Neumann boundary conditions) to branes. Open string ends are free to move along the longitudinal dimensions, which give rise to KK modes, while depending on how many times they wind around transverse coordinates, they also have the winding modes.

In Type I string theories, graviton is represented by a string loop. Together with D-branes, string theory suggests a mechanism to confine all elementary particles on the brane, except for the graviton. As the gravitons are string loops they are not subject to a boundary condition and have complete freedom to propagate in all dimensions. We will end our string theory discussion with the remark that the string theory is the only consistent theory of gravity developed to date.

Where does the ADD model fit in this picture? ADD model's relation to string theory is pragmatic, it doesn't attempt to explain or support string theory and it's first principles. The model

---

[3] Nonsupersymmetric string theory is consistent in 26 dimensions.
[4] the word "brane" stems from the word "membrane"

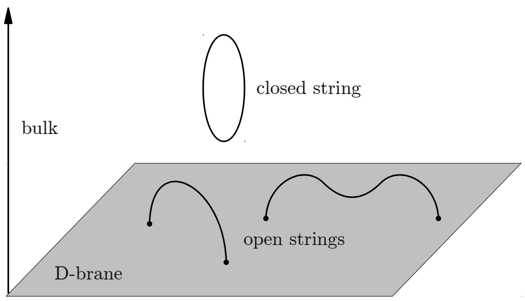

Figure 1.6: In Type I superstring theories, open strings end on D-branes, which forbids them to enter to bulk. As gravitons are closed strings, they are free to travel in the bulk.

itself relies on the strength of the gravitational interaction in the length scales of centimeter down to the Planck length 10^{-33} cm (33 order of magnitudes!) currently being assumed constant. At this point string theory is assumed to be correct, and the idea of D-branes and the confinement mechanism for all particles except gravitons on the brane are utilized. Necessity of this construct is twofold. Firstly to allow gravitons in the bulk to modify gravity in short distances. Second to confine all gauge bosons and particles carrying gauge charge on the brane to stay consistent with the SM.

Graviton being free to propagate in the bulk means the gravity is strong in short distances, but diluted and weakened in longer distances. Therefore the basic idea is defining gravity as we observe as the effective weak remnant of an interaction that is stronger at short distances. This suggests that the fundamental Planck scale should actually have a much lower value. But nature already has an energy scale, M_{EW}, so what if these two scales are close, if not equal? This summarizes the solution suggested by the ADD scenario to the hierarchy problem: Lowering M_{Pl} down to M_{EW}. Let's now continue with further model details.

ADD model assumes n transverse and compact extra dimensions of common radius R. Here large means R is large compared to the Planck length[5], because in ADD framework, the radius can be as large as a few hundred micrometers. Bulk and brane spacetimes are assumed flat with zero cosmological constant. The brane is also assumed to be "stiff", with no fluctuations into the bulk [15], [7], [16].

The model is constructed on a factorized spacetime geometry

$$M_{\mathrm{world}} = M_4 \times K_n \tag{1.15}$$

[5] which is the characteristic scale for the extra dimensions in string theory

In $4+n$-dimensional spacetime, line element has the following form

$$\mathrm{d}s^2 = g^{(4+n)}_{MN}\mathrm{d}x^M\mathrm{d}x^N, \tag{1.16}$$

where $g_{(4+n)}$ is the metric in $4+n$ dimensions, and the indices run on all dimensions $M,N = 0,\ldots,n+3$. Factorization in Eq.(1.15) means the action is written as the sum

$$S = S_{\text{brane}} + S_{\text{bulk}} \tag{1.17}$$

with the affect of extra dimensions on gravity being expressed in the S_{bulk} term.

Gravity is described in 4+n dimensions by the Einstein-Hilbert action, and for bulk it is written as [14]:

$$S_{\text{bulk}} = -\frac{1}{2}\int \mathrm{d}^{4+n}x\,\sqrt{|g^{(4+n)}|}\,M^{2+n}_{\text{Pl}(4+n)}R^{(4+n)} \tag{1.18}$$

In natural units S is dimensionless, and for a dimensionless $g^{(4+n)}$ we need to have $[R^{(4+n)}] = [\text{length}]^{-2} = [\text{mass}]^2$. Since $G^{(n+4)} = M^{-1}_{\text{Pl}(4+n)}$, this mass dimension contribution of extra dimensions are removed by $M_{\text{Pl}(4+n)}$; the power of M_{Pl} must be $n+2$. Since we assumed a flat spacetime in the beginning, the metric can be written as the sum of a flat metric plus fluctuations, as we did for the Kaluza-Klein metric. Fluctuations in 4-dimensions are represented by $h_{\mu\nu}$:

$$\mathrm{d}s^2 = (\eta_{\mu\nu} + h_{\mu\nu})\mathrm{d}x^\mu\mathrm{d}x^\nu - r^2\mathrm{d}\Omega^2_{(n)} \tag{1.19}$$

the last term being the line element in bulk, $\mathrm{d}\Omega^2_{(n)}$ being toroidal coordinates in n dimensions. Since the metric can be factorized as brane and bulk, the higher dimensional metric and Ricci scalar can safely be replaced with their $3+1$ dimensional forms.

$$\sqrt{|g^{(4+n)}|} \to \sqrt{|g^{(4)}|} \tag{1.20}$$

$$R^{(4+n)} \to R^{(4)} \tag{1.21}$$

This reduces the Planck mass to an effective parameter.

$$M^2_{\text{Pl}} \sim M^{2+n}_{\text{Pl}(4+n)}V_n \tag{1.22}$$

Where V_n is the compactification volume. Using the value $M_{\text{Pl}(4+n)} \sim M_{\text{ew}}$ and $M_{\text{Pl}} \sim 10^{18}$ GeV, we get the expression for R in hypercube topology:

$$R \sim 10^{-17+30/n}\ \text{cm} \times \left(\frac{1\ \text{TeV}}{M_{\text{ew}}}\right)^{1+2/n}. \tag{1.23}$$

See Fig. 1.7 for the R values corresponding to various n values. First case to notice could be the $n = 1$ case which has $R \sim 10^{13}$ cm. This value is about the size of the solar system and cannot be true because of common sense. On the other hand starting with $n = 2$, the predicted radii are in the sub-micrometer regime. Note that current experimental results show no deviation from Newtonian behavior at distance scales down to 5 μm [17].

On the other hand with no direct or indirect experimental data about the SM interactions down to $M_{\rm ew}^{-1}$ distances, no conclusions can be drawn on whether the extra dimensions exist or not. The way to make this situation consistent with observations is confining the SM particles to the 4-dimensional brane, and allowing only the gravitational interaction carriers (gravitons) in the $(4 + n)$ dimensional bulk.

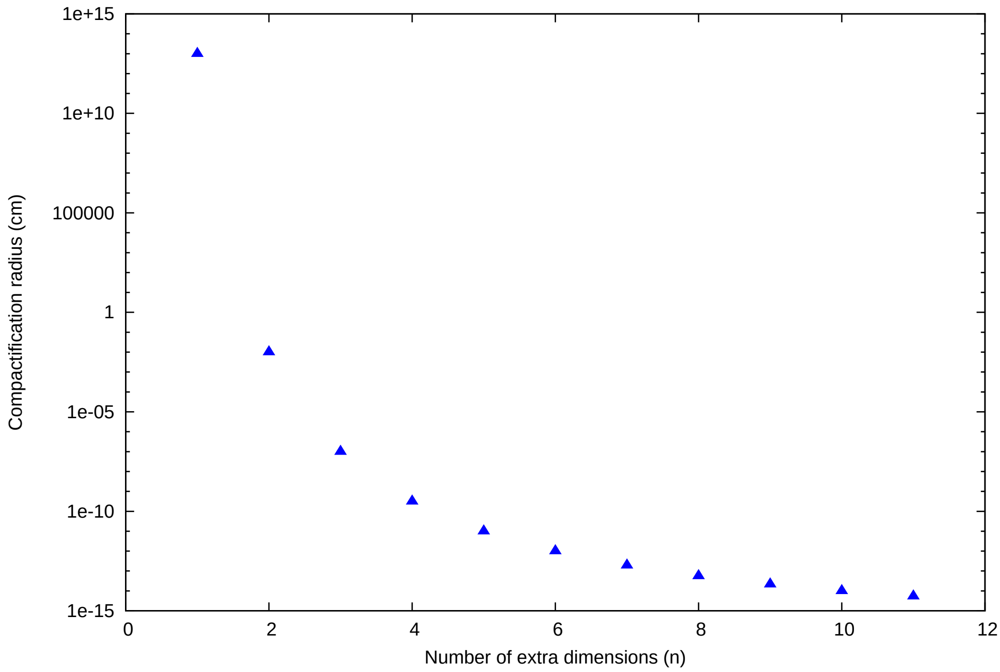

Figure 1.7: Radius R of large extra dimensions as a function of the number of extra dimensions, n, for the EW scale $m_{\rm ew} = 1$ TeV.

1.4.1 Phenomenology of Large Extra Dimensions

ADD model has a number of phenomenological implications, the most important ones are as follows:

Stronger gravity ADD model predicts a modified force law for gravity in short distances. According to the current experimental results, the $1/r$ potential is valid down to 100 μm distance.

KK excitations Mass shell condition relates the energy, momentum and invariant mass of a particle. When a particle has a momentum component in the extra dimensions, this will be observed as additional mass carried by the particle because the momentum observed on the brane is smaller than it's true value. On the other hand, compact EDs have periodic boundary conditions, which in turn means that the extra dimensional momentum components are quantized. Therefore, brane observer must observe the KK tower, infinitely many copies of the same particle, with different mass. If enough energy is provided, these excitations could be producable in collider experiments.

Graviton Production Real gravitons produced in collider experiments should leave a missing energy signature, because gravitons are invisible to the detector. Possible final states of graviton production at the LHC include a single jet, or two jets, with a significant transverse momentum imbalance.

Production of virtual gravitons should lead also to modifications of various SM process cross-sections and asymmetries, and to new processes not allowed at the tree level in the SM.

Black Hole Production Production of tiny quantum black holes at LHC energies is another prediction of the ADD model. As the gravity gets stronger in short distances in the ADD model, it becomes easier to create black holes because of larger Schwarzschild radius compared to the value calculated in 3 + 1 dimensions.

We will briefly review the questions and issues puzzling the theoreticians about the ADD model before we move on to our black hole physics discussion.

1.4.2 Downsides, problems and open questions

Not everybody is unhappy about the great desert between M_{EW} and M_{Pl}. SM predicts that the gauge couplings intersect at M_{Pl}. As we've seen before in our SUSY discussion, in the MSSM theory gauge couplings seem to intersect at $M_{\text{GUT}} \sim 10^{16}$ GeV (Fig. 1.4), which seems to be rather close to M_{Pl}. These are encouraging hints for BSM theories –especially for SUSY– and ADD model takes it away by lowering M_{Pl} down to M_{EW}.

Concerning the hierarchy problem, does the ADD model really solve it? In fact what ADD model does is not to provide an explanation to the huge gauge hierarchy but to translate it into a geometric hierarchy. The question of why the extra dimensions are unusually large compared to the distance scales of fundamental interactions remains. However it's important to note that the ADD model still brings a new perspective to understand the gauge hierarchy, a new area of possibilities from the domain of spacetime geometry for an actual solution.

An important issue of the ADD model is the proton stability. Proton is known to have a very long lifetime, $\tau > 10^{33}$ years. This is a common concern of BSM theories, because usually introduced new baryon number non-conserving interactions lead to proton decay to leptons. However in a traditional GUT, such diagrams are suppressed because of the high value of $M_{\text{GUT}} \sim 10^{-16}$ GeV. This scale is associated with the mass of GUT particles which also appear in intermediate propagators. This means that the proton decay amplitude diagrams are heavily suppressed. If the M_{GUT} is as low as M_{EW}, this suppression is essentially removed.

A number of ad hoc mechanisms have been suggested for the proton decay suppression, one being the "split fermions" scenario. According to this scenario, the brane has a large thickness in longitudinal dimensions, and quarks and leptons are localized at different locations along them. Therefore the coupling of electrons to quarks with GUT particles via three-point vertices is heavily suppressed because the overlap of quark and fermion wavefunctions in the brane are so small. The space needed to split the fermions could as well be provided by the thickness of the brane itself, which is usually called the "fat brane" scenario.

An example to open questions regarding the ADD model could be the following. The model assumes string theory, and the string theory strongly suggests SUSY. So if realized by nature, where will SUSY fit in this extra dimension picture?

1.4.3 Current Limits on ADD Model Parameters

With the startup of the collisions at the LHC with 7 TeV COM energy, new bounds on the model parameters started to be available. Here we present the 95% confidence level limits from both the CMS [18], and the ATLAS [19] experiments, set from the monojet channel. In this channel two colliding partons have one graviton and a single energetic jet in the final state.

Bounds for M_{Pl} set by the ATLAS experiment are for 2-4 extra dimensions and range from 2.3 TeV down to 1.8 TeV (Table 1.2). CMS limits are consistent with this picture but also cover the 5 and 6 extra dimension cases (Table 1.3).

Table 1.2: Lower limits on ADD model parameter M_{Pl} from the ATLAS experiment for 36 pb^{-1} integrated luminosity, with the corresponding extra dimension radii. δ is the number of extra dimensions.

δ	M_{Pl} (TeV)	R (pm)
2	2.3	9.2×10^{7}
3	2.0	1.1×10^{3}
4	1.8	4.1

Table 1.3: Expected and observed lower limits on M_{Pl} from CMS for 36 pb^{-1} integrated luminosity, with NLO k factors applied.

δ	M_{Pl} Exp. (TeV)	M_{Pl} Obs. (TeV)
2	2.41	2.56
3	1.99	2.07
4	1.78	1.86
5	1.68	1.74
6	1.62	1.68

CHAPTER 2

BLACK HOLES

Gravitational interaction is different. It is a unipolar attractive-only interaction with infinite range. All particles carrying energy-momentum gravitate, and local regions of energy concentration can only grow. As the concentration grows, the attractive force increases, so it grow faster and stronger. At some point the gravitational pull of such an object becomes so strong that even light cannot escape from it. This type of physical objects are generally called black holes.

Black holes absorb all the incoming light, but reflect or radiate (almost) nothing. Since we receive no light from them, they are called 'black'. Therefore it is impossible to observe a black hole directly. They can only be observed through their indirect effects on other objects; a visible astronomical object orbiting a massive and invisible compact object is a typical signature of black hole existence.

There is a large amount of observational evidence throughout the universe supporting the black hole thesis. All known black holes are astronomical objects as black holes are usually formed from the collapse of massive stars. Many galaxies are thought to host a supermassive black hole at their centers[1]. Masses of known black holes range from a few solar masses to $O(10^{10})$ solar mass. The closest known black hole is the Cygnus X-1, which is at a distance of 8000 light years; a fairly safe distance to the solar system.

Schwarzschild radius is one of the most important parameters of a black hole. Every massive body has an associated spherical surface whose radius is the Schwarzschild radius (R_S). In classical mechanics, it's calculated as the radius of a hyphothetical sphere around a mass

[1] Our galaxy is not an exception to this observation. The black hole at the center of our galaxy is named Sagittarius A*

where the escape velocity equals the speed of light. It's value is $R_S = 2GM/c^2$, or in natural units simply $R_S = 2GM$. Notice that R_S increases with mass. For example, Schwarzschild radius of the Earth is less than one centimeter while that of Sun is about 3 km. If the entire mass of an object is inside this surface, it's a black hole.

2.1 Types of Black Holes

Black holes can be classified according to their masses, or equivalently the size of their Schwarzschild radii:

Supermassive black holes They are usually found at the center of galaxies and may have masses of the order of billions of solar masses. For example, Schwarzschild radius of the black hole at the center of our galaxy is about 7.8 million kilometers (less than 10 suns in diameter) These black holes have density (mass divided by total volume that is in the Schwarzschild radius surface) much less than that of water. Also tidal forces around these black holes should be much less compared to smaller black holes because of the large Schwarzschild radius.

Stellar black holes These are black holes with mass of the order of a few solar masses. They are formed by the gravitational collapse of massive stars. All the possible final states of a star that burned out it's fuel can evolve have a maximum mass limit, and if the mass of the star is more than this, no known outward force is left to support it. Catastrophic gravitational collapse leads to the formation of an event horizon and the star becomes a black hole.

Primordial Normally there are no known mechanisms to form a black hole with size smaller than a stellar black hole. However, the extremely high energy densities that existed immediately after the big bang could allow formation of such objects. Note that these are hypothetical objects and their existence hasn't been observed yet, however their calculated lifetimes show that they might be decaying in present time and the signatures of their decays are being sought.

Quantum (higher dimensional) black holes If ADD type extra dimensions are realized by nature, tiny (sub-millimeter size) quantum black holes may exist too. It's been shown

Table 2.1: Different types of black holes according to their physical attributes.

	Static ($J = 0$)	Rotating ($J > 0$)
Uncharged ($Q = 0$)	Schwarzschild	Kerr
Charged ($Q \neq 0$)	Reissner-Nordström	Kerr-Newman

that [20] these objects might be produced at LHC energies. This type of black holes are the main interest of this thesis study.

Besides the physical size, black holes have a number of physical characteristics that affect their nature dramatically. According to the the no-hair theorem [21], black hole solutions in general relativity can be completely expressed in terms of three observable parameters: mass M, angular momentum J and electric charge Q. All remaining information gets effectively lost during formation as they are now beyond the event horizon.

In general, there are a total of four black hole solutions, and corresponding black holes are named after the names of their metrics (see Table 2.1). We will now discuss the features all these different types of objects with some detail, and the first one will be the most fundamental type of them all: The Schwarzschild black hole.

2.2 The Schwarzschild Black Hole

A Schwarzschild black hole is a static (non-rotating) black hole that is electrically neutral. For this reason it's the most fundamental black hole type. It's features are being expressed by the Schwarzschild solution. This metric will also be the limiting case for the charged and rotating black hole cases so we will review it's derivation with some detail.

2.2.1 Derivation of the Schwarzschild metric

Schwarzschild metric is a solution of Einstein's field equation for the region outside of a static, non-charged, massive body. Here we will be reviewing the major steps of the derivation, more detailed derivations can be found elsewhere, e.g. [22].

There are two assumptions used for the solution:

- Static: Metric must be both time-independent and symmetric under time reversal.
- Isotropic: Metric must be invariant under spatial rotations, i.e. there must not be a preferred direction in space.

In addition to these assumptions, we will require the boundary condition that the metric becomes flat at large distances from the gravitating body.

We start with a general metric form, i.e. a metric with 10 components. As we're seeking a solution in 3 + 1 dimensional spacetime, each component is a function of three spherical coordinates and one time parameter, r, θ, ϕ and t.

The time reversal invariance requirement $(r, \theta, \phi, t) \rightarrow (r, \theta, \phi, -t)$ implies

$$g'_{\mu 3} = \frac{\partial x_\alpha}{\partial x'_\mu} \frac{\partial x_\beta}{\partial x'_3} g_{\alpha\beta} = -g_{\mu 3} \quad (\mu \neq 3) \tag{2.1}$$

which holds if and only if

$$g_{\mu 3} = 0 \quad (\mu \neq 3) \tag{2.2}$$

In a similar way, the coordinate transformation assumptions on the angular variables require

$$g_{\mu 1} = 0 \quad (\mu \neq 1) \tag{2.3}$$

$$g_{\mu 2} = 0 \quad (\mu \neq 2) \tag{2.4}$$

Therefore the solution must be diagonal

$$g_{\mu\nu} = 0 \quad (\mu \neq \nu), \tag{2.5}$$

having the following form:

$$\mathrm{d}s^2 = g_{00}\mathrm{d}r^2 + g_{11}\mathrm{d}\theta^2 + g_{22}\mathrm{d}\phi^2 + g_{33}\mathrm{d}t^2. \tag{2.6}$$

The static assumption requires that $g_{\mu\mu}$ can't have t dependence. This, and the spherical symmetry requirement dictates that g_{00} and g_{33} must be functions of the radial variable r only:

$$g_{00} = A(r), \quad g_{33} = B(r) \tag{2.7}$$

For the solution to be isotropic, an arbitrary constant r-t hypersurface must reduce to a 2-sphere of radius r_0 as given below

$$\mathrm{d}l^2 = r_0^2(\mathrm{d}\theta^2 + \sin^2\theta \mathrm{d}\phi^2) \tag{2.8}$$

Let $\tilde{g}_{22}$ and $\tilde{g}_{33}$ be components of the metric solution we're seeking, on this hypersurface. If it is to be identical to a 2-sphere, it should satisfy

$$\tilde{g}_{22}\left(\mathrm{d}\theta^2 + \frac{\tilde{g}_{33}}{\tilde{g}_{22}}\mathrm{d}\phi^2\right) = r_0^2(\mathrm{d}\theta^2 + \sin^2\theta \mathrm{d}\phi^2) \tag{2.9}$$

so,

$$\tilde{g}_{22} = r_0^2, \qquad \tilde{g}_{33} = r_0^2 \sin^2\theta \tag{2.10}$$

These results must hold on all hypersurfaces of arbitrary r values:

$$g_{22} = r^2, \qquad g_{33} = r^2 \sin^2\theta \tag{2.11}$$

and hence the metric takes the following form:

$$\mathrm{d}s^2 = A(r)\mathrm{d}r^2 + r^2\mathrm{d}\theta^2 + r^2 \sin^2\theta \mathrm{d}\phi^2 + B(r)\mathrm{d}t^2 \tag{2.12}$$

Having used up all the available symmetries we now will employ the Einstein's equation to further proceed with the solution. As we're seeking a solution in the vacuum outside of the massive body, we have $T_{\mu\nu} = 0$, where $T_{\mu\nu}$ is the energy-stress tensor. We also take $\Lambda = 0$ for the cosmological constant. Under these assumptions, what one gets is the vacuum field equations:

$$R_{\mu\nu} = 0 \tag{2.13}$$

where $R_{\mu\nu}$ is the Ricci curvature tensor.

Let's assume that the radial functions have an exponential form:

$$A(r) = e^{\alpha(r)}, \qquad B(r) = -e^{\beta(r)} \tag{2.14}$$

Evaluation of Cristoffel symbols yield the following nonzero terms (note that $\Gamma^{\alpha}_{\beta\gamma} = \Gamma^{\alpha}_{\gamma\beta}$):

$$\Gamma^3_{30} = \frac{1}{2}\partial_0\beta, \qquad \Gamma^0_{33} = \frac{1}{2}e^{\beta-\alpha}\partial_0\beta, \qquad \Gamma^0_{00} = \frac{1}{2}\partial_0\alpha \tag{2.15}$$

$$\Gamma^1_{01} = \frac{1}{r}, \qquad \Gamma^0_{11} = -re^{-\alpha}, \qquad \Gamma^2_{02} = \frac{1}{r} \tag{2.16}$$

$$\Gamma^0_{22} = -re^{-\alpha}\sin^2\theta, \qquad \Gamma^1_{22} = -\sin\theta\cos\theta, \qquad \Gamma^2_{12} = \cot\theta \tag{2.17}$$

These terms are used to write the Riemann tensor $R^{\rho}_{\sigma\mu\nu}$, and eventually the Ricci tensor $R_{\mu\nu}$. Inserting $R_{\mu\nu}$ into (2.13), yields the following three equations

$$\frac{e^{\beta-\alpha}}{r}\left(\partial_0\alpha - \frac{1}{r}\right) - \frac{e^{\beta}}{r^2} = 0, \tag{2.18}$$

$$\frac{\partial_0\beta}{r} + \frac{1}{r^2}(1 - e^{\alpha}) = 0, \tag{2.19}$$

$$\frac{1}{2}r^2 e^{-\alpha}\left[\partial_0^2\beta - \frac{1}{2}\partial_0\alpha\partial_0\beta + \frac{1}{2}(\partial_0\beta)^2 + \frac{\partial_0\beta - \partial_0\alpha}{r}\right] = 0. \tag{2.20}$$

Combining these equations we find

$$\partial_0\alpha = -\partial_0\beta, \tag{2.21}$$

$$\partial_0\alpha = \frac{1}{2}(1 - e^{\alpha}). \tag{2.22}$$

Eq. (2.21) immediately gives

$$\alpha = -\beta + c, \tag{2.23}$$

where c is the integration constant. This constant can be absorbed into time coordinate with the rescaling $t \rightarrow t' = e^{-c}t$ so,

$$\alpha = -\beta \tag{2.24}$$

Solving (2.22) for α, and using the above relation gives $A(r)$ and $B(r)$

$$e^{\alpha} = \left(1 - \frac{C}{r}\right)^{-1} = g_{00} = -\frac{1}{g_{33}} \tag{2.25}$$

where C is a constant to be determined.

In the weak field limit, the time component of metric around a body of mass M is given by

$$g_{33} = -\left(1 - \frac{2GM}{r}\right) \tag{2.26}$$

Note that we're using natural units. This should match g_{33}, hence a comparison with (2.25) shows that $C = 2GM$. We identify this parameter as the Schwarzschild radius R_S.

The Schwarzschild metric takes the following final form:

$$\mathrm{d}s^2 = \left(1 - \frac{R_S}{r}\right)^{-1}\mathrm{d}r^2 + r^2\mathrm{d}\Omega^2 - \left(1 - \frac{R_S}{r}\right)\mathrm{d}t^2 \tag{2.27}$$

where $\mathrm{d}\Omega^2 = \mathrm{d}\theta^2 + \sin^2\theta\mathrm{d}\phi^2$ is the line element on the surface of the 2-sphere S^2.

When we measure the radial increment of proper distance using the Schwarzschild metric by setting $\mathrm{d}\theta = \mathrm{d}\phi = \mathrm{d}t = 0$, what we find is not $\mathrm{d}r$, but $\mathrm{d}r/(1 - R_\mathrm{S}/r)^{1/2}$ instead. Therefore the r coordinate is not exactly a measure of proper distance. Actually, the sphere we obtain for constant r and t values:

$$\mathrm{d}l^2 = r^2 \mathrm{d}\Omega^2 \tag{2.28}$$

has the surface area $4\pi r^2$, therefore the coordinate r is actually related to proper area.

Concerning the time coordinate t, (2.27) shows that it's not exactly the time kept by a standard clock in the field of the gravitating body. We find that the proper time interval kept by a stationary clock ($\mathrm{d}r = \mathrm{d}\theta = \mathrm{d}\phi = 0$) is related to coordinate time as follows

$$\mathrm{d}\tau = \left(1 - \frac{R_\mathrm{S}}{r}\right)^{1/2} \mathrm{d}t \tag{2.29}$$

The two intervals agree as $r \to \infty$. Therefore the Schwarzschild time t measures the time recorded by a clock located at spatial infinity.

The angular parameters θ and ϕ are the usual zenith and azimuth angles. The parameters r, θ, ϕ and t are collectively called Schwarzschild coordinates.

According to the Birkhoff's theorem, Schwarzschild metric solution is the unique spherically symmetric solution in the vacuum. Theorem states that a spherically symmetric metric is necessarily static, therefore it must be the Schwarzschild solution. Hence, a star experiencing purely radial motion (i.e. collapsing, expanding or pulsating) cannot emit gravitational waves.

The Schwarzschild metric (2.27) has two singularities, first is at $r = 0$, where g_{33} vanishes, and the second at $r = R_\mathrm{S}$, where g_{00} goes to infinity. The latter one turns out to be a singularity due to the particular choice of coordinates. We will demonstrate this by studying the surface $r = R_\mathrm{S}$ in other coordinate systems, which is the next topic in this chapter. On the other hand, unlike the former one, the singularity at $r = 0$ is a physical singularity, because at this location the curvature of spacetime diverges.

2.2.2 Alternative coordinate systems

To study the singularity at $r = R_\mathrm{S}$, consider purely radial null curves in Schwarzschild spacetime, i.e. trajectories whose angular coordinates are constant and $\mathrm{d}s^2 = 0$:

$$\mathrm{d}s^2 = 0 = \left(1 - \frac{R_\mathrm{S}}{r}\right)^{-1} \mathrm{d}r^2 - \left(1 - \frac{R_\mathrm{S}}{r}\right) \mathrm{d}t^2 \tag{2.30}$$

therefore

$$\frac{\mathrm{d}t}{\mathrm{d}r} = \pm\left(1 - \frac{R_\mathrm{S}}{r}\right)^{-1} \tag{2.31}$$

This expression measures the slope of light cones on a spacetime diagram of the t-r plane. For large r values, we get ± 1, which is what we expect in flat spacetime. However as $r \to R_\mathrm{S}$, the slope becomes infinite, which means that an infinitesimal radial translation requires an infinite amount of time. This means that the light cones close up as R_S is approached. An observer located at spatial infinity sees a photon approaching the Schwarzschild radius, but never crossing it. It merely asymptotes to this radial distance. We will now study descent to a BH through other coordinates to see what actually is going on at $r = R_\mathrm{S}$.

Let's make the following change to the radial coordinate map:

$$\frac{1}{1 - \frac{R_\mathrm{S}}{r}}\mathrm{d}r^2 = \left(1 - \frac{R_\mathrm{S}}{r}\right)(\mathrm{d}r^*)^2 \tag{2.32}$$

The resultant coordinate system only covers the radial region $r > R_\mathrm{S}$ and $r = R_\mathrm{S}$ is now mapped to minus infinity. r^* is called the tortoise coordinate and is explicitly written as

$$r^* = r + 2MG \log\left(\frac{r - r_s}{r_s}\right) \tag{2.33}$$

The tortoise coordinate satisfies

$$\frac{\mathrm{d}r^*}{\mathrm{d}r} = \left(1 - \frac{R_\mathrm{S}}{r}\right)^{-1} \tag{2.34}$$

Let's define the ingoing and outgoing null coordinates u and v:

$$u = t - r^* \tag{2.35}$$

$$v = t + r^* \tag{2.36}$$

The inward going radial null geodesics are characterized by v = constant, and the outgoing ones satisfy u = constant (Fig. 2.1). By replacing t with v and u, we obtain the ingoing and outgoing Eddington-Finkelstein coordinates. The corresponding metrics are written as

$$\mathrm{d}s^2 = -\left(1 - \frac{R_\mathrm{S}}{r}\right)\mathrm{d}v^2 + 2\mathrm{d}v\mathrm{d}r + r^2\mathrm{d}\Omega^2 \quad \text{(ingoing)} \tag{2.37}$$

$$\mathrm{d}s^2 = -\left(1 - \frac{R_\mathrm{S}}{r}\right)\mathrm{d}u^2 - 2\mathrm{d}u\mathrm{d}r + r^2\mathrm{d}\Omega^2 \quad \text{(outgoing)} \tag{2.38}$$

It can be shown that the determinant of these metrics are finite and perfectly regular at $r = R_\mathrm{S}$. As this implies that the metric is invertable[2], we're led to the conclusion that the singularity at $r = R_\mathrm{S}$ in Schwarzschild coordinates is simply a coordinate singularity.

[2] Note that an arbitrary $N \times N$ matrix A satisfies $AA^{-1} = I$ only if it's an invertable matrix (I is the $N \times N$ unit matrix).

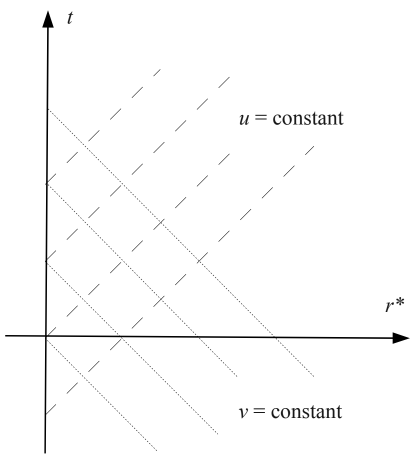

Figure 2.1: Null coordinates u and v.

Remember that the Schwarzschild solution was valid only for the exterior region $r > R_S$. We couldn't infer from Schwarzschild metric about $r < R_S$ because of the singularity at R_S, but since the EF coordinates have no such singuarity, we can infer in this region also. As this surface is not physically singular, a falling observer sees nothing special while passing thru the event horizon. The new line elements we wrote do not represent a new geometry, they represent the same geometry with the metric written in Schwarzschild coordinates, only the spacetime points are labeled with a different set of coordinates.

2.2.3 Kruskal-Szekeres Coordinates and the Maximally Extended Schwarzschild Solution

This coordinate system covers the entire spacetime of the maximally extended Schwarzschild metric and is well-behaved except at the physical singularity at the origin. Kruskal coordinates replace the Schwarzschild coordinates t and r with V and U defined below for the interval $r > R_S$:

$$V = \left(\frac{r}{R_S} - 1\right)^{1/2} e^{r/2R_S} \sinh\left(\frac{t}{2R_S}\right), \tag{2.39}$$

$$U = \left(\frac{r}{R_S} - 1\right)^{1/2} e^{r/2R_S} \cosh\left(\frac{t}{2R_S}\right), \tag{2.40}$$

while at the interior region $0 < r < R_{\rm S}$:

$$V = \left(1 - \frac{r}{R_{\rm S}}\right)^{1/2} e^{r/2R_{\rm S}} \cosh\left(\frac{t}{2R_{\rm S}}\right), \tag{2.41}$$

$$U = \left(1 - \frac{r}{R_{\rm S}}\right)^{1/2} e^{r/2R_{\rm S}} \sinh\left(\frac{t}{2R_{\rm S}}\right), \tag{2.42}$$

where r and t are Schwarzschild coordinates. In terms of the U and V coordinates, Schwarzschild metric is written as

$$\mathrm{d}s^2 = \frac{4R_{\rm S}}{r} e^{-r/R_{\rm S}}(-\mathrm{d}V^2 + \mathrm{d}U^2) + r^2\mathrm{d}\Omega^2 \tag{2.43}$$

Where r is a function of U and V, defined implicitly as follows

$$V^2 - U^2 = \left(1 - \frac{r}{R_{\rm S}}\right) e^{r/R_{\rm S}} \tag{2.44}$$

With this metric we now see that spacetime is nonsingular at $r = 2M$, actually there is nothing special with this surface at all.

To see how radial light rays behave in these coordinates let's set $\mathrm{d}s^2 = 0$ in (2.43). This gives $\mathrm{d}U = \pm\mathrm{d}V$, therefore

$$V = \pm U + \text{const.} \tag{2.45}$$

which reveals one of the most interesting features of the Kruskal map: Light cones are always at 45° in the $V - U$ space. Light rays travel at V = constant (ingoing) or U = constant (outgoing). A timelike trajectory always lies inside the (two dimensional) light cone. In this coordinate system, Schwarzschild radius $r = 2M$ is located at

$$V = \pm U. \tag{2.46}$$

Kruskal coordinates (V, U, θ, ϕ) cover the entire spacetime, see Fig. 2.2. The figure has been split to four regions by event horizons. Bottom of the diagram represents the past, while the top part is the future. There are two physical singularities at $r = 0$, the past and future singularities.

Region I is the $r > R_{\rm S}$ region, i.e. where the Schwarzschild coordinates are well defined. It is asymptotically flat and represents our universe. Region II is beyond the event horizon and therefore it is the interior of the black hole. As the light cones are at 45°, all timelike paths end up in the physical singularity. No timelike paths can go back to region I once they enter region II. An observer in region I can send messages to both regions.

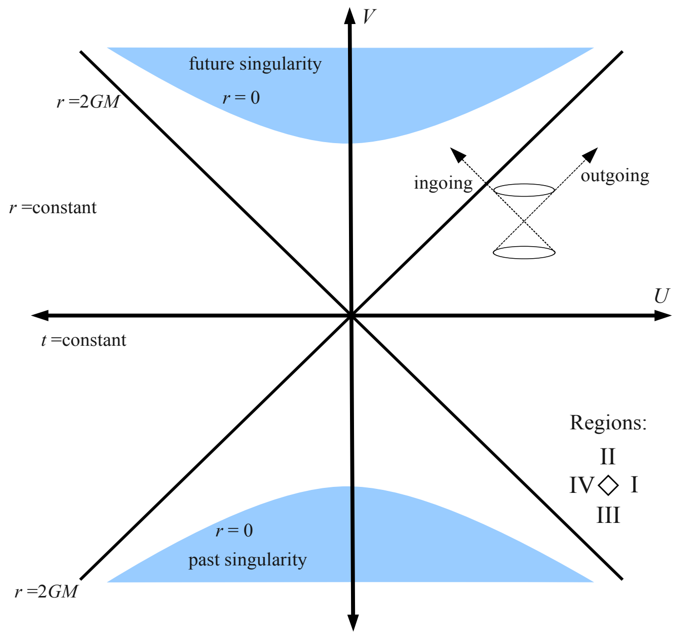

Figure 2.2: Schwarzschild spacetime in Kruskal-Szekeres coordinates. Note that each point is a two sphere.

Region III contains the past physical singularity and has an event horizon. All timelike paths are outwards from this region, and nothing can come back either. This curious region therefore represents a so-called “white hole”; the exact opposite of a black hole (it’s the time reverse of a black hole since V is a time coordinate). Note that it cannot exist because the initial conditions needed for it’s formation are unphysical.

Region IV is another asymptotically flat universe with $r > R_S$, possibly a mirror image of ours, but not necessarily. But if this is another universe, is it possible to travel there and back? Unfortunately (or maybe fortunately) this doesn’t seem to be possible. Note that only space-like paths lead to this region, all timelike paths point to the physical singularity. Therefore it is not possible to pass from one universe to another without hitting the singularity.

2.3 Conformal Diagrams

Cleverly made conformal transformations are a great help in understanding the causal structure of metrics, especially when there is spherical symmetry like in the Schwarzschild metric case. Causal structure of a spacetime is knowing which event can influence another, hence knowing the light cones. One can also bring the infinity of a coordinate to a finite value with a conformal transformation, which is quite useful because it allows one to represent a whole spacetime with a diagram that fits on a single piece of paper.

Conformal transformations preserve angles between four vectors. Therefore they essentially are a local change of scale and rotation.

The transformed metric can be depicted on a spacetime diagram, which is called a conformal diagram (or Carter-Penrose diagram). Such a diagram represents a two dimensional surface of radial and time coordinates with the angular coordinates fixed. While all light cones are at 45° as in Kruskal diagram, the main difference in conformal diagram is the infinities being located at finite values.

Conformal (Penrose) diagram for Schwarzschild metric has been shown on Fig. 2.3.

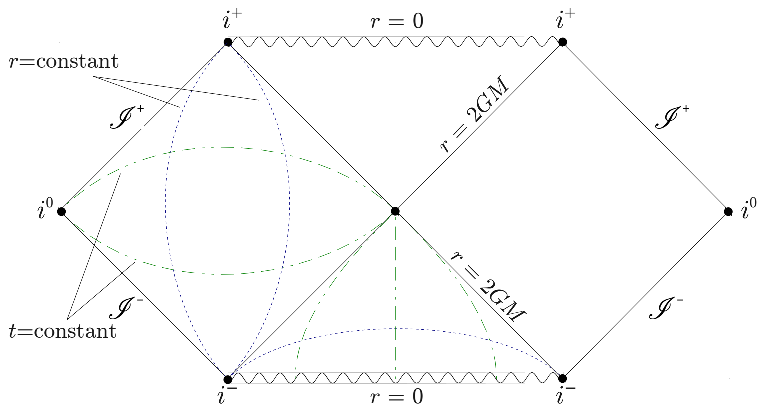

Figure 2.3: Conformal diagram of Schwarzschild black hole. As in all space-time diagrams, horizontal and vertical are radial and time axes. Each point on the diagram is a two-sphere.

Since the conformal transformation shrinks infinities to finite values, constant time and space coordinate curves become hyperbolas. At the corners of the diagram there are the points where these curves converge; these are the "conformal infinity" points i^+ and i^- (future and past infinity). We should emphasize that the i^+ and i^- points are distinct from the $r = 0$ line.

The line labeled $\mathscr{I}^-$ represent the origin of incoming light rays, while $\mathscr{I}^+$ is where outgoing light rays end.

The diagram clearly shows that $r = 0$ line is the end of time for any object that crossed the event horizon.

2.4 Charged Black Holes

A static black hole with nonzero electric charge ($Q \neq 0$) is described by the Reissner-Nordström (RN) metric:

$$\mathrm{d}s^2 = \left(1 - \frac{r_s}{r} + \frac{r_Q^2}{r^2}\right)^{-1} \mathrm{d}r^2 + r^2 d\Omega^2 - \left(1 - \frac{r_s}{r} + \frac{r_Q^2}{r^2}\right)\mathrm{d}t^2, \tag{2.47}$$

where

$$r_Q^2 = GQ^2 \tag{2.48}$$

and Q is the electric charge of the black hole. Note that as $Q \to 0$, the Schwarzschild metric is retained.

We define

$$\Delta = 1 - \frac{r_s}{r} + \frac{r_Q^2}{r^2} \tag{2.49}$$

and rewrite the RN metric in terms of Δ

$$\mathrm{d}s^2 = -\Delta \mathrm{d}t^2 + \Delta^{-1}\mathrm{d}r^2 + r^2\mathrm{d}\Omega^2 \tag{2.50}$$

Let's find the location of the event horizon using the $g^{rr} = 0$ condition. As $g^{rr} = \Delta(r)$, we find an unusual result:

$$r_{\pm} = \frac{1}{2}\left(R_\mathrm{S} \pm \sqrt{R_\mathrm{S}^2 - 4R_Q^2}\right) \tag{2.51}$$

Depending on the values of R_S and R_Q, the metric may have two event horizons.

There are three distinct physical cases depending on the values of these variables, which corresponds to the conflicting effects between gravitational and electric forces:

Case 1: $R_\mathrm{S} > 2R_Q$ Δ has two zeroes at r^- and r^+, at which the metric is singular. The surfaces $r = r^{\pm}$ are both null surfaces, and there are two nested event horizons. Similar to the Schwarzschild case, these surfaces are coordinate singularities. A difference from the Schwarzschild black hole is, the physical singularity here is a timelike line, not a spacelike line.

Conformal diagram for a charged black hole has been depicted on Fig. 2.4. The outer horizon at r_+ behaves exactly like the Schwarzschild case. Once an observer crosses it, r becomes a timelike coordinate and only possible motion is towards decreasing r. Once the observer crosses the inner horizon at r_-, r becomes spacelike again and one has the freedom to move radially away from the singularity. It's possible to fall into the singularity (Path B), but more importantly, it's possible to move radially away and outside of the inner horizon. This second choice reveals another interesting behavior (Path A), once the observer chooses to leave, now r becomes timelike again and the observer must move in the increasing r direction, towards the outer horizon, and eventually leave the black hole, as if being ejected from a white hole. As a summary, once you enter a charged black hole, you either fall into the singularity, or the black hole will kick you out.

Case 2: $R_S = 2R_Q$ This is the case when the two horizons merge at $r = R_S/2$, and it is called an "extremal black hole". This case is inherently unstable and addition of even a small amount of charged matter will spoil it. It represents the balance between gravitational and electric forces. The name extremal means this is a black hole with minimum possible mass allowed concerning it's charge (and angular momentum).

Case 3: $R_S < 2R_Q$ The metric coefficient $\Delta(r)$ is never zero, which means that this configuration has no event horizon. However the physical singularity at $r = 0$ still exists, but since there is no event horizon to obscure it from the rest of the universe, this is a naked singularity. According to Roger Penrose's cosmic censorship conjecture, nature cannot realize this case during gravitational collapse. Also it can be shown that a high amount of charge prevents the gravitational collapse [23]. The EM energy in this case exceeds the total energy of the BH, which requires that the mass is negative. Hence this physical case is generally considered unphysical. Conformal diagram of this case is shown in Fig. 2.5. It's almost the same as the Minkowski spacetime, except the singularity at $r = 0$.

2.5 Rotating Black Holes

Mathematical analysis of these type of black holes has an inherent technical difficulty: One has to give up the spherical symmetry. As the black hole to be analyzed is rotating, it's as-

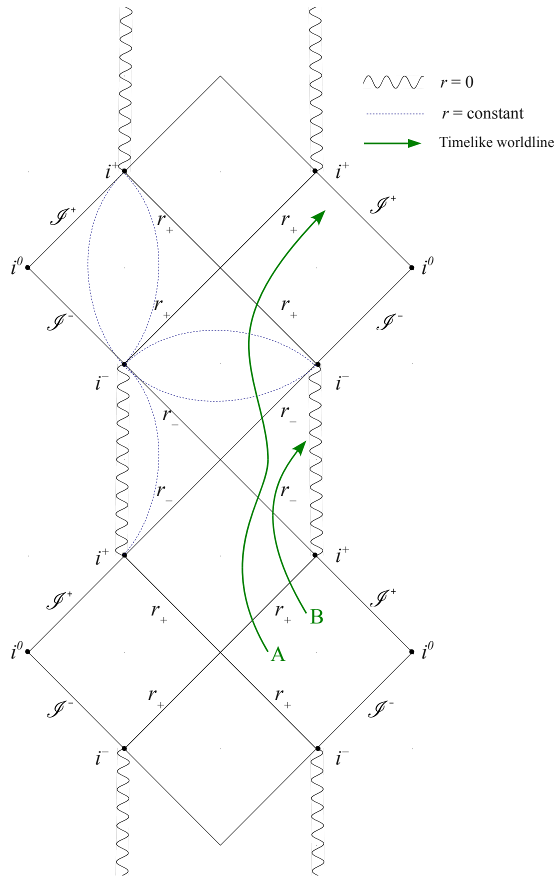

Figure 2.4: Penrose diagram of RN metric featuring a double horizon [22].

sumed to be symmetric around a static rotation axis, therefore the relevant coordinate system here is the cylindrical coordinates.

The metric describing the geometry of the spacetime around a massive rotating black hole is the Kerr metric:

$$\begin{aligned} \mathrm{d}s^2 = &-\left(1-\frac{R_\mathrm{S} r}{\rho^2}\right)\mathrm{d}t^2 - \frac{R_\mathrm{S} a r \sin^2\theta}{\rho^2}(\mathrm{d}t\mathrm{d}\phi + \mathrm{d}\phi\mathrm{d}t) \\ &+\frac{\rho^2}{\Delta}\mathrm{d}r^2 + \rho^2\mathrm{d}\theta^2 + \frac{\sin^2\theta}{\rho^2}\left[(r^2+a^2)^2 - a^2\Delta\sin^2\theta\right]\mathrm{d}\phi^2 \end{aligned} \tag{2.52}$$

where $R_\mathrm{S} = 2GM$ as before. We also define the following length scales:

$$\Delta(r) = r^2 - R_\mathrm{S} r + a^2, \tag{2.53}$$

$$\rho^2(r,\theta) = r^2 + a^2\cos^2\theta, \tag{2.54}$$

$$a = J/M. \tag{2.55}$$

Obviously the constant a represents the angular momentum per unit mass.

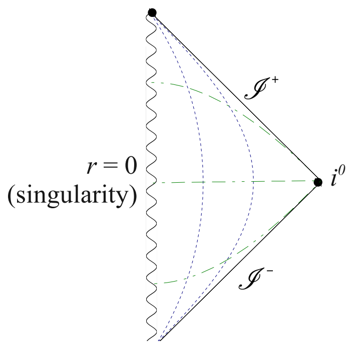

Figure 2.5: Conformal diagram of the $R_S < 2R_Q$ case for the RN metric featuring a naked singularity.

Including the electric charge in the solution is also easy, simply replace R_S with $2(R_S - R_Q)$, (remember $R_Q = GQ^2$) and the resultant metric is the Kerr-Newman metric. As the characteristic features of rotating black holes are there without the need to introduce electric charge, we will continue with the no charge case.

The coordinates used in the metric (t, r, θ, ϕ) are known as Boyer-Lindquist coordinates. These coordinates reduce to Schwarzschild coordinates as $a \to 0$ and are related to Cartesian coordinates in Euclidian space as:

$$x = \sqrt{r^2 + a^2} \sin\theta \cos\phi \tag{2.56}$$

$$y = \sqrt{r^2 + a^2} \sin\theta \sin\phi \tag{2.57}$$

$$z = r\cos\theta \tag{2.58}$$

We notice an important difference between the r coordinates of this coordinate system and that of the Schwarzschild coordinates: Here $r = 0$ is not a point, but a ring with radius a.

Just like we did in the RN metric case, we will locate the event horizons by setting $g^{rr} = \Delta/\rho^2 = 0$. Since $\rho^2 \geq 0$ we obtain the quadratic equation

$$\Delta(r) = r^2 - R_S r + a^2 = 0 \tag{2.59}$$

Again in similarity with the RN case, there are three distinct physical regimes for $R_S > 2a$, $R_S = 2a$ and $R_S < 2a$. These regimes are the result of the conflict between the angular motion and gravity. The last regime is the one with too high an angular momentum resulting in a naked singularity. The $R_S = 2a$ case is again an unstable black hole similar to the unstable RN solution case.

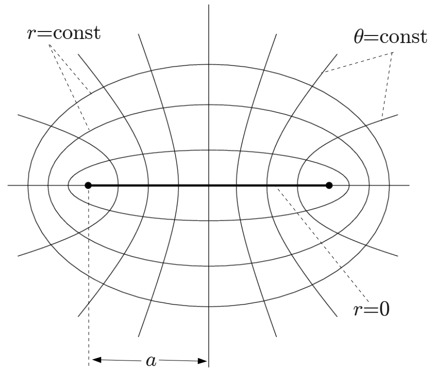

Figure 2.6: Coordinates relevant to rotating black holes.

In the $R_s > 2a$ case, the coordinate singularities are located at:

$$r_{\pm} = R_S/2 \pm \sqrt{R_S^2/4 - a^2}, \tag{2.60}$$

both of which are event horizons (see Fig. 2.7).

There is another singularity in the metric where the purely temporal metric component g_{tt} changes sign from positive to negative. This is called the static limit surface and it's found by solving for $g_{tt} = 0$:

$$r_{sl} = R_S/2 \pm \sqrt{R_S^2/4 - a^2 \cos^2\theta} \tag{2.61}$$

Due to the frame dragging effect, an object close to the black hole must move in the direction of the rotation of the black hole (ϕ direction). Static limit is the surface at which this frame dragging effect is so strong that the particles must move with the speed of light to merely stand still. Note that because of the cosine term, it touches the outer horizon at it's poles.

The volume of space between the static limit and the event horizon surfaces is called the ergosphere. Since ergosphere is outside the event horizon, a particle that enters it, can leave it, actually it can leave with a momentum boost. Therefore it's possible to extract energy from the black hole's rotational kinetic energy by sending an object to this region; this is called a Penrose process. This process is considered to be one of the most powerful energy releasing mechanisms in the nature, like gamma ray bursts.

Inspecting the Kerr metric (2.52), we note that the physical singularity is not at $r = 0$, but at $\rho = 0$ instead. As ρ is the sum of two strictly nonnegative quantities (see Eq.(2.54)), it can only be zero when both r and a are zero, or when $r = 0$ and $\theta = \pi/2$. We have seen before

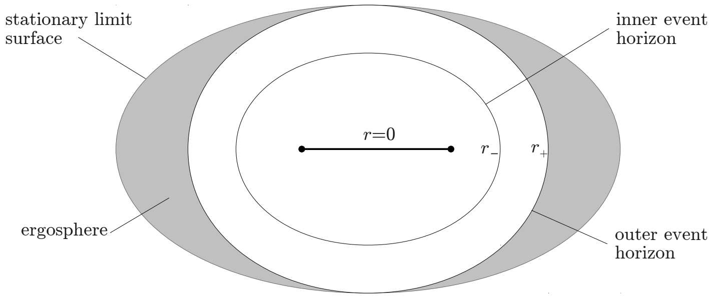

Figure 2.7: Important regions and surfaces of a rotating black hole (side view).

that, $r = 0$ is a disk and imposing $\theta = \pi/2$ gives us the outer ring of this disk. Therefore Kerr solution tells us that rotation turns the point singularity of the Schwarzschild black hole into a circular ring.

Conformal diagram for a Kerr black hole for the $R_S > 2a$ case has been depicted in Fig. 2.8. It's similar to the RN case but there are a few important differences. Firstly the Kerr solution has no spherical symmetry, therefore we will have different geometries for different θ values. Second, there is the possibility to pass through the ring singularity. This will take an observer to a distinct copy of our universe. Third, the region near the ring singularity has closed timelike curves, which means that causality might also be violated in this region.

2.6 Classical Black Hole Thermodynamics

2.6.1 Penrose process

In the previous section we mentioned that it's possible to extract energy from a rotating black hole. This is possible (at least theoretically) by a classical process called the Penrose process. (Fig. 2.9)

To extract energy, one first sends a particle, *particle 0*, into the ergosphere of a rotating black hole. Here it disintegrates into two particles, *particle 1* and *particle 2*. It's possible that the particle disintegrates in a special way, leaving one of the daughter particles, say *particle 1*, with negative energy. This is possible because the energy of a particle is [24]

$$E = -K_\mu p^\mu \tag{2.62}$$

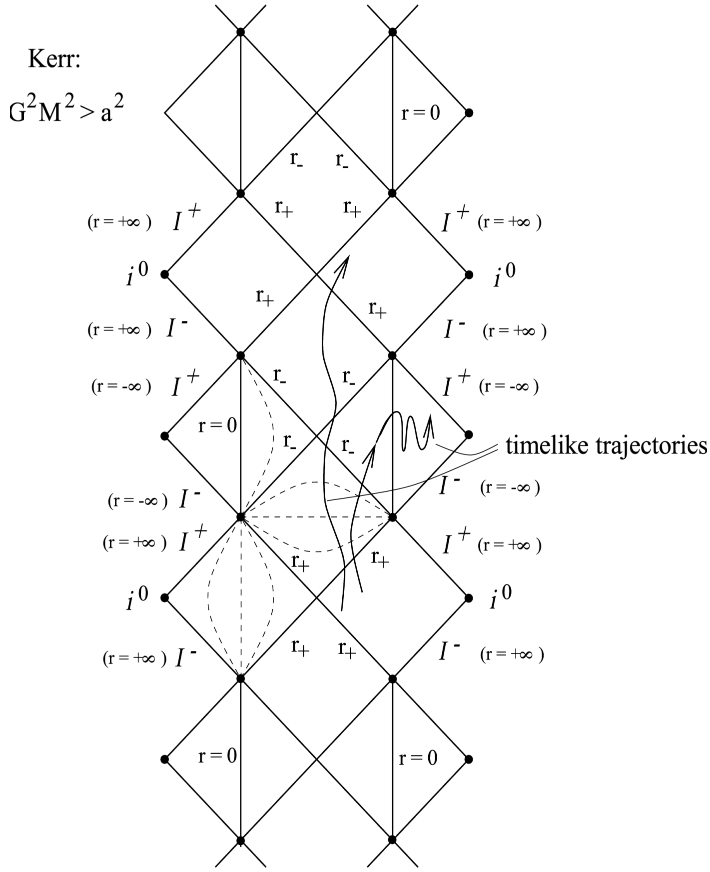

Figure 2.8: Conformal diagram for a Kerr black hole [22].

where $K = \partial_t$ is a Killing vector and p^μ is it's four momentum which can take a negative value in the ergosphere, because in this region K^μ becomes spacelike. Note that here negative energy means that the energy needed to take the particle to infinity exceeds it's rest energy.

After the disintegration, *particle 1* falls into the black hole. At this point, energy conservation dictates that *particle 2* carries more energy than *particle 0*, which has been provided by the black hole. According to Penrose, with a careful choice of the initial trajectory of *particle 0* and also with the disintegration process, *particle 2* can leave the ergoregion and the black hole energy has been extracted.

The change in the black hole mass is equal to the energy of *particle 2*, $\delta M = E^{(2)}$, and similarly the angular momentum of the black hole $J = Ma$ changes as $\delta J = L^{(2)}$. The upper limit on the angular momentum change is written as

$$\delta J < \frac{\delta M}{\Omega_{\rm H}} \tag{2.63}$$

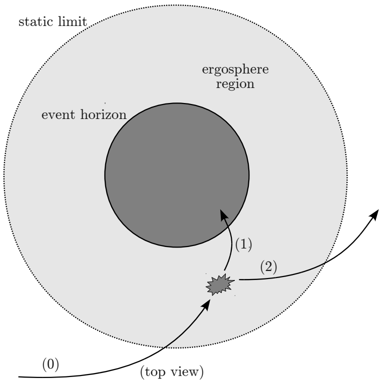

Figure 2.9: Diagram of Penrose process seen as a black hole is viewed from top [24]. *Particle 0* enters the ergoregion and disintegrates in a special way leaving one of the daughter particles with negative energy. One particle (*particle 1*) crosses the horizon while the other (*particle 2*) leaves the ergoregion. Energy conservation requires that *particle 2* has more energy than *particle 0*.

where Ω_{H} is the angular velocity of the event horizon.

Let's define the irreducable mass [24]

$$M_{\mathrm{irr}}^2 = \frac{A}{16\pi G2} \tag{2.64}$$

$$= \frac{1}{2}\left(M^2 + \sqrt{M^4 - J^2}\right) \tag{2.65}$$

where A is the surface area of the outer horizon. The differential of this mass shows how it changes with mass and angular momentum:

$$\delta M_{\mathrm{irr}} = \frac{a}{4GM_{\mathrm{irr}}\sqrt{G^2M^2 - a^2}}(\Omega_H^{-1}\delta M - \delta J) \tag{2.66}$$

using the limit (2.63) in this result shows why M_{irr} is entitled as the irreducable mass:

$$\delta M_{\mathrm{irr}} > 0 \tag{2.67}$$

A direct consequence of this inequality is that the surface area A of a black hole cannot decrease. This is actually a very important result. By computing the change in surface area δA using (2.64) and (2.66), we can write the relation

$$\delta M = \frac{\kappa}{8\pi}\delta A + \Omega_{\mathrm{H}}\delta J \tag{2.68}$$

where κ is the surface gravity of the Kerr solution. There is a profound similarity with this result and the first law of Thermodynamics

$$\delta E = T\delta S + P\delta V \tag{2.69}$$

which eventually led to the concept of black hole thermodynamics.

There are the following correspondences between the variables of the two theories:

$$E \leftrightarrow M \tag{2.70}$$

$$S \leftrightarrow A/4 \tag{2.71}$$

$$T \leftrightarrow \kappa/2\pi \tag{2.72}$$

It's been understood that there is actually a one to one correspondance between the rules of black hole mechanics and thermodynamics. We will now review them briefly:

The zeroth law For a stationary black hole, the surface gravity κ is constant over the event horizon.

The analogue law is the zeroth law of thermodynamics, the temperature T is constant throughout a system which is in thermal equilibrium. This law has an extended form which implies that Ω_{H} and the electrostatic potential Φ are also constant over the event horizon.

The first law The changes in the black hole mass M, area A, angular momentum J, and electric charge Q are related as

$$\delta M = \frac{\kappa}{8\pi}\delta A + \Omega\delta J + \Phi\delta Q \tag{2.73}$$

Which has been dictated by the conservation of energy.

The second law The surface area A of a black hole event horizon cannot decrease.

This is the Hawking's area theorem. The analogy with the second law of thermodynamics, which states that the entropy S of a closed system cannot decrease, implies a profound connection between the surface area A and the entropy S.

This law has been modified because a black hole can actually radiate energy with the Hawking radiation process which causes it to lose mass and the horizon area to decrease. A generalized version of the second law states that the total entropy of the BH plus the environment system cannot decrease.

The third law The surface gravity κ cannot be reduced to zero.

This is analogous to the weak form of the third law of thermodynamics, which states that the temperature T of a system cannot be reduced to absolute zero in a physical process. The strong form of this law states that the entropy S of a system goes to zero as it's temperature T goes to absolute zero, and there is no analogue of this version of the third law in black hole mechanics.

2.7 The Evaporating Black Hole

Incorporation of quantum mechanics into black hole physics leads to a number of interesting results. One such result is that the black holes are not exactly black, they must be radiating energy in the form of Hawking radiation. Hawking radiation is a thermal process which is a purely quantum phenomenon that can only happen in a region of space with very strong gravity. The mechanism says that all types of elementary particles should be radiated, and their energy-momentum distribution must follow the Planck distribution, with the corresponding temperature of BH being called it's Hawking temperature. Hawking temperature of a BH is inversely proportional to it's mass.

Unruh effect has been discovered in attempts to further understand the Hawking radiation mechanism. We will begin our Hawking radiation discussion by summarizing the Unruh effect.

2.7.1 Unruh Effect

To simplify things, we will confine ourselves to one spatial and one time coordinate. Consider an observer moving with uniform acceleration of magnitude α in the x–direction, in flat space which is described by the metric:

$$\mathrm{d}s^2 = -\mathrm{d}t^2 + \mathrm{d}x^2 \tag{2.74}$$

The observer's worldline can be parametrized by it's proper time τ as follows

$$t(\tau) = \frac{1}{\alpha}\sinh(\alpha\tau) \tag{2.75}$$

$$x(\tau) = \frac{1}{\alpha}\cosh(\alpha\tau) \tag{2.76}$$

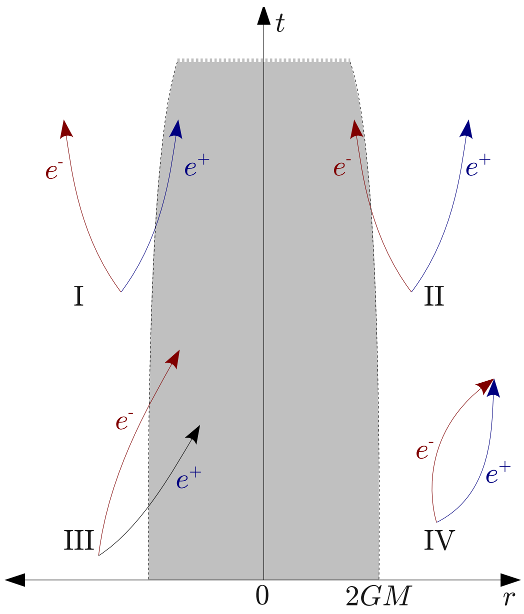

Figure 2.10: Hawking radiation process. Virtual particle-antiparticle pairs are created and annihilated around the event horizon of the black hole all the time. Both members of the pair may fall into the black hole (III) or might annihilate before falling (IV). However one particle or antiparticle may move away to infinity while it's negative energy partner falling into the black hole (I, II). Overall, the black hole is radiating away particles and losing it's mass, therefore is effectively evaporating.

which obeys the relation

$$x^2(\tau) = t^2(\tau) + \alpha^2 \tag{2.77}$$

This is the equation for a hyperbola. Notice that this worldline asymptotes to null paths $x = \pm t$ both in the past, and the future. Therefore the trajectory of an accelerated observer travels from past null infinity ($\mathcal{I}^-$) to future null infinity ($\mathcal{I}^+$), not the timelike infinity like inertial observers. This is our starting point.

Now let's choose a new set of coordinates (η, ξ) on the two dimensional Minkowski space. We define these coordinates as follows:

$$t = \frac{1}{a} e^{a\xi} \sinh(a\eta), \qquad x = \frac{1}{a} e^{a\xi} \cosh(a\eta) \qquad (x > |t|) \tag{2.78}$$

where a is a constant. The set of coordinates (η, ξ) is called the Rindler coordinates. In terms of these coordinates, the constant-acceleration path becomes

$$\eta(\tau) = \frac{\alpha}{a}\tau \tag{2.79}$$

$$\xi(\tau) = \frac{1}{a} \ln\left(\frac{a}{\alpha}\right) \tag{2.80}$$

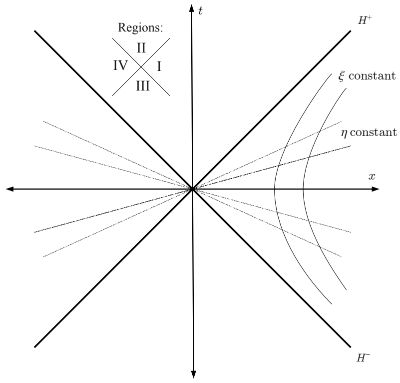

Figure 2.11: Minkowski spacetime in Rindler coordinates η and ξ. $H^{\pm}$ are Cauchy horizons.

Which is a rather simple form; η is proportional to proper time and ξ is constant. Let the observer be traveling with $\alpha = a$. Then

$$\eta = \tau, \qquad \xi = 0 \tag{2.81}$$

which shows that η is nothing but another name for τ. Metric is written in these coordinates as

$$\mathrm{d}s^2 = e^{2a\xi}(-\mathrm{d}\eta^2 + \mathrm{d}\xi^2) \tag{2.82}$$

Rindler coordinates on Minkowski space have been depicted on Fig. 2.11. These coordinates have the ranges $\eta > -\infty$, $\xi < +\infty$ therefore they cover the wedges I and IV in Fig. 2.11. Wedge I is known as the Rindler space, but it's obviously just a part of the Minkowski space. An observer moving along a constant acceleration path is also called a Rindler observer.

We want to study how a Rindler observer sees the particle content of the Minkowski vacuum. We will continue working in two dimensions (one space and one time). Let's start with the simplest case of a massless scalar field ϕ. The relevant wave equation is the KG equation:

$$\partial_\mu \partial^\mu \phi = 0 \tag{2.83}$$

Where the scalar field ϕ is a quantum operator. This equation has the following orthonormal positive frequency solutions:

$$f_\omega(t,x)^{\pm} = \frac{1}{\sqrt{2\omega}} e^{-i\omega(t\mp x)} \tag{2.84}$$

where we used the dispersion relation $\omega = +|k|$. f^+ represents outgoing waves while f^- are ingoing. Positive energy solutions are eigenfunctions of the energy operator with positive eigenvalue:

$$i\frac{\partial}{\partial t} f_\omega = \omega f_\omega \tag{2.85}$$

They are orthogonal in the following sense:

$$(f_\omega, f'_\omega) = \delta(\omega - \omega') \tag{2.86}$$

We will expand ϕ in this basis. To make the outgoing and ingoing modes clearer, we will switch to null coordinates.

In null coordinates defined as $u = t - r$ and $v = t + r$, Minkowski metric becomes

$$\mathrm{d}s^2 = -\mathrm{d}u\mathrm{d}v \tag{2.87}$$

Null coordinates of the Rindler observer u' and v' transform as

$$\mathrm{d}s^2 = -\mathrm{d}u\mathrm{d}v = -e^{a(v'-u')}\mathrm{d}u'\mathrm{d}v' \tag{2.88}$$

and the modes for the inertial observer become:

$$f^+_\omega(u) = \frac{1}{\sqrt{2\omega}} e^{-i\omega u}, \qquad f^-_\omega(v) = \frac{1}{\sqrt{2\omega}} e^{-i\omega v} \tag{2.89}$$

We must write a different basis for the Rindler observer because it's coordinates u' and v' are different than u and v.

$$g^+_\omega(u') = \frac{1}{\sqrt{2\omega}} e^{-i\omega u'}, \qquad g^-_\omega(v') = \frac{1}{\sqrt{2\omega}} e^{-i\omega v'} \tag{2.90}$$

The field ϕ can now be expanded in the inertial observer's frame as

$$\phi = \int \mathrm{d}\omega \left[a_\omega f^+_\omega + a^\dagger_\omega (f^+_\omega)^* + c_\omega f^-_\omega + c^\dagger_\omega (f^-_\omega)^* \right] \tag{2.91}$$

where the coefficients a, $a^\dagger$, c and $c^\dagger$ are the creation and annihilation operators.

When annihilation operator acts on a vacuum state, it gives zero:

$$a_\omega |0\rangle = 0, \tag{2.92}$$

and creation operator acted on a vacuum yields a vacuum state carrying fields of energy ω. Therefore the state

$$(a^\dagger_\omega)^n |0\rangle = |n_\omega\rangle \tag{2.93}$$

represents a vacuum containing n particles of energy ω. The number operator is

$$N = a^\dagger_\omega a_\omega \tag{2.94}$$

whose expectation value is:

$$\langle n_\omega | a^\dagger_\omega a_\omega | n_\omega \rangle = \langle n_\omega | N_\omega | n_\omega \rangle = n_\omega \tag{2.95}$$

Now we will introduce a second basis of solutions to the wave equation, $\{g_\omega, g^*_\omega\}$. We can expand ϕ in this basis as well

$$\phi = \int \mathrm{d}\omega \left[b_\omega g^+_\omega + b^\dagger_\omega (g^+_\omega)^* + d_\omega g^-_\omega + d^\dagger_\omega (g^-_\omega)^* \right] \tag{2.96}$$

note that the operators b and $b^\dagger$ above operate on a different vacuum state.

The two bases are related by Bogoliubov transformations:

$$g_\omega = \int \mathrm{d}\omega' (\alpha_{\omega\omega'} f_{\omega'} + \beta_{\omega\omega'} f^*_{\omega'}) \tag{2.97}$$

$$f_\omega = \int \mathrm{d}\omega' (\alpha^*_{\omega'\omega} g_{\omega'} - \beta_{\omega'\omega} g^*_{\omega'}) \tag{2.98}$$

the coefficients α and β are called the Bogoliubov coefficients, and can be computed with the inner products

$$\alpha_{\omega\omega'} = (g_\omega, f_{\omega'}), \qquad \beta_{\omega\omega'} = -(g_\omega, f^*_{\omega'}) \tag{2.99}$$

and

$$_{\mathrm{in}}\langle 0 | N^{\mathrm{out}}_\omega | 0 \rangle_{\mathrm{in}} = {}_{\mathrm{in}}\langle 0 | b^\dagger_\omega b_\omega | 0 \rangle_{\mathrm{in}} = \int \mathrm{d}\omega' |\beta_{\omega\omega'}|^2 \tag{2.100}$$

therefore, even if there are no particles in the <u>in</u> vacuum, there may be particles in the <u>out</u> vacuum.

$$n(\omega') = \int |\beta_{\omega'}(\omega)|^2 \mathrm{d}\omega \tag{2.101}$$

Evaluating the integral one finds

$$n(\omega') = \frac{1}{e^{2\pi\omega'/a} - 1} \tag{2.102}$$

With the corresponding temperature expression

$$T = \frac{a}{2\pi} \tag{2.103}$$

this represents a thermal spectrum:

$$n(\omega)\mathrm{d}\omega = \frac{1}{e^{\omega/T} - 1}\mathrm{d}\omega \tag{2.104}$$

Note that the Boltzmann constant $k_B = 1$ in the system of units we use. The associated temperature can be found as:

$$T = \frac{a}{2\pi} \tag{2.105}$$

As the metric components are independent of η, we know that ∂_η is a Killing vector. By using the definition of the redshift factor in terms of the Killing vector $V = \sqrt{-K_\mu K^\mu}$, we find

$$V = e^{a\xi} \tag{2.106}$$

and the surface gravity $\kappa = \sqrt{\nabla_\mu V \, \nabla^\mu \, V}$ at this Killing horizon is

$$\kappa = a. \tag{2.107}$$

2.7.2 Hawking Radiation

Consider a nonrotating observer sitting at fixed radius r outside of a Schwarzschild black hole. As the observer is at fixed radial position, equivalence principle says that it's accelerating away from the black hole, therefore it's a Rindler observer. The redshift factor of the observer $V^2 = -K_\mu K^\mu$ (where $K = \partial_\mu$ is the time-translation Killing vector) is:

$$V = \sqrt{1 - \frac{2M}{r}} \tag{2.108}$$

and the corresponding acceleration is

$$a = \frac{M}{r\sqrt{r - 2M}} \tag{2.109}$$

which attains very large values as $r \to R_\mathrm{S}$, compared to the scale set by the Schwarzschild radius:

$$a \gg \frac{1}{2M} \tag{2.110}$$

For an accelerating observer whose length and timescales set by $a^{-1} \ll 2M$, spacetime looks essentially flat. Therefore the spacetime around the event horizon can be considered flat.

So we expect the quantum state of some scalar field ϕ look like the Minkowski vacuum (free of any particles) as seen by accelerated observers near the black hole, if the quantum field is in a state which is regular near the horizon. Therefore the accelerated observer will experience the Unruh effect: The observer will be seeing the flat vacuum as a thermal state at a temperature $T = a/2\pi$.

Let's extend this local thermal bath to infinity. The outgoing modes of this thermal state will be redshifted as they climb away the gravity well of the black hole. Static observers at two different radii measure the temperatures $T_2/T_1 = \xi_1/\xi_2$, where ξ is the norm of the time-translation Killing field.

As we have $\xi_\infty = 1$ at infinity, the radiation reaches the infinity and we have a blackbody radiator with (Hawking) temperature $T_\infty = \kappa/2\pi$ at the rest frame of the black hole.

The number of i-type particles that reach infinity is:

$$N_i = \frac{\Gamma_i}{e^{\omega/T_{\mathrm{H}}} - 1} \tag{2.111}$$

where Γ_i is the greybody factor, which accounts for the emissivity of the black hole. Emitted particles may backscatter because of the angular momentum barrier and spacetime curvature, so a black hole is not a perfect blackbody.

Stefan-Boltzmann law gives the rate of energy radiated away from the black hole

$$\frac{\mathrm{d}E}{\mathrm{d}t} \simeq -\sigma A T_{\mathrm{H}}^4 \tag{2.112}$$

where σ is Stefan's constant and A is black hole's surface area.

Since in our units

$$E = M, \qquad A = M^2, \qquad T_H \sim \frac{1}{M} \tag{2.113}$$

we have

$$\frac{\mathrm{d}M}{\mathrm{d}t} \sim \frac{1}{M^2} \tag{2.114}$$

where σ is Stefan's constant and A is black hole's surface area.

Therefore lifetime of the black hole is:

$$\tau \sim M^3. \tag{2.115}$$

CHAPTER 3

QUANTUM BLACK HOLES

3.1 Introduction

We discussed in Chapter 1 that the gravitational coupling getting stronger at short distances suggests a solution to the hierarchy problem. However this scenario has consequences that goes beyond the hierarchy problem, implications in the domain of black hole physics. If gravity gets stronger in short distances, than the Schwarzschild radius R_{S} associated with a body of mass must also change.

In 2001, Greg Landsberg and Savas Dimopoulos noticed this implication and calculated R_{S} assuming the existence of n ADD type extra dimensions:

$$r_{s(4+n)} = \frac{1}{\sqrt{\pi} M_{(4+n)}} \left(\frac{M_{\mathrm{BH}}}{M_{(4+n)}} \left(\frac{8\Gamma((n+3)/2)}{n+2} \right) \right)^{\frac{1}{n+1}} \tag{3.1}$$

where M_{BH} is the black hole mass [20]. Comparison of this expression with 4-dimensional R_{S} for the same mass shows that $r_{s(4)} < r_{s(4+n)} < R$, where R is the common radius of n extra dimensions [25]. Therefore, if the ADD model is true, same mass corresponds to larger Schwarzschild radius, which eventually is “easier” to form into a black hole. The interesting implication of this discovery is the possibility of tiny black hole production at the LHC, since LHC will collide protons at center of mass (CM) energies high enough to form tiny, higher-dimensional, or quantum black holes.

Horizon radii of such black holes for different number of extra dimensions can be found on Table 3.1.

It might be argued that the quantum black hole channel is the one which suffers the most from the lack of a complete theory of quantum gravity. Their being (theoretical) objects with sizes close to the extra dimension sizes, and having mass close to the energy scale of the underlying theory leaves a wide room for speculations. Such research areas are occasionally called “speculative science”. The content of this chapter will be the major points of black hole physics on which there are broad consensus. We are beginning our discussion with the formation of quantum black holes.

3.2 Black Hole Formation

Formation analyses of quantum black holes start with the assumption that the collisions with energies $E \gg M_{(4+n)}$ should correspond to the classical limit of the fundamental quantum gravity theory. This assumption allows the use of the semiclassical “black disk” approximation in cross-section calculations. According to this approach, when two partons collide with an impact parameter $b < R_{\rm S}$, collision results with the formation of a black hole (Fig. 3.1). The parton level cross section for black hole production calculated via this approximation is given as [20, 27]:

$$\sigma(M_{\rm BH}) = \pi r^2_{s(4+n)} = \frac{1}{M^2_{(4+n)}}\left(\frac{M_{\rm BH}}{M_{(4+n)}}\left(\frac{8\Gamma((n+3)/2)}{n+2}\right)\right)^{\frac{2}{n+1}} \tag{3.2}$$

The total cross-section is written in the parton luminosity approach as:

$$\frac{d\sigma(pp \to {\rm BH} \to X)}{dM_{\rm BH}} = \frac{dL}{dM_{\rm BH}}\sigma(ab \to {\rm BH})\Big|_{s=M^2_{\rm BH}} \tag{3.3}$$

where the parton luminosity $dL/dM_{\rm BH}$ is a sum over all parton types

$$\frac{dL}{dM_{\rm BH}} = \frac{2M_{\rm BH}}{s}\sum_{a,b}\int_{M^2_{\rm BH}/s}^{1}\frac{dx_a}{x_a}f_a(x_a)f_b(M^2_{\rm BH}/sx_a) \tag{3.4}$$

which are weighed by the parton distribution functions $f_i(x_i)$.

There are other sources of quantum black hole production on earth too. For example collisions of high energy cosmic rays with nuclei in the upper atmosphere have enough CM energy for

Table 3.1: Horizon radii for 5 TeV black holes in the large extra dimension model with $M_{(4+n)}$ = 1 TeV, for different values of extra dimensions [26]. Note that the protons’s radius is ~ 1 fm.

n	1	2	3	4	5	6	7
$R_{\rm S}$ ($\times 10^{-4}$ fm)	4.06	2.63	2.22	2.07	2.00	1.99	1.99

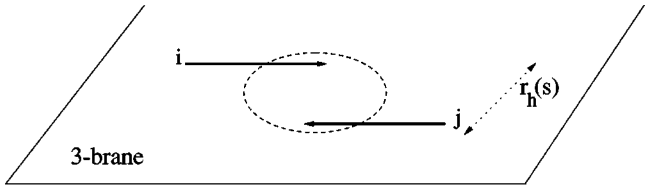

Figure 3.1: In the semiclassical view, a black hole is formed when the impact parameter of two colliding partons is smaller than the Schwarzschild radius corresponding to their center of mass energy $\sqrt{s}$ [27].

BH formation. Especially the neutrinos being scattered by nuclei are expected to be the most effective sources of black hole production because of the absence of any QCD-type contaminating effects and their small SM cross-sections [28–31].

3.3 Decay of black holes

Once formed, black holes are predicted to decay mainly through the Hawking radiation mechanism in very short time scales. It's widely accepted that the time evolution of quantum black holes should consist of a number of distinguishable, consecutive stages:

Balding phase When formed, the black hole has very high multipole moments of gravitational, electromagnetic and other fields. These are collectively called it's "hair", which, according to the "No hair" theorem, a black hole cannot carry. Therefore the first evolution stage of a black hole is to shed it's hair; hence the name balding phase. In the $E \gg M_D$ limit, this will essentially be a classical process, taking place in a time scale of $t \approx R_S$. In this stage the black hole will also shed the charges it carry by gauge radiation, possibly through the Schwinger process. What remains after this phase is a rotating, Kerr black black hole.

Spin-down phase Probability to form a zero angular momentum black hole is nearly zero, because this requires the impact parameter to be zero. Therefore all quantum black holes will be formed with some spin. However, a spinning black hole state is unstable and it tends to become more and more a Schwarzschild black hole by shedding its spin. Therefore the second stage of BH evolution is the spin-down stage, in which the black hole loses its angular momentum through Hawking radiation and superradiance. Once this stage ends, the resulting object is a spherically symmetric, static, Schwarzschild black hole

Schwarzschild phase The now spherically-symmetric black hole emits Hawking radiation [32], and loses energy. This is the best understood stage of BH decay from the theoretical point of view. As the BH radiates energy, it loses mass and becomes hotter. This stage ends when the BH's mass closes to the Planck mass where quantum gravity effects become important.

Planck phase The details of this stage are completely unknown as they are governed by quantum gravity effects. For this very reason this is also a very important stage because it has the potential to give valuable information about QG. The possible scenarios about this stage can be listed as follows:

- The black hole completely decays into a number of high p_T particles with energies E $\sim M_D$.
- Black hole decay stops with a stable decay relic. The black hole completely decaying into statistically distributed particles could violated unitarity. Such relics should leave a missing transverse energy signature in the event. Also as most of the BHs will be formed from $q-q$ collisions, these relics will tend to be charged, and their passage through the detector should be observable in the tracker and the muon detectors.

3.4 Details of the Schwarzschild Phase

Hawking radiation, which is the major part of this stage has been detailed in Section 2.7.2. It is a thermal process in which the four momenta of the radiated particles are determined by the Hawking temperature T_H of the black hole, and the corresponding Planck distribution. Final state particle species are chosen democratically (with equal ratios) to all Standard Model particles. If the theories predicting them are correct, BH decays will produce Higgs or SUSY particles, or if they exist, any other BSM particles too.

The Hawking temperature for a (4+n)-dimensional black hole is:

$$T_{(4+n)} = \frac{(n+1)}{4\pi R_S} \tag{3.5}$$

where R_S is the Schwarzschild radius. Written explicitly the expression becomes

$$T_{(4+n)} = M_{(4+n)} \left(\frac{M_{(4+n)}}{M_{BH}} \right)^{\frac{1}{n+1}} \left(\frac{(n+1)^{n+1}(n+2)}{2^{2n+5}\pi^{(n+1)/2}\Gamma((n+3)/2)} \right)^{\frac{1}{n+1}} \tag{3.6}$$

Calculated temperature values for 5 TeV black holes for different n values have been listed on Table 3.2. It's important to note that the energy spectrum of the emitted particles follows the Planck distribution. As the peak of the distribution is around the temperature value, the temperature represents the most probable energies of the emitted particles. However note that for a specific particle to be emitted, the black hole's temperature must exceed it's rest mass ($T_H \geq m$). Also note that as the black hole decays, it's temperature increases due to the decreasing mass.

Table 3.2: Hawking temperatures of $M = 5$ TeV black holes for different number of extra dimensions. Extra dimension model is for $M_{(4+n)} = 1$ TeV. [26]

n	2	3	4	5	6	7
T_H (GeV)	179	282	379	470	553	629

Lifetime of the black hole can be found from the temperature expression:

$$\tau_{(4+n)} \sim \frac{1}{M_{(4+n)}} \left(\frac{M_{BH}}{M_{(4+n)}} \right)^{\frac{n+3}{n+1}} \tag{3.7}$$

A comparison of Eqs. (3.6) and (3.7) with their 4-dimensional equivalents show that, for the same M_{BH}, the (4+n)-dimensional black hole is warmer, hence it decays faster than the 4-dimensional black hole [25]. As a note, typical Hawking temperature for a (4+n)-dimensional black hole accessible at LHC energies is $\sim 10^{15}$ K, which corresponds to a lifetime of about $\sim 10^{-26}$ seconds.

To compare, the lifetime of stellar black holes which have a mass $M > 10^{15}$ g, exceeds the age of the universe ($\sim 10^{10}$ years) [33]. The Hawking temperature of supermassive black holes ($M > 10^{27}$ g) is even lower than the CMB temperature which is about 3 K, so they don't evaporate at all.

An important question is what fraction of particles will be emitted to the bulk in the form of gravitons. The importance of the question is in the overall multiplicity suppression and increased missing energy in such a case. To address this issue we remember that the Hawking radiation mechanism has a democratic nature; the particle emission probabilities are close for each elementary particle. Since SM has 60 elementary particles (or 61 with the Higgs), the graviton emission probability is only $\sim 2\%$. Note that this probability will be even lower if there are other elementary particles with mass less than average BH temperatures, because they will be emitted too. In conclusion, graviton emission to bulk is more or less omissable and most of the radiation should go into the brane.

Concerning the Hawking radiation mechanism, the number of particles emitted per unit time is written for n dimensions as follows:

$$\frac{\mathrm{d}N^{(s)}(\omega)}{\mathrm{d}t} = \sum_j \sigma^{(s)}_{j,n}(\omega)\frac{1}{e^{\omega/T_H} \pm 1}\frac{\mathrm{d}^{n+3}k}{(2\pi)^{n+3}} \tag{3.8}$$

One difference from the 4D case is the appearance of the $\sigma^{(s)}_{j,n}$ term in the higher dimensional case. This term can significantly modify the spectrum and is called the greybody factor. Note that it's a function of spin, angular momentum, and the energy of the particle, also the number of dimensions n. This factor is due to the strong gravitational background a particle has to pass through as it reaches an observer at infinity. In effect it represents the transmission cross-section for a particle travelling in the gravitational field of the black hole.

3.5 Indirect Indications of Black Hole Production

In the next chapter we will present our study on the detection of black hole events, directly from their decays. However there are indirect indications of black hole production too. One such indication should be the observation of a sharp cutoff in the dijet events jets when the invariant mass exceeds the Planck mass [34]. At energies lower than the Planck scale, it's expected that the black hole production is exponentially suppressed due to the string excitations or other quantum effects. Therefore the production is expected to start when the CM energy exceeds the Planck mass, and the dijet events will be suppressed as these collisions are now forming into black holes Fig. 3.2.

In fact for this very reason the BH production might render the probing of smaller distance scales impossible, as the higher energy particle beams needed to probe lower distance scales will all end up in black holes after the collisions [27]. In this sense BH production, if true, will have a destructive effect in future collider experiments.

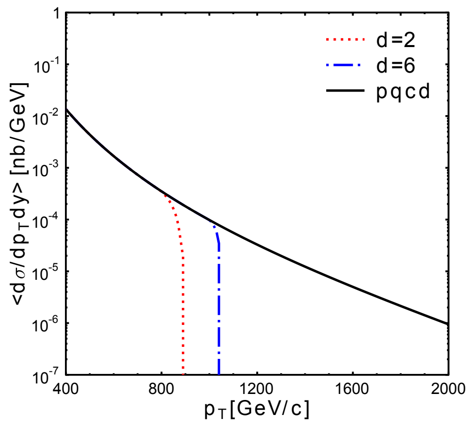

Figure 3.2: The expected affect of BH production on the distribution of high energy jets [33]. Here the jet distributions are for $\sqrt{s}$ = 14 TeV and the ADD scenario is with $M_{(4+n)}$ = 1 TeV. Notice that the cutoff should happen at energies close to the Planck mass, but it's not very sensitive to the number of extra dimensions, d.

Another indirect indication of BH production will be a numerically similar increase in the total production rates of all types of elementary particles. For example the BH should emit, Higgs and SUSY particles too, and an overall increase in their production rates (if they exist) will signal black hole decays.

3.6 How Safe is Black Hole Production on Earth?

LHC started to operate and the world is just the way as it used to be[1]. This was in fact the conclusion of the LHC Safety Assessment Group that performed an extensive study of the safety of high energy collisions at the LHC [35], along with other studies such as [36]. What was studied by the LHC Safety Assessment Group was not limited to only black holes, but the possibility of any catastrophic phenomenon connected to the LHC collisions. Since the LHC is currently operating at half it's design energy, we want to briefly review why LHC poses no safety risks to the Earth. Our discussion will be limited to quantum black hole production.

Most important argument against the possibility of catastrophic results for the Earth is the constant bombardment of the upper atmosphere by energetic cosmic rays. Part of the collisions of these particles (which are mainly protons and neutrinos) with atoms and molecules at the upper atmosphere are more energetic that those of the LHC. Since the Earth is about

[1] still no BSM signatures too, but probably it's too early to expect that

4.5 billion years old, either there is no black hole production, or the production ends with a quick decay (in about 10^{-26} s) as theoretically foreseen. In fact, concerning the cross-section area for cosmic ray collisions, earth is a very small object. Jupiter and Sun have a much larger cross-section area and these stellar objects are obviously fully intact. In fact collisions much more energetic than the LHC collisions are happening all around the universe, it is estimated that the universe performs total number of collisions corresponding to the whole LHC programme, 3×10^{13} times every second, and already performed 10^{31} times since the beginning of the universe. There is no observational evidence of a catastrophic event caused by tiny black holes in the universe.

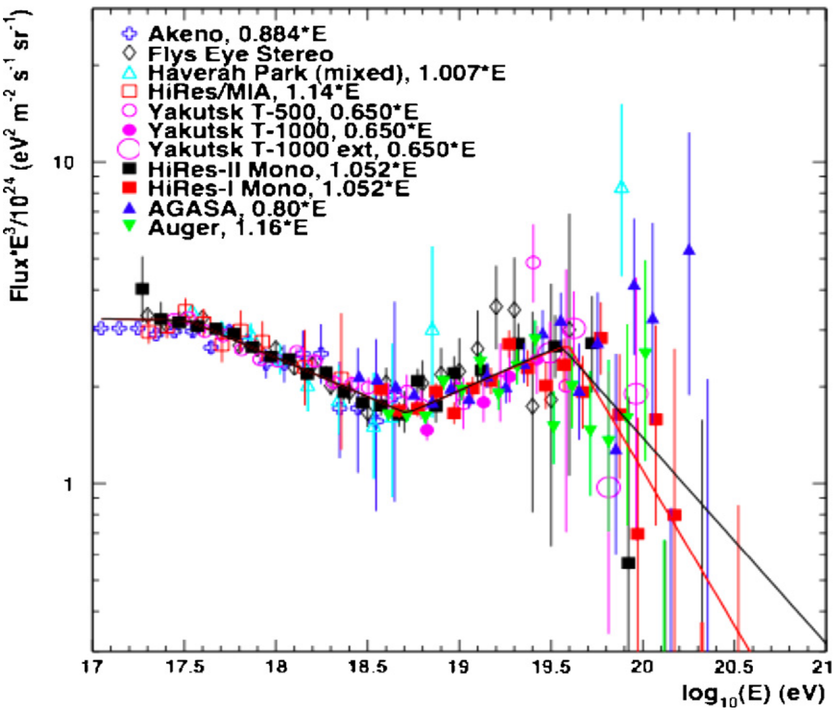

Figure 3.3: Flux distribution of high energy cosmic rays versus energy, as measured by several experiments [35]. Notice that the plot starts with cosmic rays of energy 10^{17} eV. The CM energy of the collisions of a cosmic ray with this energy with a particle of mass $m \approx 1$ GeV in the lab frame is $\sqrt{s} \approx \sqrt{2Em} \approx 100$ TeV, which is a comparable value to LHC collisions.

According to the experimental observations, the highest energy cosmic rays detected have energies around 10^8 TeV (see Fig. 3.3). Also cosmic rays with an energy of 10^5 TeV hit every square centimeter area of earth with a flux of 5×10^{-14} per second, from all directions; with this energy corresponding to 14 TeV center of mass energy when a collision with a fixed target is considered. Earth's surface area is about 5×10^{18} cm^2 and the age of the Earth is about 4 billion years. The result is a total of $\sim 3 \times 10^{22}$ cosmic ray collisions, having a CM energy equal or greater than the energy of the LHC collisions, have already happened on the Earth. LHC collisions will be harmless because all the billion years time of cosmic bombardmand never ended with catastrophic consequences of any kind for the Earth.

The black holes to be produced at the LHC are expected to decay with the Hawking Radiation mechanism. This effect has not been observed so far because of the need for extremely sensitive equipment for it's detection, however, there is broad consensus among the physics community that the Hawking effect is valid. What's more, regardless of the validity of this mechanism, it's known that a physical object created from colliding elementary particles must also be able to decay back to them [37].

One difference of LHC collisions from the cosmic ray collisions is that, unlike the cosmic events, the LHC collisions may produce nearly stationary black holes. Cosmic ray black holes could have been created, but maybe they went through the earth and left it before having a chance to accrete it. What if a stationary black hole starts accreting Earth's matter?

The answer to this question is in the stability of ultra dense stellar objects, such as white dwarves and neutron stars. These objects have matter densities high enough to stop black holes produced in cosmic ray collisions. However lifetimes of observed high density stellar objects show that possible tiny black holes do not accrete and turn them into small black holes.

3.7 First Limits on Quantum Black Hole Production

With the start of proton collisions with 7 TeV CM energy at the LHC, first results from quantum black hole searches from the CMS experiment are now available [38]. The results show no deviations from the SM predictions, and agree well with the QCD multijet processes which are the main background of the black hole signal. Therefore limits on model parameters have been set. According to these limits, depending on the number of extra dimensions, minimum black hole mass can be in the range of 3.5-4.5 TeV for Planck mass values in the range of 1.5-3.5 TeV. The exclusion regions have been shown on Fig. 3.4.

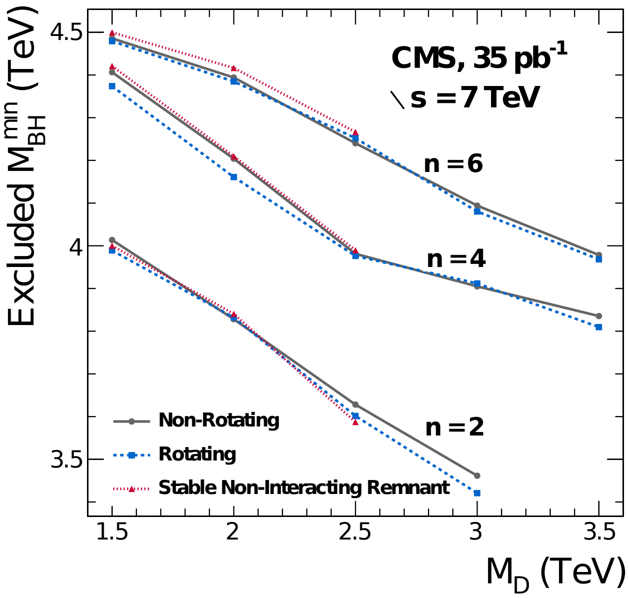

Figure 3.4: 95% confidence level limits set on the model parameters by the CMS experiment from 35 pb^{-1} of collected data. Parameter points below the lines are excluded.

CHAPTER 4

OBSERVING QUANTUM BLACK HOLES

4.1 LHC

We will begin our discussion of experimental detection efforts for quantum black holes by describing the Large Hadron Collider (LHC). LHC is a proton and heavy ion (Pb^{+}) collider [39]. It's being hosted at the international CERN laboratory, which is on the Swiss-French border near Geneva, Switzerland (Figs. 4.1(a) and 4.1(b)). By the time this thesis is written, LHC was the world's most powerful particle accelerator, accelerating protons to 3.5 TeV energy, while the second most powerful accelerator Tevatron at FermiLab accelerating protons and antiprotons up to 0.98 TeV energy.

Main purpose in building the LHC is to discover the Higgs particle, as Higgs physics is of vital importance for the standard model. LHC is also a long awaited tool to allow physicists to test beyond the standard model (BSM) theories and explore physics in energies up to 14 TeV. Some highlights from the physics agenda of LHC can be listed as follows:

- Search for the Higgs particle up to a mass of 1 TeV. Measure it's properties if discovered, set limits on it's mass otherwise.
- Search for SUSY particles with mass up to 2−3 TeV.
- Search for extra spatial dimensions and various associated phenomena (e.g. black holes and graviton production). Relevant physics models are ADD (Arkani-Hamed, Dvali-Dimopoulos), RS (Randall-Sundrum) and UED (Universal Extra Dimensions).
- Test other BSM theories (which is a long list), and search for any other theoretically unforeseen BSM phenomena.

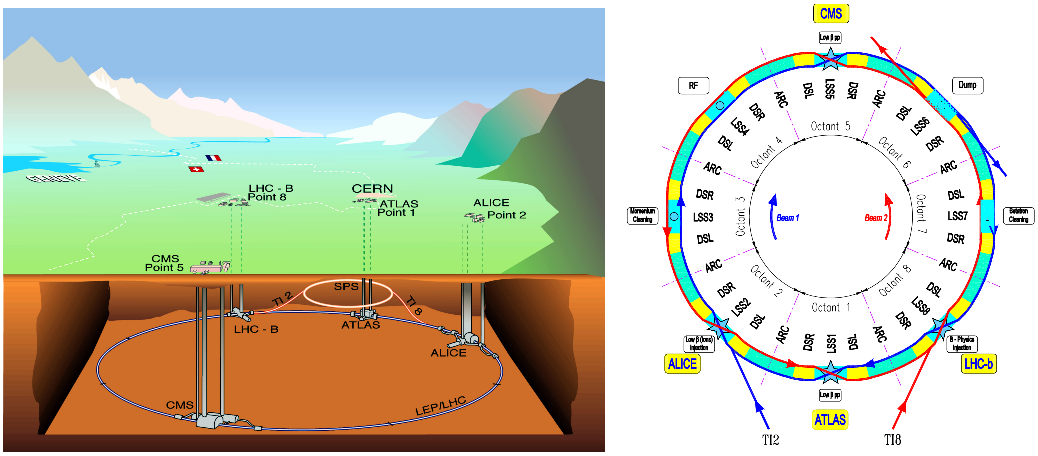

(a) (b)

Figure 4.1: (a) The Large Hadron Collider (LHC) is being hosted at the international CERN laboratory at Genève, Switzerland. It's been constructed in the former LEP tunnel. The tunnel is situated in the large plain area between the Jura mountains (France) and the Salev mountain/Lake Leman (Switzerland). It has a circumference of 27 km and a depth ranging from 50 m to 175 m. Three of the four major experiments, and a large portion of the main ring are situated in France. (b) The LHC ring consists of 8 octants/sections. Locations marked with stars are where collisions take place. Protons from SPS are injected to LHC at points 2 and 8 (TI2 and TI8). Accelerating cavities are situated at octant 4. It's still possible to see the LEP era detector DELPHI in the cavern at point 8, which currently hosts the LHCb experiment.

- Precision measurements of the CKM matrix components in the *b* sector to understand CP violation and explain the observed matter-antimatter imbalance in the universe.
- Search for quark-gluon plasma by recreating big bang conditions in heavy ion collisions.
- Study QCD and diffractive (forward) physics in TeV energies.
- Improve the precision of various SM parameter measurements, e.g. vector boson masses.

There are many factors that led to the current design of the LHC. Among these, two of them might be considered to have the deepest impact. First is obviously the cost, which happens to be the prime motivation to use the former LEP tunnel, also determining that the LHC is a synchrotron type accelerator. Second is the collision energy requirement; the machine had to provide collisions energetic enough to allow discovery of Higgs particle with mass up to 1 TeV, novel SM phenomena e.g. strong interaction region of weak interactions, or BSM phenomena like extra dimensions and Supersymmetry (SUSY).

In circular accelerators, accelerated particles lose energy in the form of synchrotron radiation, which limits the energies the collider can reach. The energy loss of a highly relativistic particle per orbit is

$$-\Delta E = \frac{4\pi\alpha}{3R}\beta^3\gamma^4 \tag{4.1}$$

where R is the radius of the accelerator, α the fine structure constant, β and γ are the relativistic context variables

$$\beta = \frac{v}{c} \approx 1, \qquad \gamma = \frac{E}{mc^2} \tag{4.2}$$

in which E and m are the energy and mass of the accelerated particle.

The formula (4.1) has two important implications:

- Energy loss is inversely proportional to R hence one should increase the radius of the collider to reduce the energy loss. This is an advantage of the 27 km circumference of the LEP tunnel. Note that with increasing radius, the collider becomes more and more like a linear collider.
- Relation between the energy loss and the mass of the accelerated particle is $-\Delta E \propto m^{-4}$. Therefore, heavier the accelerated particle, much less the radiated energy. This is the reason why protons were chosen over the electrons at the LHC; because they are O(10^3) times heavier than the electrons.

The proton choice has it's disadvantages too. Unlike the electron, proton is a composite particle; it consist of a number of quarks and gluons (collectively called partons), each sharing the proton's total energy-momentum. As interactions happen between the partons, this means that only a fraction of the total CM energy is available for physics processes. The energy available to each parton is $\sqrt{x_1 x_2 s}$, where x are the fraction of the parent proton's four-momentum carried by the interacting partons, and $\sqrt{s}$ is the center of mass energy. Taking also the proton structure functions into account, it's been decided to operate LHC with 7 TeV proton beams.

In a circular collider, particle beams are held in a circular path by the Lorentz force due to magnetic field. The required magnetic field is produced by dipole type magnets. Keeping a 7 TeV proton beam in the LHC ring requires a magnetic field of 8.33 Tesla. The only cost effective way to produce a field such intense at a 27 km ring is by means of superconducting magnets. Note that in the 90's when the LHC project had started, production of such magnets was not possible, but it's been foreseen that as of 2000's, they will be available with a reasonable cost.

Because of the inverse dependence of parton-parton scattering cross section on the interaction energy ($\sigma \propto E^{-2}$) to achieve physics results in an acceptable period of time, high energy proton beams must also consist of a large number of protons. Therefore at the LHC, the increase in energy to multi-TeV scale must be accompanied by an increase in luminosity.

Luminosity $\mathcal{L}$ of an accelerator directly determines the amount of collisions happening per unit time:

$$N_{\text{event}} = \mathcal{L}\sigma_{\text{event}} \tag{4.3}$$

Here σ_{event} is the cross section of the particular process under study and $\mathcal{L}$ the machine luminosity. Luminosity depends only on the beam parameters and is written as

$$\mathcal{L} = \frac{N_b^2 n_b f_{\text{rev}} \gamma_r}{4\pi\epsilon_n\beta^*} F \tag{4.4}$$

In the above, N_b is the number of particles in one bunch, n_b the number of bunches per beam, f_{rev} the revolution frequency, γ_r the relativistic gamma factor, ϵ_n the normalized transverse beam emittance, β^* the beta function at the collision point and F the geometric luminosity reduction factor which accounts for the nonzero crossing angle at the interaction point. This expression can be rewritten in a somewhat more intuitive way as follows:

$$\mathcal{L} = \frac{f_{\text{rev}} n_1 n_2}{4\pi\sigma_x\sigma_y} \tag{4.5}$$

with n_1 and n_2 being the number of particles in colliding bunches, and σ_x and σ_y the transverse (Gaussian) beam profile parameters.

Luminosity of the LHC will be $10^{34}\,\text{cm}^{-2}\text{s}^{-1}$. This is also called the "high luminosity" configuration, because in the first few years LHC will run at a lower luminosity configuration ($2 \times 10^{33}\,\text{cm}^{-2}\text{s}^{-1}$).

In accelerators, protons are circulated and collided in bunches. A beam is similar to a train, and a bunch is like a wagon; carrying certain number of passengers (protons), having a certain spatial length and a certain spatial distance with the other bunches. We have seen on (4.4) that the number of particles in a bunch directly affects the luminosity, and as a result, they affect the number of interesting events. However, inelastic collisions happen at a variety of energy scales, a huge number of them happening at low energies. These events typically have low energy jets in the final state that make small angles with the beam axis. They are collectively called the pile-up events, since the detector sees all these final states piled up on one another, along with any interesting events if they happened during the bunch crossing too. This introduces a difficulty to the observation of interesting physics events in general.

As can be seen at (4.4) and (4.5), one way to reduce the pile-up events is operating the accelerator at a higher frequency. Major limiting factor on the frequency value is the response/recovery time of subdetector units and readout electronics.

One bunch in the LHC beam contains 10^{11} protons, and a proton beam in LHC consists of 2808 bunches. Bunch length at injection is 11.24 cm, which is squeezed to 7.55 cm at the interaction point. Bunches have a space of 7.5 cm between them. The crossing frequency has been decided to be 40 MHz, which means bunch crossings every 25 ns. In the high luminosity configuration, the inelastic pp collision cross section is $\sim$ 60 mb, which corresponds to an event rate of 6×10^8 events/s. This means that LHC experiments will observe a maximum of 20 pile-up events in each bunch crossing. The machine will be operated at 75 ns bunch crossing interval in the beginning of operation, however.

Unlike it's closest competitor Tevatron, which is a proton-antiproton collider, LHC is a proton-proton collider. The reason for not using antiprotons is the difficulty in producing the sufficient amount of antiprotons needed for LHC luminosities. On the other hand, at the LHC energies both the protons and antiprotons behave similarly in collisions because at these energies both have the gluons as the most active component. Therefore the effect of the pp choice on physics programme is minimal at best.

Unfortunately the consequences of the pp choice on the physical design of the collider itself are not as minimal. Oppositely charged particle beams can be accelerated in a single aperture ring having an elliptical cross section (e.g. Tevatron). Since the particles of the two beams are oppositely charged, they are kept on a circular path by the same magnetic field. This advantage is lost when same charged particles are collided. As the LEP tunnel has no room for two seperate rings, the LHC beam pipes have a twin-aperture design, with seperate magnetic field configuration for each beam.

Main components of the LHC ring are the dipole magnets (Fig. 4.2). They are responsible for keeping the protons on a circular track by bending their paths. There are a total of 1232

Table 4.1: LHC with numbers.

General	
Proton collision energy	$\sqrt{s}$ = 14 TeV (2.2 μJ)
Lead (Pb) nuclei collision energy	$\sqrt{s}$ = 1150 TeV
Proton bunches per orbit	2808
Protons per bunch	1.15×10^{11}
Bunch crossing interval	75 ns (initial runs), 25ns (operation)
Instantenaous power loss per proton	1.84×10^{-11} W
Synchrotron radiation power per ring	3.6×10^{-3} W
Amount of Helium in cryogenics	~ 96 tonnes
Magnets	
Dipole magnets	
Number	1232
Length	~ 14 m
Weight	~ 34 Tons
SC material	Niobium-titanium
Operating temperature	1.9 K
Energy stored/magnet	7 MJ
Operating magnetic field	0.54-8.3 T
Operating current	12 kA
Number of quadrupoles	392
Number of different magnet types	57
Total number of magnets	~ 9000

dipole magnets at the LHC. These magnets are made of superconducting Niobium-Titanium that are cooled by Helium to 1.9 K temperature. Note that this temperature is lower than that of cosmic microwave background radiation (2.73 K), hence the outer space.

Dipoles can create magnetic fields up to 8.3 T, the field needed to keep a 7 TeV proton beam in orbit, which requires an electric current of 12 kA to be conducted. This is equivalent to a stored energy of 7 MJ per dipole.

The event of a superconductor leaving the superconductivity phase is called a quench. When a superconductor running 12 kA electric current attains a nonzero resistance, the results can be catastrophic, because a power of order 10^8 W turns into heat for every ohm of resistance. That's why quench prevention is an active research topic for accelerator scientists at CERN. Beam apertures of magnets are kept in ultra-vacuum to prevent the unwanted effects of collisions between gas atoms and the beam particles.

Proton beams are accelerated by RF cavities. Each beam has 8 cavities that accelerate them

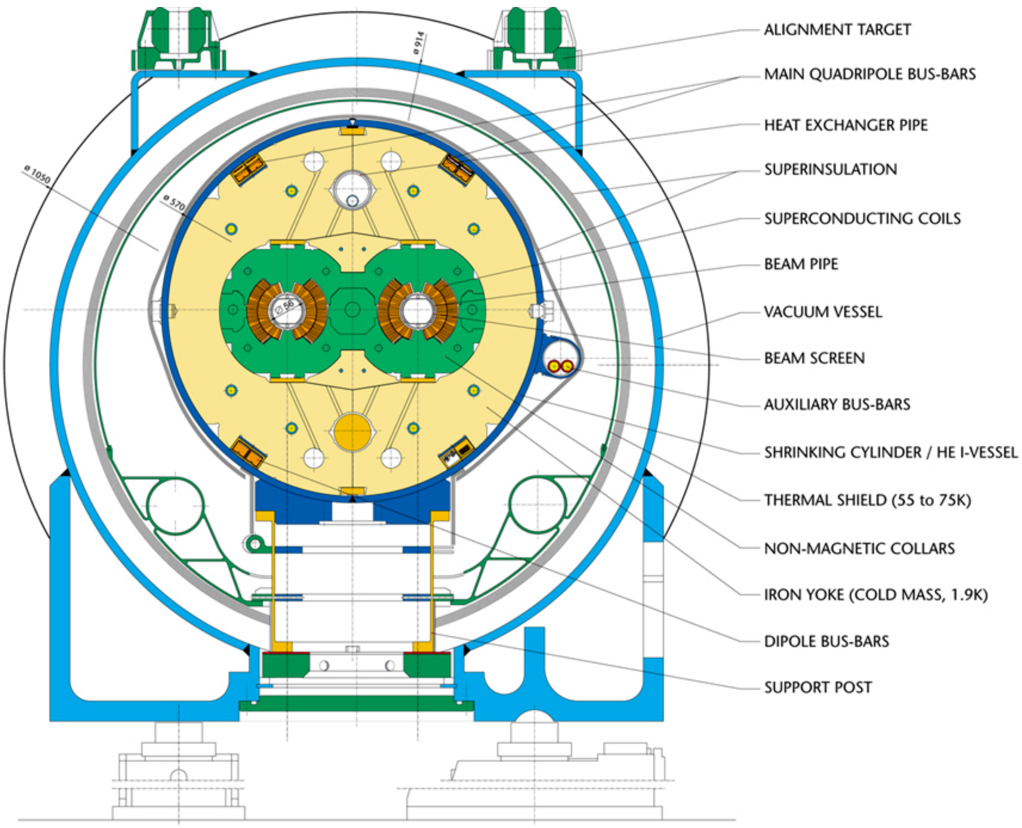

Figure 4.2: Cross-section of an LHC dipole magnet [40].

seperately. LHC cavities can create an electric field strength of ~ 5.5 MV/m at peak energy.

Concerning the acceleration of protons and heavy ions to multi-TeV energies, LHC is the last step in a chain of accelerators. Protons are obtained by ionizing Hydrogen atoms, lead nuclei are obtained from vaporized lead. Respectively, the protons go through the following accelerators[1] (see Fig. 4.3): LINAC2 (50 MeV), the booster (1.4 GeV), the PS (28 GeV), the SPS (450 GeV) and finally the LHC (7 TeV). The accelerator chain that lead ions follow: LINAC3 (4.2 MeV/u), low energy ion ring (72 MeV/u), the SPS (177 GeV/u) and LHC (2.76 TeV/u).

The resultant 7 TeV proton beam in the LHC corresponds to a stored energy of 362 MJ per beam, and an electric current of ~ 0.6 A. Transverse beam profile is O(mm), while at the interaction point it's squeezed to ~ 10 microns.

LHC has four interaction points where proton and Pb^+ beams collide. Four major experiments are situated at these locations. Two of them are general purpose detectors, "Compact

[1] Values in parantheses are the energies of particles as they leave that particular accelerator.

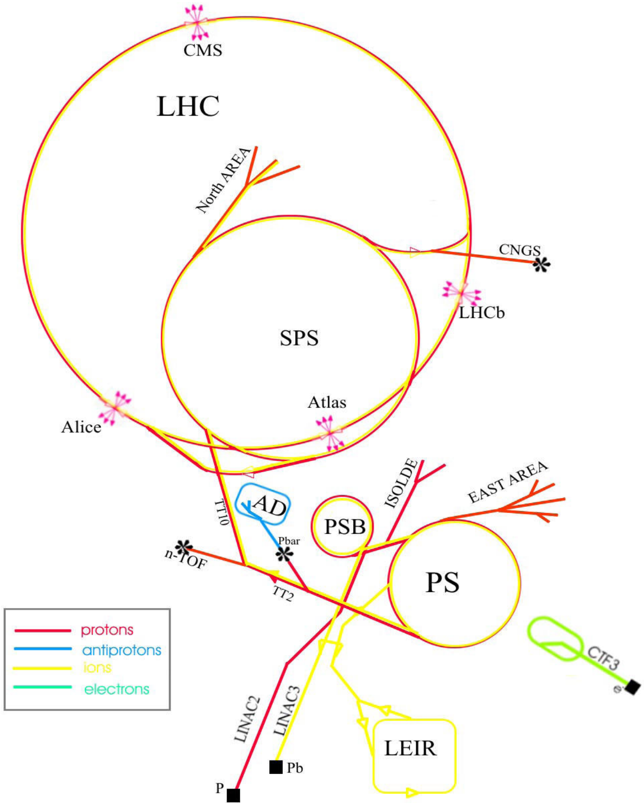

Figure 4.3: CERN accelerator complex.

Muon Solenoid" (CMS) and "A Toroidal LHC Apparatus" (ATLAS). These are designed to discover any possible BSM events, and also for precision measurements on standard model parameters. "Large Hadron Collider beauty" (LHCb) experiment specializes in b-physics, for measurements related to CP violation. "A Large Ion Collider Experiment" (ALICE) is also a specialized experiment, it's been designed for heavy ion collision and quark-gluon plasma studies.

There are two smaller detectors installed near CMS and ATLAS caverns, which are the "Total Cross Section, Elastic Scattering and Diffraction Dissociation" (TOTEM) and "LHC forward" (LHCf) experiments, respectively. Names of the experiments leave little to speak about their purpose, which is studying forward physics.

The newest LHC experiment which has been approved by CERN RB is the "Monopole and Exotics Detector At the LHC" (MoEDAL). It's an array of active detector elements installed at Point 8 cavern walls, sharing the same location with the LHCb detector. This experiment's prime motive is to search for direct magnetic monopole production at the LHC.

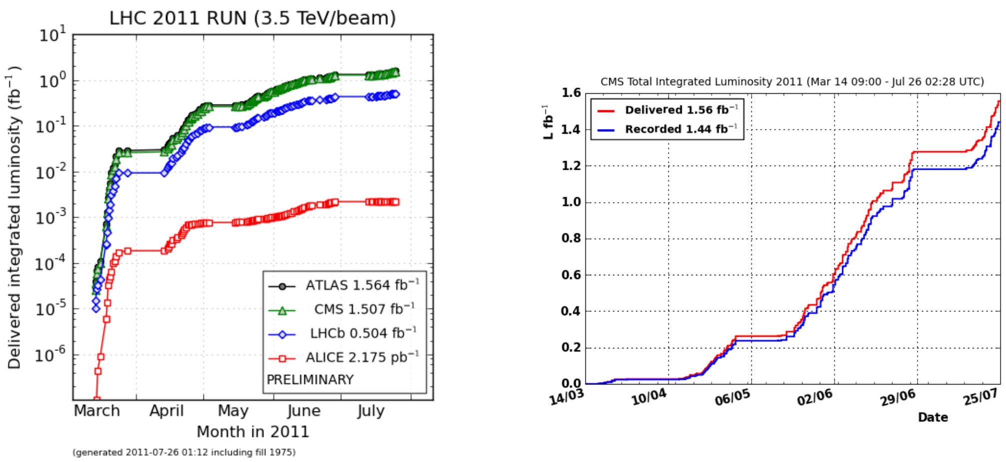

(a) (b)

Figure 4.4: Integrated luminosities of the LHC as of July, 2011. (a) Integrated luminosity as delivered to all experiments [41], and (b) the luminosity recorded by the CMS experiment [42].

4.2 The Compact Muon Solenoid

4.2.1 Overview

Compact Muon Solenoid is one of the four major experiments at the LHC. It's a general purpose detector meant to observe as many BSM processes as possible that would occur at TeV energy collisions, but to observe SM events and heavy ion collisions too. It's name emphasizes the fact that one of the primary design emphasis of CMS is precision muon measurements.

In colliding beam experiments, particles in the final state can be found to be emitted in all directions, therefore hermeticity is important for colliding beam detectors. Since construction of a spherical detector poses many technical difficulties, CMS has a cylindrical shape, collision point being located in the middle of it. As further structure, many CMS subdetectors have a barrel-endcap design.

Because of a number of reasons such as mass, lifetime, detector matter, charge and magnetic field, different particles in the final state of a high energy collision tend to leave their detectable signatures at different radial distance domains. For this reason colliding-beam detectors usually have a layered structure, like that of an onion (or maybe leek). Each layer is a different subdetector specializing in the measurement of certain type of particles or activity in general.

A general view of the CMS detector has been shown on Figure 4.5. Physics Technical Design Report [43] is a good reference for the detector and it's been widely used for the writing of this chapter. Innermost layer of the CMS is the tracker, which provides data for precise measurements of the tracks of charged particles passing through the detector.

Second layer is the electromagnetic calorimeter, i.e. the ECAL. A calorimeter in experimental particle physics is a measurement device that stops the particles reaching it, delivering physicists with measurements of deposited energy in it. Electrons and photons usually deliver all of their energies to the ECAL, yet some amount of energy leak to the HCAL is possible. ECAL also helps jet reconstruction, since jets leave a fraction of their energies in the ECAL too.

Third layer of CMS is the HCAL. HCAL is the hadron calorimeter, used for measuring the energies of hadronic activities.

The superconducting solenoid of CMS was the world's greatest as of 2008, which provides a high magnetic field of 3.8 Tesla. It houses the tracker and most of the calorimetry.

Fourth and the last physical layer of CMS is the muon system. These detectors are essentially trackers, they detect the passage of charged particles.

4.2.2 Conventions and Coordinates

The nominal interaction point in the heart of the detector is the origin of the Cartesian coordinate system. x direction is horizontal, pointing to the LHC center. y direction points vertically up from the ground plane. Hence the z direction is aligned with the beampipe, and at Point 5, it points to the Jura mountains.

The $x-y$ plane is also named the transverse plane and the azimuth angle ϕ is the angle on the transverse plane from the x direction. CMS assumes that ϕ runs in the range $[-\pi, \pi]$.

The zenith or the polar angle θ is the angle between a vector and the z (beam) direction. It shows the transversality of a vector.

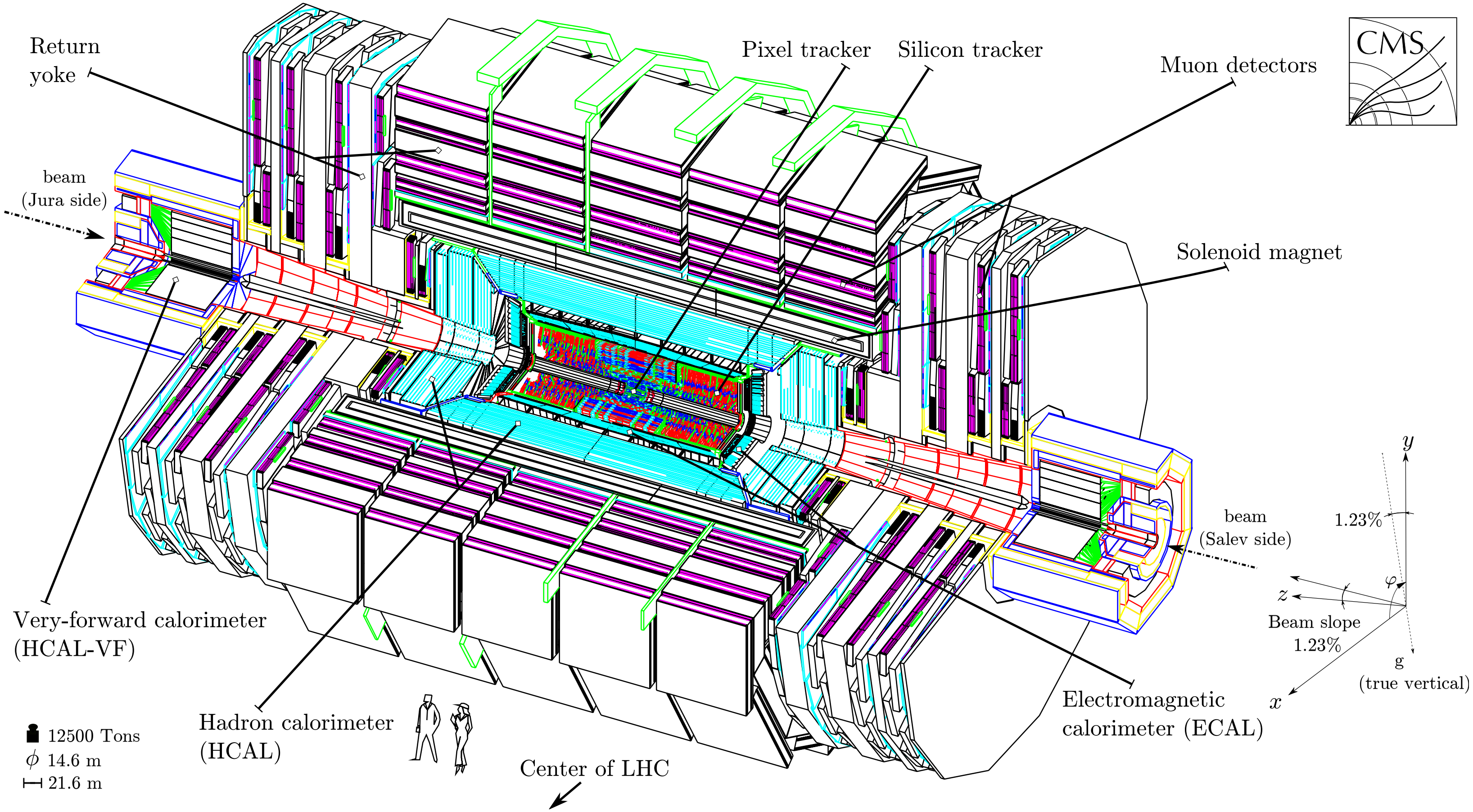

Figure 4.5: General view of The Compact Muon Solenoid (CMS) [43]

Instead of the θ angle, pseudorapidity variable (defined as $\eta \equiv -\ln\tan\frac{\theta}{2}$) is more commonly used in particle physics. A perfectly transverse vector (lying on the $x-y$ plane) has $\eta = 0$, while a longitudinal vector has $\eta = \infty$. Sign of η of a vector has the same sign with it's z component since η is an odd function about $\theta = \pi/2$.

Transverse momentum and energy of a physical object are defined as $p_T \equiv |\mathbf{p}| \sin\theta$ and $E_T \equiv E\,\frac{p_T}{|\mathbf{p}|}$. The energy imbalance in the transverse plane for a physics event is named the missing transverse energy, E_T^{miss}.

4.2.3 Detector Components

4.2.3.1 Tracker

Tracker is the innermost component of CMS, directly covering the interaction point. Tracker detects the passage of charged particles. Information acquired from the tracker is used for the following:

- Electron and muon reconstruction. Electron without a track is basically a photon from the experimental point of view. Muon track at tracker is combined with muon detectors to improve muon measurements.
- Interaction vertex reconstruction. This helps remove physical objects not part of the signal event, for example the particles coming from pile-up events.
- Determining how isolated a physics object is[2]. Isolation is an important criteria for the final state particles of signal events.
- Tracker information is indispensible for τ and b tagging.

Design of the CMS tracker has mainly been dictated by the distribution of charged particle density versus distance from the interaction point. Especially the pile-up events create a large number of low momentum particles near the interaction point. Radial distribution of the charged particle density can be split into three regions. In the high density region which is closest to the interaction point ($r < 20$ cm), pixel type detectors, at the medium and low

[2] A physics object in this context means either a jet, electron, photon or muon.

density regions ($20 < r < 120$ cm) silicon strip type detectors have been used. At the intermediate region, silicon microstrip detectors with minimum cell size of 10 cm$\times$80 μm, occupancy of approximately 2-3% per bunch crossing are used. At the outermost region ($r > 55$ cm), the particle flux is low enough for the use of larger pitch silicon microstrips with minimum cell size of 25 cm$\times$180 μm, and an occupancy of approximately 1%.

The tracker has a barrel-endcap structure. Barrel section covers the low rapidity region ($|\eta| < 2.0$), while the endcaps cover the higher rapidity region ($2.0 < |\eta| < 2.5$). Outer radius of the tracker extends to about 110 cm. It's length is about 540 cm.

Pixel detector has been shown in Figure 4.6. Pixel type detector has been chosen to provide high resolution measurements at low radial distance to interaction point (IP) under high charged particle densities. Around the outer parts of pixel detector ($r \approx 10$ cm) the charged particle flux reaches it's maximum ($\approx 10^7$/s). Occupancy here is 10^{-4} per pixel per bunch crossing. Detector has pixels having size $100 \times 150\ \mu\text{m}^2$. It's total area of 1 m^2 hosts 66 million pixels.

Pixel detector consists of three barrel layers, and two endcap layers for each side. Barrel layers are located at radii 4.4 cm, 7.3 cm and 10.2 cm. Their length is 53 cm. The endcap disks cover the radial region $6 < r < 15$ cm and at $|z| = 34.5, 46.5$ cm along the beam line. Endcap disks of the detector are assembled in a turbine-like geometry with 20° blade angle to benefit from Lorentz effect. Each blade has 7 modules, making a total of 672 pixel modules.

Note that the pixel detector itself is no larger than an amateur grade telescope. It is the smallest subdetector of CMS, yet providing more than half of the total readout channels of CMS[3] alone.

Spatial resolution of pixel tracker is measured to be about $10\,\mu m$ and $20\,\mu m$ for $r - \phi$ and z measurements, respectively.

Pixel data is acquired by Read-Out Chips (ROCs). Each ROC reads an array of 52×80 pixels, producing an analog optical signal. A single pixel barrel module is readout by 16 ROCs, and the endcap modules are read by 2 to 10 ROCs. ROC data is held in a buffer during L1 trigger decision process. An accept decision leads the data to be transmitted to Front-End Controller (FED) boards by optical fibers. A total of 40 FEDs digitize and deliver the pixel data to online

[3] which is approximately 100 million.

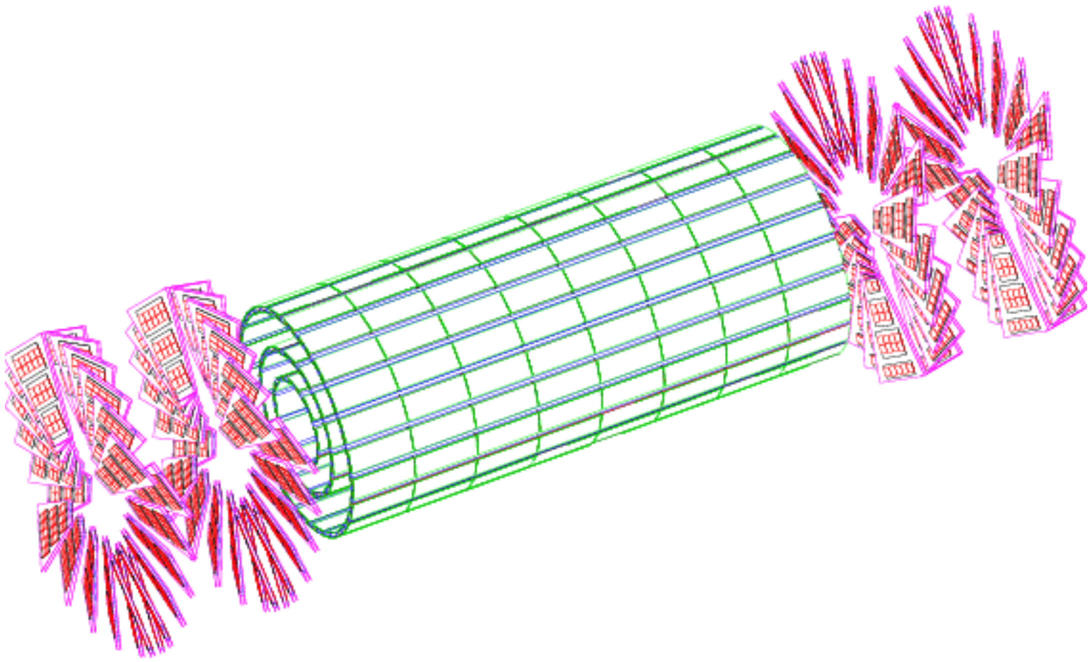

Figure 4.6: Pixel detector of the CMS [43].

data acquisition system (DAQ).

The silicon strip detector also has a barrel-endcap structure. Barrel detectors are located at r between 20 and 110 cm. They contain 9.6 million silicon strips.

Barrel detector layers are split into two concentric parts. The inner barrel (TIB) consists of 4 detector module layers, extending to $|z| < 65$ cm. First two of these layers are "stereo" modules, providing measurement in both $r - \phi$ and $r - z$ coordinates. Resultant single point resolution is $23 - 34\,\mu$m in $r - \phi$ direction and $230\,\mu$m in z direction.

The outer barrel (TOB) consists of 6 layers with $|z| < 110$ cm. The drop in the radiation at this distance allows the use of thicker silicon sensors with longer strip length and wider pitch. First two layers provide stereo measurements with single point resolution in the interval $35 - 51\,\mu$m in $r - \phi$ direction and $530\,\mu$m in z.

Endcap of strip detector (TEC) consists of 9 disks in $120 < |z| < 280$ cm in each side.

There are three small disks filling the gap between TIB and TEC, which are named as tracker inner disk (TID). Each endcap module consists of concentric rings of strip detector modules

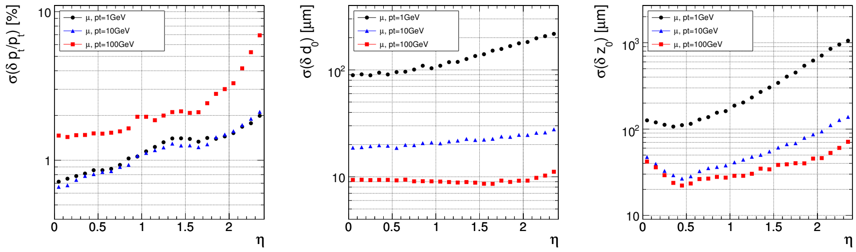

(a) (b) (c)

Figure 4.7: Performance of CMS tracker for single muon track reconstruction with P_T of 1, 10 and 100 GeV/c (a) Transverse momentum, (b) and (c) are the transverse and longtudinal impact parameters [43].

around the beam line. These strips are aligned in radial direction. The two inner rings of TID, inner two rings and the fifth ring of the TEC are again arranged as stereo modules. All sensors have the thickness of 320 μm, except four outer rings of TEC sensors, which have a thickness is 500 μm.

Strip detector has a total of 15 400 modules, which are mounted on a carbon-fiber structure. They operate at $-20\,^{\circ}$C temperature.

Strip detectors are read out by APV25 chips. Each chip samples, amplifies, buffers and processes signals from 128 channels of a silicon strip sensor. They transmit the data to FEDs via analogue optical link. These FEDs can receive the data from a maximum of 96 APV25 chip pairs. FEDs digitize, format and deliver the collected data to online DAQ for processing.

4.2.3.2 ECAL

Active elements of the electromagnetic calorimeter (ECAL) of CMS consists of 61 200 lead tungstate ($PbWO_4$) crystals in the barrel part and 7 324 in the two endcaps.

$PbWO_4$ Crystals are scintillators. They have short radiation (X_0=0.89 cm) and Molière (2.2 cm) lengths, and are also radiation hard and fast (80% of light emitted in 25 ns). Relatively low light yield (30 photons/MeV) is compensated by photodetectors with intrinsic gain. In the barrel, silicon avalanche photodiodes (APD) are used, and in the endcaps vacuum phototriodes (VPT) are used. A temperature stability within 0.1 °C is needed because of the sensitive crystals and APDs.

Barrel (EB) part has an inner radius of 129 cm. 36 identical supermodules, each covering half barrel length corresponds to $0 < |\eta| < 1.479$. Crystals have a front face cross section of $\approx 22 \times 22\,\mathrm{mm}^2$ and a length of 230 mm, corresponding to a radiation length of 25.8 X_0. These crystals point to interaction vertex with a small tilt of 3°. They are placed on a grid in $\eta - \phi$.

The endcaps (EE) are at a distance of 314 cm from the vertex and covers the pseudorapidity range $0 < |\eta| < 3.0$. They are structured as two "Dees", which are supported by 5×5 crystal modules named as supercrystals. The crystals point to the interaction vertex, but are installed on an $x - y$ grid. They are all identical with the cross section area of $28.6 \times 28.6\,\mathrm{mm}^2$, and a length of 22.0 cm (24.7 X_0).

A preshower device is placed in front of the crystal calorimeter over much of the endcap preudorapidity range. Active elements of this device are 2 planes of silicon strip detectors with a pitch of 1.9 mm, which lies behind the disks of lead absorber at depths of 2 X_0 and 3 X_0.

The readouts from photodetectors are amplified and digitized by 12 bit ADCs, which send this information to trigger. Each trigger uses the consecutive data within 250 ns time frame. These are then weighed and summed for the final value. The noise has been measured at test beam studies to be about 40 MeV per channel.

The performance of a supermodule was measured in a test beam (see Fig. 4.8). The energy resolution which is measured by fitting a Gaussian function to the reconstructed energy distributions has been parametrized as a function of energy:

$$\left(\frac{\sigma}{E}\right)^2 = \left(\frac{S}{\sqrt{E}}\right)^2 + \left(\frac{N}{E}\right)^2 + C^2 \tag{4.6}$$

where S is the stochastic term, N the noise and C the constant term. The values of these parameters can be found on Fig. 4.8.

4.2.3.3 HCAL

A hadron calorimeter with high energy resolution, good containment and hermeticity is important for a colliding beam detector. Hadron calorimeter has critical importance for especially the missing E_T measurements, which is expected to exist for a number of important BSM processes.

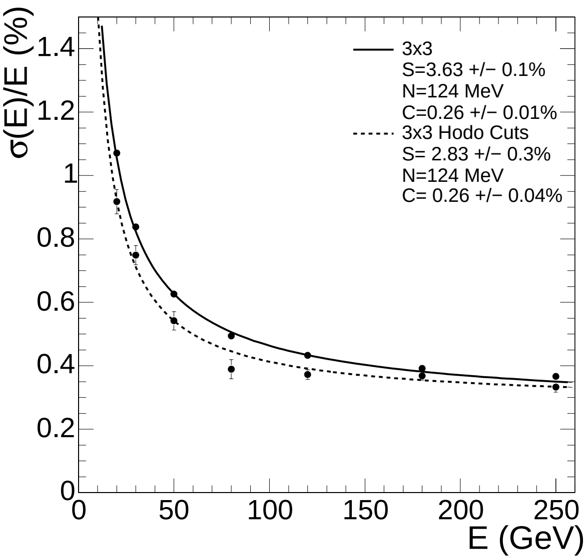

Figure 4.8: The ECAL supermodule energy resolution σ_E/E, as a function of electron energy as measured from a beam test [43]. Upper series of data corresponds to a $20\times20\,\mathrm{mm}^2$ trigger. Lower series are events to fall within $4\times4\,\mathrm{mm}^2$ region. The energy was measured in an array of 3×3 crystals with electrons impacting the central crystal.

Good containment means that as many hadronic activity as possible must be stopped in the HCAL. Structure of CMS HCAL has been determined with this requirement in mind. It is located between the ECAL and the solenoid magnet. It has also an additional layer of scintillators outside the solenoid called the hadron outer (HO) detector. Hadron calorimeter also has a barrel-endcap structure (HB and HE). There is a gap between HB and HE at 53° through which the services of ECAL and inner tracker pass.

As active elements of HCAL, the tile/fibre technology has been used. Light emerging from plastic scintillator tiles are read out with wavelength shifting (WLS) fibers. This light is channeled to readout electronics with clear fibres. Photodetection is made with hybrid photodiodes (HPDs).

Hadron Barrel (HB) subdetector consists of 32 towers in range $|\eta| < 1.4$, and a total of 2304 towers with a segmentation of $\Delta\eta \times \Delta\phi = 0.087 \times 0.087$. The HB is read out as a single longitudinal sampling. There are 15 brass plates, each with a thickness of about 5 cm, plus 2 external stainless steel plates for mechanical strength. In the front there is a 9 mm thick scintillator plate, unlike the other ones which have a thickness of 3.7 mm.

HO scintillators have a thickness of 10 mm, covering $|\eta| < 1.26$. They increase the effective thickness of the hadron calorimetry to over 10 interaction lengths, reducing the tails in the energy resolution function. HO also improves the MET resolution. The subdetector is installed on the muon barrel structure, hence it's geometry follows that of it's host. It is divided to 5 sections along η, called rings -2, -1, 0, 1 and 2. Ring 0 is fixed, and has two scintillator layers on either side of an iron absorber with thickness 18 cm, at radial distances of 3.850 m and 4.097 m. Other rings are mobile and have single layers at a radial distance of 4.097 m. Each ring covers 2.5 m in z. HO scintillators follow the HCAL barrel tower geometry in η and ϕ.

Each hadron endcap (HE) of HCAL consists of 14 η towers with 5° segmentation in ϕ, covering $1.3 < |\eta| < 3.0$. The total number of HE towers is 2304.

Coverage between the pseudorapidities of 3.0 and 5.0 is provided by the steel/quartz fibre Hadron Forward (HF) calorimeter. Because the neutral component of the hadron shower is preferentially sampled in the HF technology, this design leads to narrower and shorter hadronic showers and hence is ideally suited for the congested environment in the forward region. The front face is located at 11.2 m from the interaction point. The depth of the absorber is 1.65 m. The signal originates from Čerenkov light emitted in the quartz fibres, which is then channeled by the fibres to photomultipliers. The diameter of the quartz fibres is 0.6 mm and they are placed 5 mm apart in a square grid. There are 13 towers in η, all with a size given by $\Delta\eta$ of approximately 0.175, except for the lowest-η tower with $\Delta\eta$ of approximately 0.1 and the highest-η tower with $\Delta\eta$ of approximately 0.3. The ϕ segmentation of all towers is 10°, except for the highest-η one which has $\Delta\phi = 20°$. This leads to 900 towers and 1800 channels in the 2 HF modules.

For gauging the performance of the HCAL, it is usual to look at the jet energy resolution and the missing transverse energy resolution. The granularity of the sampling in the 3 parts of the HCAL has been chosen such that the jet energy resolution, as a function of E_T, is similar in all 3 parts. This is illustrated in Figure 4.9. The resolution of the missing transverse energy ($E_{\mathrm{T}}^{\mathrm{miss}}$) in QCD dijet events with pile-up is given by $\sigma(E_{\mathrm{T}}^{\mathrm{miss}}) \approx 1.0\sqrt{\sum E_{\mathrm{T}}}$ without energy clustering corrections, with $\langle E_{\mathrm{T}}^{\mathrm{miss}} \rangle \approx 1.25\sqrt{\sum E_{\mathrm{T}}}$

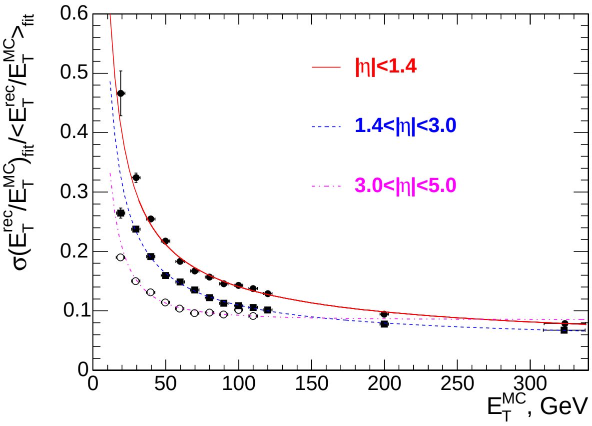

Figure 4.9: Jet energy resolution of HCAL for pions as found by simulation studies [43].

4.2.3.4 The Muon System

Outermost subdetector of the CMS is the muon system. The muon system contains about 25 000 m^2 of active surface, and around 1 million readout channels. One quarter of the CMS muon system has been shown in Figure 4.10.

Muon system has three different types of gaseous detectors. In the barrel region ($|\eta| < 1.2$) drift tube chambers have been used, because in this region the magnetic field is not strong and both the muon rate and the neutron induced backgrounds are low.

The endcap region ($|\eta| < 2.4$) has almost the opposite features of the central region; here both the magnetic field, number of muons and the neutron induced backgrounds are high. Therefore in the two endcaps cathode strip chambers (CSC) have been used.

The third detector technology used is the resistive plate chambers (RPC). These have been used in both η regions. They are operated at avalanche mode for reliable operation at high rates (up to 10 kHz/cm^2). These detectors have a fast response time and good time resolution but their spatial resolution is lower than that of CSCs and DTs. They are therefore used for bunch crossing identification.

The Muon Barrel (MB) region contains 250 gas chambers which are organized in 4 detector stations. These stations have the shape of concentric cylinders, with the iron yoke in between. Their radial distance from the beam axis are approximately 4.0, 4.9, 5.9 and 7.0 m from the beam axis, which are labeled MB1, MB2, MB3 and MB4 respectively. Each station is designed to give a muon vector, with a precision better than 100 μm in position and approximately 1 mrad in direction.

Yoke consists of five wheels along the beam line, and the detector segmentations follow this structure as well. All these wheels are divided into 12 sectors, each covering an angle of 30°. Chambers in different stations have been installed in a staggered fashion, so muons travelling through the sector boundaries would cross at least 3 of 4 stations.

Each wheel in layers MB1, MB2 and MB3 have 12 chambers. Top and bottom sectors of MB4 have two chambers so these layers have 14 chambers per wheel.

Maximum drift length of a DT is 2.0 cm and the single-point resolution is $\approx 200\ \mu$m.

Each DT chamber has either 1 or 2 RPCs coupled to it. In the stations MB1 and MB2, DT's are sandwiched between two RPC's. MB3 and MB4 DTs have single RPC attached at the innermost side of them.

As a result, a high-p_{T} muon crosses up to 6 RPCs and 4 DT chambers, producing 44 measurement points, which are then used to build a muon track candidate.

The two endcaps of the Muon Endcap (ME) system contains a total of 468 Cathode Strip Chambers (CSCs). They are grouped in 4 disks in z, and these disks have three concentric rings in the innermost station, and two in the others.

CSC's are trapezoidal in shape, consisting of 6 gas gaps. Each gap has a plane of cathode strips and a plane of anode wires, the two planes being almost perpendicular to each other. In order to avoid gaps in muon acceptance, all CSCs except the ones in the third ring of the first endcap disk (ME1/3) are overlapped in ϕ.

Each ring of a muon station has 36 chambers, except for the innermost ring of the second through the fourth disks (ME2/1, ME3/1, and ME4/1) where there are 18 chambers.

Each CSC provides up to 6 space coordinates (r, ϕ, z). The spatial resolution provided by each chamber is typically about 200 μm (100 μm for ME1/1), the angular resolution in ϕ being of order 10 mrad.

For low-momentum muons, momentum resolution is determined by the resolution of the inner tracker, because the best momentum resolution (by an order of magnitude) is made with tracker information.

For muons with P_T values up to 200 GeV/c, the momentum measurement resolution is dominated by multiple scattering in the material before the first muon station. After this value the gas chamber spatial resolution starts to dominate the precision.

Muon momentum measurement preformance of CMS has been shown in Figures 4.11(a) and 4.11(b).

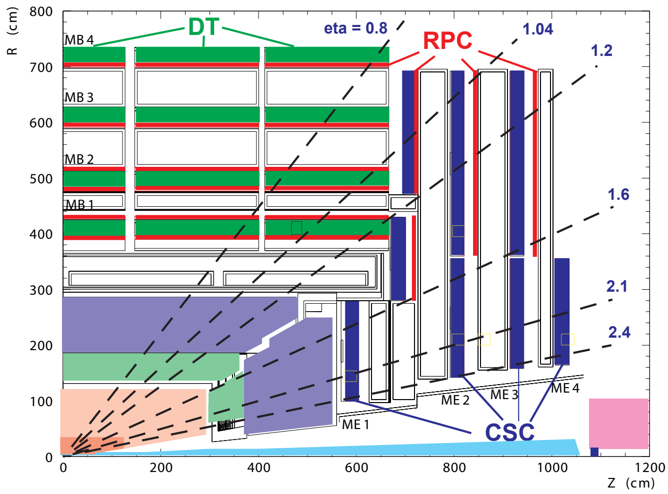

Figure 4.10: Layout of the CMS muon system [43].

4.2.3.5 Trigger and Data Acquisition

In the design luminosity of LHC, there will be bunch crossings every 25 ns, which corresponds to $\approx 10^9$ interactions per second. Only 100 events can be stored per second, which means that only one event can be picked out of 10^6 interactions, and this event cannot be picked just randomly, it must be an interesting event too.

CMS data acquisition and trigger system has 4 main parts: Detector electronics, the Level-1 trigger (calorimeter, muon, and global), the readout network, and the online high level trigger (HLT) which is based on software running on a computer farm.

The total time budget of L1 trigger is 3.2 μs, with less than 1 μs for trigger calculations, and

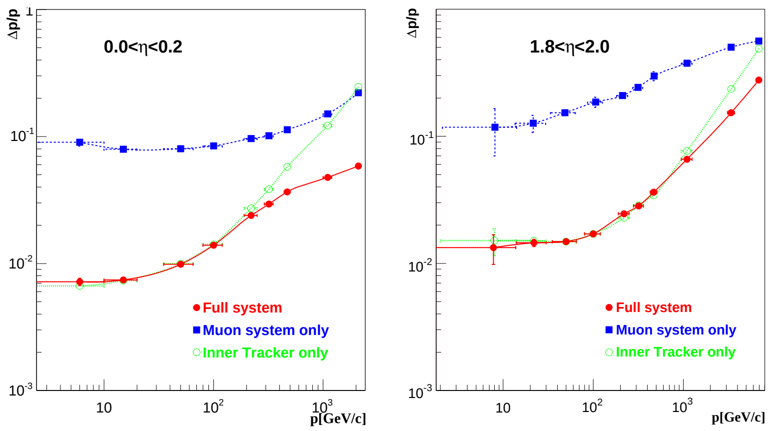

(a)

(b)

Figure 4.11: Muon momentum resolution of CMS for muons in (a) barrel and (b) endcap regions [43].

the rest for the transit time of data between the trigger and the detector. Design frequency of L1 trigger is 100 kHz.

Level-1 trigger consists of custom hardware processors. For the decision, data from calorimetry, muon systems, and some correlation of information between the two is used.

Level-1 uses “trigger primitive” objects for decision, such as photons, electrons, muons, and jets. These objects are formed from reduced-granularity and reduced-resolution data because of the strict temporal constraint. The objects are required to pass E_{T} or p_{T} thresholds. Global $E_{\mathrm{T}}^{\mathrm{miss}}$ and E_{T} sums are also used in the decision.

Trigger system consists of custom ASICs (Application Specific Integrated Circuit), FPGAs (Field Programmable Gate Array), PLDs (Programmable Logic Device), and RAM (Random Access Memory) logic chips.

While the L1 decision is being made, the high-resolution data from all detectors are held in pipelined memories, and upon receipt of a trigger, they are transferred to front-end readout buffers, in which they are further processed for e.g. data compression or zero suppression. Data is moved to dual-port memories, and claimed by DAQ system afterwards.

At this stage, each event has a size of about 1.5 MB (pp interactions), and they are held in several hundred front-end readout buffers.

Data is packed to form an event, which has the size of 1.5 MB for pp collisions, and sent to

HLT. HLT is a farm of CPUs running the trigger software. Every event is analyzed by one processor core. HLT reduces the 100 kHz L1 rate to 100 Hz, and the triggered events are sent to mass storage. Software based triggering has a number of serious advantages, such as the ability to easily benefit from the future developments in processor technology, the software used in selection can easily be upgraded as needed, also there is a flexibility in choosing the domain of events to process. Disadvantage of this strategy is the difficulty in simulating trigger decisions.

4.2.3.6 Software and Computing

A large fraction of experimentation tasks are done by the help of microcomputers. To name a few, the detector calibration, full simulation of detector response to many different physics signals, reduction of the immense data in the form of electrical signals produced by CMS into higher order physics objects (reconstruction), filtering events for different searches, storing the data and making it accessible to the physicists for analysis, and finally the physics analyses are all made on computers by the help of software.

CMS, and all LHC experiments in general produce large amounts data. Unfortunately the infrastructure needed for the computation related tasks related to this data exceeds what CERN can and will deliver in the future. Therefore it's been decided to use a distributed approach to the computing problem. The specific technology used is the "computing grid", whose popularity is growing fast among the science community worldwide, by many disciplines. The grid structure tailored for the LHC's computing needs is called the LCG, the LHC Computing Grid. LCG has a tiered organization scheme. The data is distributed from top, to bottom, Tier-0 naturally is CERN. Tier-1 and Tier-2's are computing centres at national laboratories and universities scattered around the world. Physicists can access experimental or Monte-Carlo data at Tier-2 centers or at lower tiers.

The CMS specific software components provide many important tools and services. This software infrastructure is called CMSSW. It has Monte Carlo event generation interfaces, GEANT4 interface for simulation of these events, event reconstruction services, analysis tools, various monitoring tools and a number of other tools and libraries. It's a huge software collection consisting of a few million lines of code mainly written in C++, Fortran and Python.

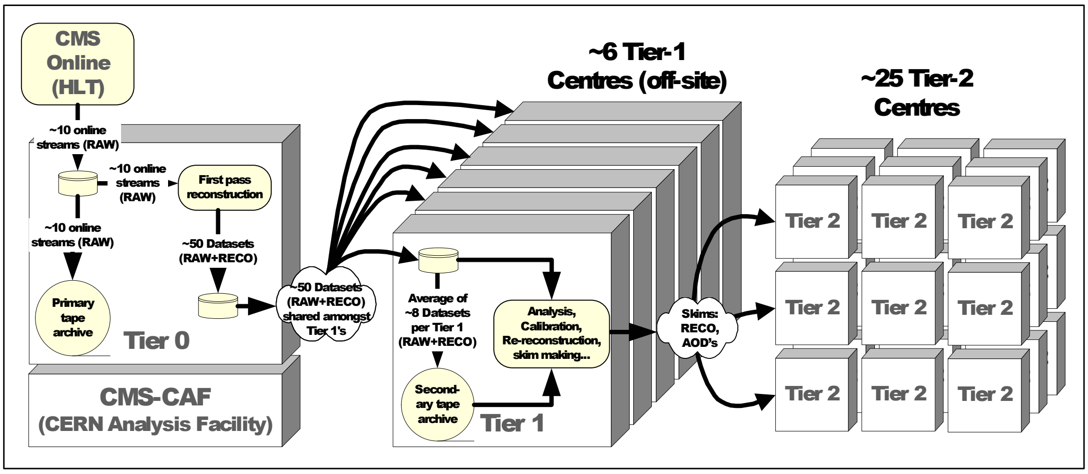

Figure 4.12: Collision data of LHC experiments is accessed from the LHC Computing Grid (LCG). Member sites of the LCG are organized in a tiered structure.

Table 4.2: Mass resolutions of the CMS detector for various particles at the low luminosity configuration of LHC.

Particle $\rightarrow$ via the decay mode	GeV/c^2
$B \rightarrow \pi + \pi$	0.031
$B \rightarrow J/\Psi + K_S^0$	0.016
$\Upsilon \rightarrow \mu^+ + \mu^-$	0.050
$H\,(130\ \mathrm{GeV}/c^2) \rightarrow \gamma + \gamma$	0.90
$H\,(130\ \mathrm{GeV}/c^2) \rightarrow Z + Z^* \rightarrow 4\mu$	1.3
$A\,(500\ \mathrm{GeV}/c^2) \rightarrow \tau + \tau$	75.0
$W \rightarrow$ jet + jet	13.0
$Z'(1\ \mathrm{TeV}/c^2) \rightarrow \mu^+ + \mu^-$	45.0
$Z'(1\ \mathrm{TeV}/c^2) \rightarrow e^+ + e^-$	5.0

CHAPTER 5

SIMULATIONS OF HIGHER DIMENSIONAL BLACK HOLES

In this chapter we will present our simulation study of quantum black hole formation and decay in the CMS experiment at 14 TeV COM energy. Our aim is to produce a black hole signal via detector simulation, try to understand it's signature for various model parameters, and develop a method to distinguish those events from SM processes with similar signatures.

5.1 A Virtual Experiment

5.1.1 Generating Black Hole Events

Black hole events have been generated with the Charybdis event generator [44, 45], version 1.003. Although later versions included additional options, this version allowed simulation of all the major features of quantum black hole physics. We used Pythia 6.325 [46] for parton showering. Both the event generation and the later simulation steps have been performed within the CMS official software framework, CMSSW [47].

Common Charybdis options used in the event generation of all datasets are defined as follows:

- *Time variation*: As the black hole evaporates, it's Hawking temperature increases with the decreasing mass. Therefore the spectrum of emitted particles changes as the black hole evaporates. This generally results in a shift in the energy spectrum of the emitted particles to higher values (Figure 5.1).
- *Greybody factors*: As discussed in the previous chapter, a particle emitted by Hawking radiation mechanism must first cross the space-time region bent by the black hole,

before reaching the observer at infinity. This region acts as a potential barrier, and it's effect on emission spectra is described by greybody factors. These factors therefore are essentially the transmission cross-sections of Hawking radiation particles. They are functions of the energy-spin of the particles and also the number of extra dimensions. They distort the energy spectra of emitted particles, also distorting the democratic decay behaviour (Figure 5.1).

- *Yoshino-Rychkov factors in cross-section*: Yoshino-Rychkov enhancement factors are enhancements to the Black-disk approximation, incorporating the inelasticity of the collision of gravitational waves corresponding to the mother partons and formation of an apparent horizon in the cross-section computation [48].

- *N-Body parameter*: Final stage of the BH decay has been simulated in Charybdis with a non-thermal n-body decay. This option sets the number of particles black hole decays to. Increased values give higher values of observed decay products in the event with a corresponding shift to lower values for their energy distribution (Figure 5.2).

- *Allow heavy particle emission*: Option to control emission of heavy particles (t, W, Z and standard model Higgs)

- *Planck mass definition*: Option to address the different conventions in literature for relating Newton constant to Planck mass. Conversion factors can be found on Table 5.8.

Option values used in this study can be found on Table 5.1.

Table 5.1: Common Charybdis options used for the generation of all datasets.

Option	Value
Time variation	On
Greybody factors	On
Yoshino-Rychkov factors in cross-section	On
NBODY	2
Allow heavy particle emission	On
Planck mass definition	2

Next step in our virtual experiment is the simulation of these physics events happening in the CMS detector at LHC, and trying to understand the response of the detector to such events.

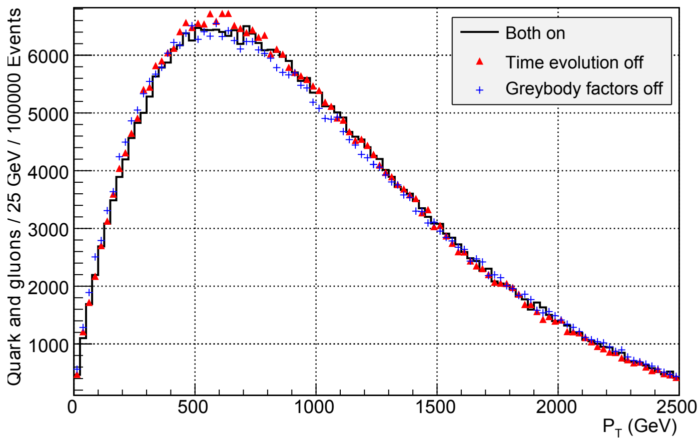

Figure 5.1: P_T distributions of quarks and gluons showing the affect of various combinations of time variation and greybody factor options for 5 TeV black holes.

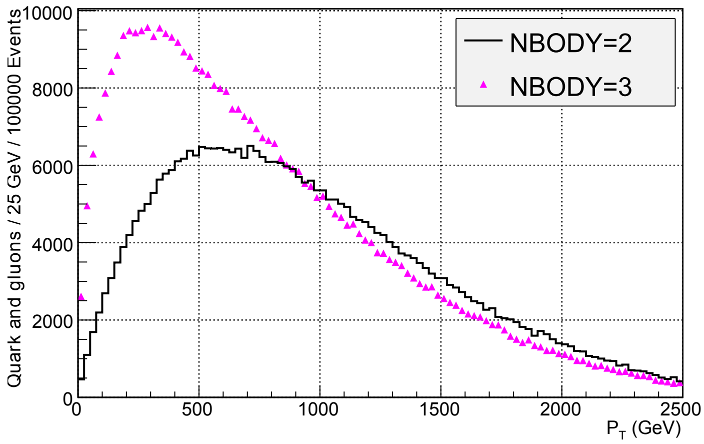

Figure 5.2: P_T distributions of quarks and gluons emitted from 5 TeV black hole decay for NBODY=2 and NBODY=3 cases.

5.1.2 Simulating Black Hole Events

For the detector simulation of the generated events, we used the fast simulation software of CMSSW [49].

Fast simulation is a method used for accurately simulating detector effects for use in physics analyses, to scan parameter space, also for purposes like developing and tuning reconstruction algorithms and designing detector upgrades. With fast simulation, events can be simulated at about 3 orders of magnitude smaller time scales compared to full simulation, which is it's main advantage. This performance is achieved by a number of simplifying assumptions, a

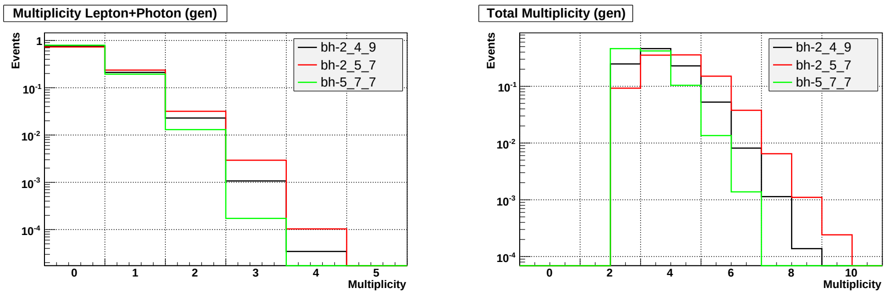

(a) (b)

Figure 5.3: (a) Generator level multiplicity for emitted prompt leptons and photons, and (b) Generator level total multiplicity.

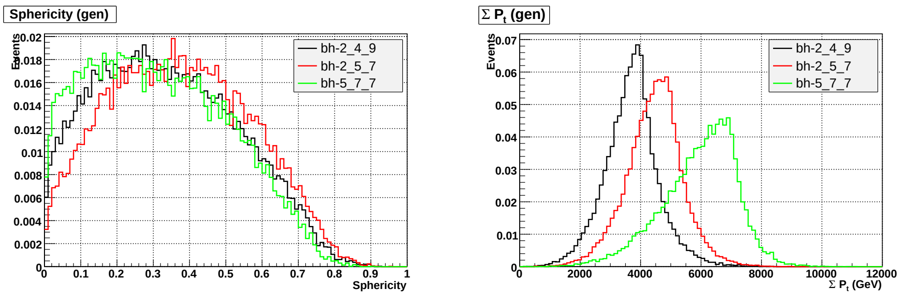

(a) (b)

Figure 5.4: (a) Sphericity distributions, and (b) $\sum P_T$ distributions for black hole events in the generator level.

number of dedicated parametrizations, and some optimized reconstruction algorithms developed for fast simulation. The following interactions are simulated by the fast simulation software of CMSSW:

- Electron bremsstrahlung,
- photon conversion,
- ionization losses,
- multiple scattering,
- electromagnetic and hadronic showering.

We studied three signal samples with different Planck mass, minimum black hole mass and total number of dimensions (Table 5.2). While simulating our samples, we assumed pile-up free collisions.

Table 5.2: Signal samples used in this analysis. Each sample contains 29000 simulated events.

M_{Pl} (TeV)	Min. BH Mass (TeV)	Tot. Dim.	Cross-section (pb)	Technical Name
2	4	9	54.05	bh-2_4_9
2	5	7	11.90	bh-2_5_7
5	7	7	$(49.90) \times 10^{-3}$	bh-5_7_7

We also simulated a sample with Geant 4 [50] based full simulation to estimate the accuracy of the fast simulation. The sample has been simulated for 5 TeV black holes and had 11 000 events. As example, shape comparisons for jet E_T and η, and for the event shape variable aplanarity have been shown on Figs. 5.5(a)-5.6. We observe that the distributions have a well agreement and conclude that fast-simulation is capable of simulating black hole events with acceptable accuracy for a physics analysis.

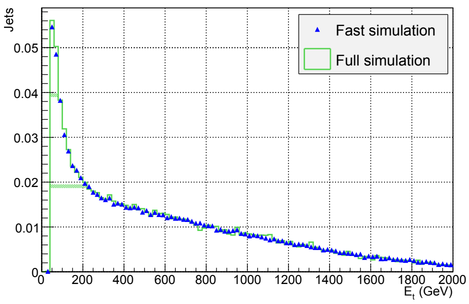

(a)

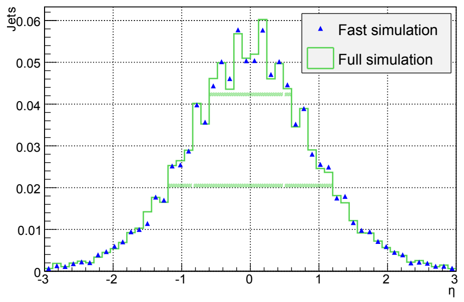

(b)

Figure 5.5: Comparison of reconstructed jets between fast and full simulation for (a) E_T values, and (b) η values.

5.1.3 Physics Objects and Preselection

The transverse plane being favored by particles radiated from the black hole allows us to select reconstructed particles with relatively high transverse momenta. This also has the advantage of rejecting backgrounds like low-$\hat{P}_T$ standard model processes and pile-up.

For the particle ID process, we used the tools provided by CMSSW, the physics analysis toolkit (PAT). PAT provides isolation information for relevant reconstructed physics objects. The isolation variable ("IsoVar") of a physics object is the sum of P_T or E_T of relevant reconstructed objects in the corresponding subdetector, found in a cone of radius ΔR around

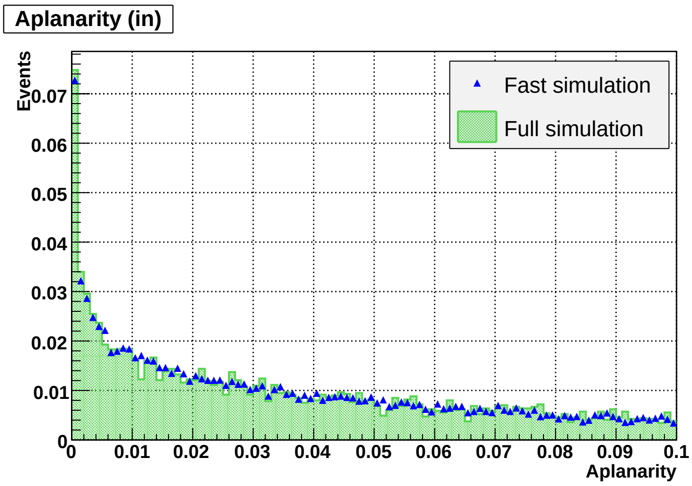

Figure 5.6: Aplanarity variable comparison among fast and full simulation samples.

it. Unless otherwise stated, we used the PAT defaults for the isolation variable calculation settings.

Jet reconstruction The jets we use in this analysis have been reconstructed with the iterative cone algorithm of cone size 0.5. Jets satisfying the following criteria have been accepted for analysis:

- Jets should satisfy $E_T > 75$ GeV and $|\eta| < 3.0$

Beam halo muons, hot/dead calorimeter cells and noise effects on both ECAL and HCAL result in fake reconstructed jets. In order to reject such jets we required the jets satisfy the following data cleaning cuts:

- EMF > 0.1, where EMF is the fraction of the jet energy deposited in the ECAL.
- Number of calorimeter towers ≥ 3
- Number of tracks in the jet cone ≥ 1

Finally we employed the Monte-Carlo jet calibration [51] (see Fig. 5.7) to correct for the jets' four momenta. The calibration is a result of simulation of the detector response for benchmark hadronic channels and analysis of monte-carlo truth and reconstructed jet correlations.

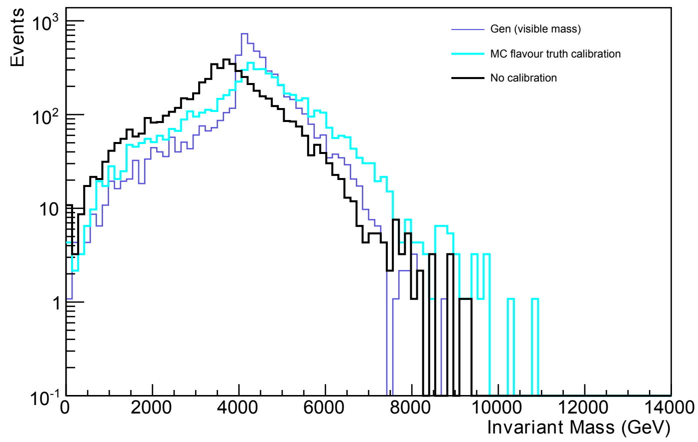

Figure 5.7: Affect of Monte-Carlo jet correction to black hole invariant mass reconstruction. Visible invariant mass is the black hole mass computed from all decay products except neutrinos.

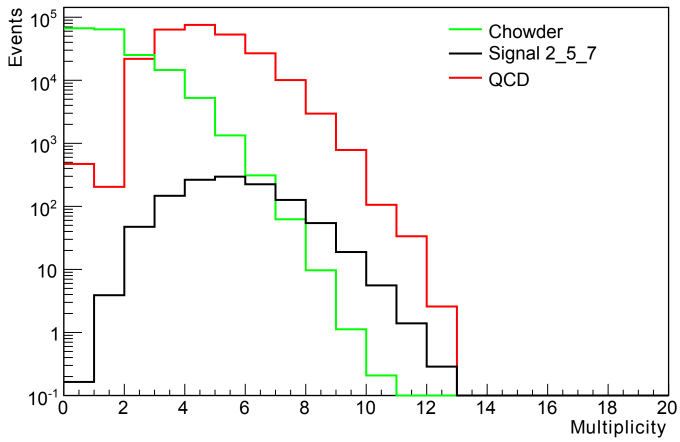

Figure 5.8: Multiplicity of jets in signal and background events.

Electron reconstruction Electrons are reconstructed using both the information from the tracker, and the ECAL. An electron consists of a supercluster in ECAL and a matching track fitted to tracker hits with the GSF (Gaussian sum filter) algorithm. This algorithm can handle the electron's bremstrahlung along it's trajectory. Electron energy and momentum is computed by combining the energy-momentum information from the supercluster object and the GSF track.

We used the following criteria to identify electrons emitted by the black hole:

- Electrons should satisfy $E_T > 75$ GeV and $|\eta| < 2.4$

- Duplicate electron removal. Duplicate electrons are two electrons reconstructed from two tracks sharing the same supercluster, or vice versa. This algorithm removed 0.3-0.4% of the reconstructed electrons in the signal samples.

- Tracker isolation: Isolation requirement is to reject the π/K meson decays faking electrons. Jets may also fake electrons because of the energy they leave in ECAL and also the possibility to emit e/μ during showering.

  Isolation variable is defined as the P_T sum of tracker tracks in a cone of $0.02 < \Delta R < 0.2$ around the electron (inner cone is for self track removal), having $P_T > 1.5$ GeV and $\Delta Z_{\text{Track,Vertex}} < 0.1$ cm. We require isolation variable to be less than 3 GeV.

- Electron quality cuts, provided by the software framework. This is one of the various criteria sets defined by the CMS e/gamma physics object group. The following variables are considered for the electron acceptance:

  - H/E: ("HoE") Ratio of the electron's energy deposited in the HCAL to the amount in ECAL.
  - $\sigma_{\eta\eta}$: This is a variable describing the spatial shape of the EM shower along η.
  - $\Delta\eta_{in}$ and $\Delta\phi_{in}$: Distance between the associated track and supercluster of the electron in η and ϕ spaces, respectively.

  Cut points are different for barrel and endcap regions of ECAL, and can be found on Table 5.3. An electron must satisfy all the cuts to be accepted.

Table 5.3: Electron ID cuts for the "Robust" preset.

	ECAL Barrel ($0 < \eta < 1.48$)	ECAL Endcap ($1.48 < \eta < 3$)
$H/E <$	0.115	0.150
$\sigma_{\eta\eta} <$	0.0140	0.0275
$\Delta\phi_{in} <$	0.053	0.092
$\Delta\eta_{in} <$	0.0090	0.0105

Reconstructed electron multiplicites have been shown on Fig. 5.9.

Muon reconstruction Muon reconstruction uses both the muon detectors and the inner tracking system to achieve high precision measurements. The reconstruction uses the stan-

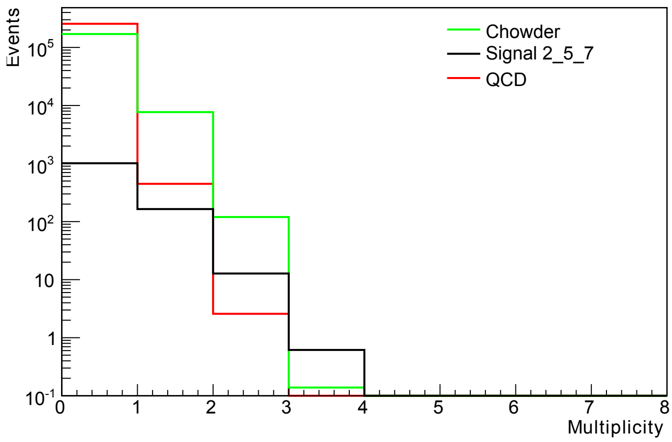

Figure 5.9: Reconstructed electron multiplicities for signal and W, Z, top background events (these backgrounds are collectively called "Chowder").

dalone muon objects which have been reconstructed with the information coming only from the muon detector system. Afterwards these muons are matched to the tracks reconstructed from the tracker system, these muons are named as global muons, which are the type of muons we used in the analysis.

- Muons should satisfy $E_T > 75$ GeV and $|\eta| < 2.4$
- Isolation criteria: We require the muons to be isolated because hadronic activity like meson decays also lead to muon emissions. Black hole decays have a lot of hadronic activity so muon isolation is important for our analysis.
  - Tracker isolation: Isolation variable is computed from the sum of P_T of all the tracks within $0.01 < \Delta R < 0.3$ distance, with minimum z distance to the primary vertex < 0.2 cm, and < 0.1 cm in the transverse plane. We require that the isolation variable has a value less than 2.0 GeV.
  - ECAL and HCAL isolation: These variables are the E_T sums of deposited energies in corresponding detectors in a cone of $\Delta R < 0.3$ around the muon track. We require the isolation variable to be less than 2.0 GeV for both ECAL and HCAL.

Reconstructed muon multiplicities for signal and background events have been shown on Fig. 5.10.

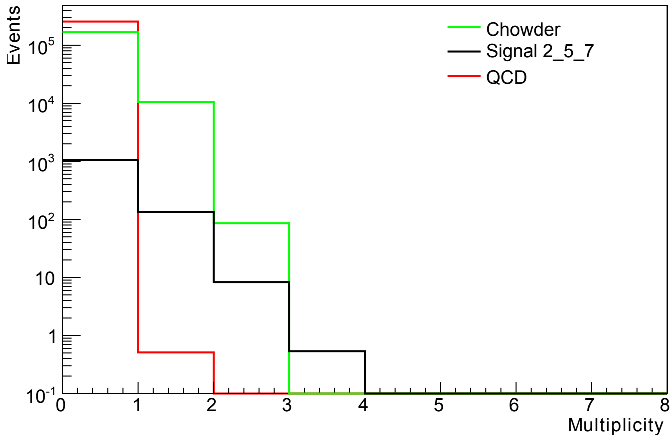

Figure 5.10: Reconstructed muon multiplicities for black hole signal and W, Z, top background events.

Photon reconstruction

- Photons are required to satisfy $E_T > 75$ GeV and $|\eta| < 2.4$
- Duplicate removal with electrons which share the same supercluster. This selection drops ~1% of all the reconstructed photons in the signal samples.
- Isolation: Meson decays (e.g. pions) are big source of photons that are not a direct part of the signal event. Energetic photons are also emitted as bremsstrahlung e.g. by hard muons. To reject such objects, we require the photons to be isolated.
  - Tracker isolation: Isolation variable is defined exactly the same way as that of electron, except for the inner cone veto. For the photon case the isolation requirement is IsoVar < 5.0 GeV.
  - ECAL Isolation: Isolation variable has been defined as the E_T sum of the basic clusters in a cone of $\Delta R = 0.3$ around the photon, excluding the ones in the photon supercluster. We require this variable to be less than 5.0 GeV.
  - HCAL Isolation: Isolation variable is the E_T sum of calo-towers satisfying the requirement $0.15 < \Delta R < 0.3$. We require the variable is < 3.0 GeV.

Before we start discussing about the characteristics of a black hole event we would like to give some information about the background processes. These are standard model processes that have a final state similar to that of a black hole decay.

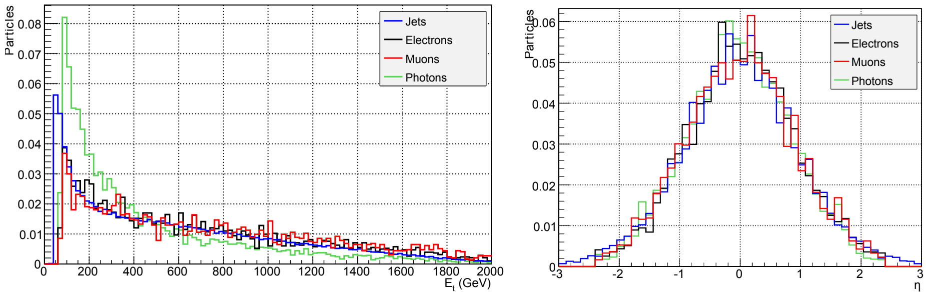

(a) (b)

Figure 5.11: (a) E_T/P_T, and (b) η distributions of reconstructed and identified particles for 4 TeV black holes.

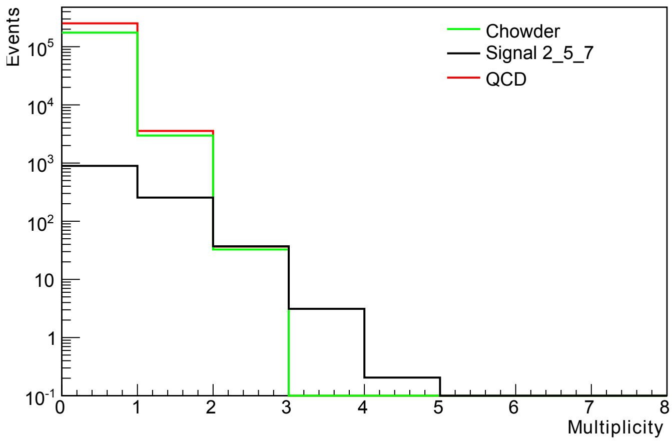

Figure 5.12: Reconstructed and identified photon multiplicities for black hole signal and W, Z, top backgrounds.

5.1.4 Standard Model Background Processes

Since the black hole decay is characterized by large transverse energies, high level of hadronic activity and lepton/photon emissions, SM events with such final states constitute the backgrounds of our signal. The background processes for the black hole events are QCD dijet/multijet, W/Z+jets and tt+jets processes.

All the background samples used in this analysis have been generated using the ALPGEN event generator [52–54]. These events have been simulated by the CMS collaboration using GEANT4 based full simulation.

Among the samples, W/Z+jets and tt+jets processes had been made available for analysis in the form of combined, or mixed sets, mimicking the actual backgrounds in the experiment.

The number of simulated events and weight breakdown for the contained sub-datasets of the mentioned datasets can be found on Table 5.4. We used the JetMET primary dataset for Chowder backgrounds. This dataset is a subset of the original dataset containing events that satisfy certain criteria such as high E_T jets in the event.

Details of QCD backgrounds analyzed can be found on Table 5.5.

Table 5.4: Sub-dataset breakdown of the “Chowder” dataset

Dataset	Cross-section (pb)	Simulated events	Jet/MET PD sel. eff. (%)	Corresponding i. lumi. (pb^{-1})
W + 0 jet,	45000	25120	0.3	0.20
W + 1 jet, $0 < P_T^W < 100$	9200	343661	3.8	0.99
W + 1 jet, $100 < P_T^W < 300$	250	169865	68.8	0.99
W + 2 jets, $0 < P_T^W < 100$	2500	159475	6.7	0.95
W + 2 jets, $100 < P_T^W < 300$	225	186726	65.0	1.28
W + 3 jets, $0 < P_T^W < 100$	590	40173	11.4	0.60
W + 3 jets, $100 < P_T^W < 300$	100	79287	67.4	1.18
W + 4 jets, $0 < P_T^W < 100$	125	23732	18.9	1.01
W + 4 jets, $100 < P_T^W < 300$	40	26942	67.8	0.99
W + 5 jets, $0 < P_T^W < 100$	85	18516	29.8	0.73
W + 5 jets, $100 < P_T^W < 300$	40	32885	75.0	1.10
Z + 0 jets	4400	75038	2.3	0.74
Z + 1 jet, $0 < P_T^Z < 100$	935	35052	3.7	1.01
Z + 1 jet, $100 < P_T^Z < 300$	30	19621	54.3	1.20
Z + 2 jets, $0 < P_T^Z < 100$	271	16991	5.9	1.07
Z + 2 jets, $100 < P_T^Z < 300$	28	20226	57.3	1.26
Z + 3 jets, $0 < P_T^Z < 100$	68	8017	11.0	1.08
Z + 3 jets, $100 < P_T^Z < 300$	13	15866	65.2	1.87
Z + 4 jets, $0 < P_T^Z < 100$	14	6377	19.3	2.36
Z + 4 jets, $100 < P_T^Z < 300$	4.3	4940	74.7	1.54
Z + 5 jets, $0 < P_T^Z < 100$	8.8	3835	31.6	1.38
Z + 5 jets, $100 < P_T^Z < 300$	4.9	4773	80.0	1.22
tt + 0 jets	619	521391	35.8	2.35
tt + 1 jets	176	230943	63.8	2.06
tt + 2 jets	34	71254	87.7	2.39
tt + 3 jets	6	12488	89.0	2.34
tt + 4 jets	1.5	4647	86.8	3.57

5.1.5 Black Hole Decay Characteristics

Invariant mass of the black hole is being reconstructed using the four momenta of all the reconstructed particles in the event; namely jets, electrons, muons and photons:

$$P^\mu = \sum_{\text{all particles}} p_i^\mu;\ M_{BH} = P_\mu P^\mu \tag{5.1}$$

Ratio of generated black hole mass to reconstructed mass for 4 TeV black holes has been depicted in Figure 5.13.

Table 5.5: QCD background datasets analyzed in this study. Number of jets column shows the number of jets in the final state and E_T bin column shows the interval in which the highest E_T jet in the event is allowed.

# Jets	Dataset E_T bin (GeV)	Cross-section (pb)	Simulated events	Corresponding int. luminosity (pb^{-1})
2	20-80	2.42×10^8	444244	0.002
2	80-140	9.95×10^5	105699	0.11
2	140-5600	6.64×10^4	502273	7.56
3	20-80	1.33×10^7	595014	0.04
3	80-140	1.05×10^6	533971	0.51
3	140-180	6.50×10^4	484266	7.45
3	180-5600	2.86×10^4	425902	14.89
4	20-100	1.84×10^6	625061	0.34
4	100-160	1.63×10^5	462629	2.84
4	160-200	1.91×10^4	165948	8.69
4	200-250	7.28×10^3	83846	11.52
4	250-400	3.50×10^3	36040	11.52
4	400-5600	4.38×10^2	6567	14.99
5	20-100	2.22×10^5	592460	2.67
5	100-160	4.31×10^4	493518	11.45
5	160-200	7.23×10^3	74921	10.36
5	200-250	3.36×10^3	11770	10.36
5	250-400	2.04×10^3	11770	3.50
5	400-5600	2.37×10^2	278528	136.53
6	20-100	3.20×10^4	524410	16.39
6	100-180	1.60×10^4	542763	33.92
6	180-250	3.00×10^3	225115	75.04
6	250-400	1.29×10^3	94915	73.58
6	400-5600	2.32×10^3	89899	38.75

We have seen in the previous chapter that the black hole is formed from the two partons of the two colliding protons. To form a black hole, these partons should have an impact parameter less than the Schwarzschild radius corresponding to their COM energy. The probability of the longitudinal momentum of the partons being exactly equal is zero, so the black holes to be formed at the LHC must have a longitudinal momentum when formed. We can see this result in the β ($\equiv v/c$) distribution of black holes, the values are for right after the formation and before any particle is emitted (Fig. 5.14). We observe that the black hole events tend to have lower β values compared to the backgrounds.

Black holes not being formed stationary has an important kinematical consequence: Decay products tend to be radiated to the transverse direction due to Lorentz contraction of the beam axis. This behavior leads to an important signature of black hole events, i.e. a high value of P_T sum (ST for short):

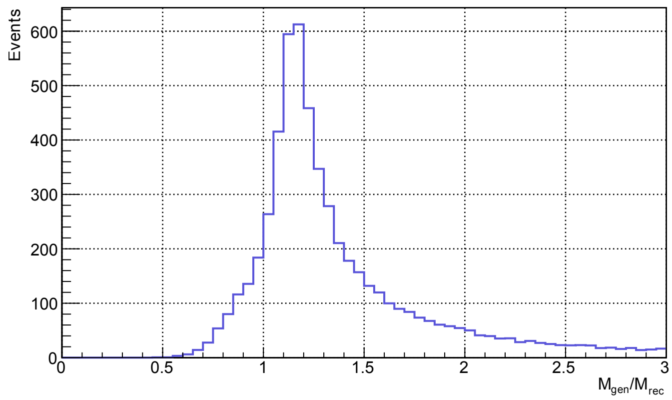

Figure 5.13: Ratio of the generated to reconstructed invariant masses for 4 TeV black holes. The shift to values higher than 1 means part of the emitted energy has evaded reconstruction, or rejected in preselection. Events with value less than one are usually the events with different type of objects (e.g. jets and electrons) reconstructed from the same energy deposit in e.g. ECAL. These are called ambiguities or reconstruction duplicates. As black hole mass reconstruction is integrative over all reconstructed particles, it's sensitive to such effects. It's possible to consider the above distribution as the starting point of a phenomenological correction to BH mass once they are discovered.

$$\mathrm{ST} \equiv \sum_{all\ particles} |\mathbf{p}_T^i| \tag{5.2}$$

The ST variable distributions have been shown on Fig. 5.15(a). We observe that this is a powerful variable for background rejection.

The momentum inbalance in the event is called the missing energy. Since we're studying parton-parton interactions, the net momentum along the beam axis is unknown, hence we are left with the inbalance in the transverse plane only. This inbalance is named MET (missing transverse energy) and is essentially the norm of the negative vector sum of all physics objects in the event. Neutrinos are the prime source of MET in SM[1]. MET distributions for 5 TeV black holes and SM background processes are shown in Fig. 5.15(b).

Sphericity tensor is helpful in understanding event-wide kinematics

$$S^{\alpha\beta} = \frac{\sum_i p_i^\alpha p_i^\beta}{\sum_i |\mathbf{p_i}|^2} \tag{5.3}$$

We construct the tensor using all the particles in the event, after that the tensor is diagonalized.

[1] Note that any activity left undetected, like energy flowing to dead regions of the detector, also contributes to MET. Therefore albeit being a very important variable for many processes, MET is one of the most demanding variable to calculate as it needs the detector to be fully understood and calibrated.

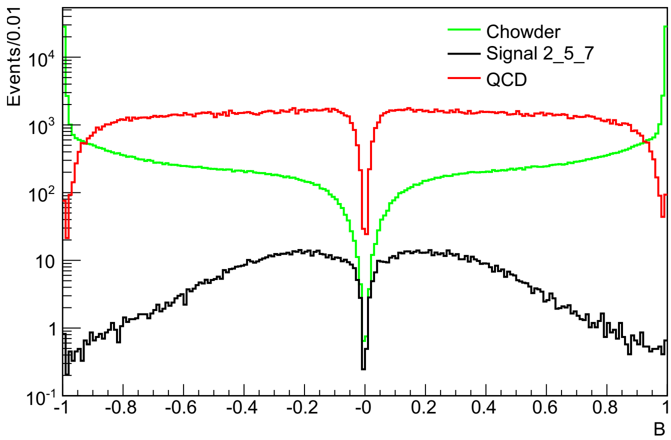

Figure 5.14: β distribution for 5 TeV black holes and SM backgrounds.

This yields three eigenvalues with $\lambda_1 \geq \lambda_2 \geq \lambda_3$ and $\lambda_1+\lambda_2+\lambda_3 = 1$. Using these eigenvalues, it is possible to write two event shape variables:

- Sphericity, defined as $S = 3/2(\lambda_2 + \lambda_3)$. This event shape variable represents how spherical the particles in the event are emitted. Increasing sphericity valus corresponds to more spherical events. Sphericity distribution for BH and background events have been shown on Fig. 5.15(c). Here we observe that BH events tend to be more spherical events.

- Aplanarity, defined as $A = \frac{3}{2}\lambda_3$. Aplanarity variable can have values in the interval $0 \leq A \leq 1/2$. Events with low A values are planar events, while high A valued events are more spherical. As seen on Fig. 5.15(d), signal and backgrounds show difference in especially the very low aplanarity values, along with a slight difference in the slope of distributions at higher aplanarity values.

E_T and η distributions of the highest E_T jet in the event are also good measures of the energy flow to the transverse plane and have discriminating value for transverse-plane-favoring events like black hole decays. Distributions of these variables have been shown on Figs. 5.15(e), 5.15(f)).

The Fox-Wolfram moments H_l, $l = 0, 1, 2, \ldots$, are defined as [55]

$$H_l = \sum_{i,j} \frac{|\mathbf{p}_i||\mathbf{p}_j|}{E^2_{\text{vis}}} P_l(\cos\theta_{i,j}) \tag{5.4}$$

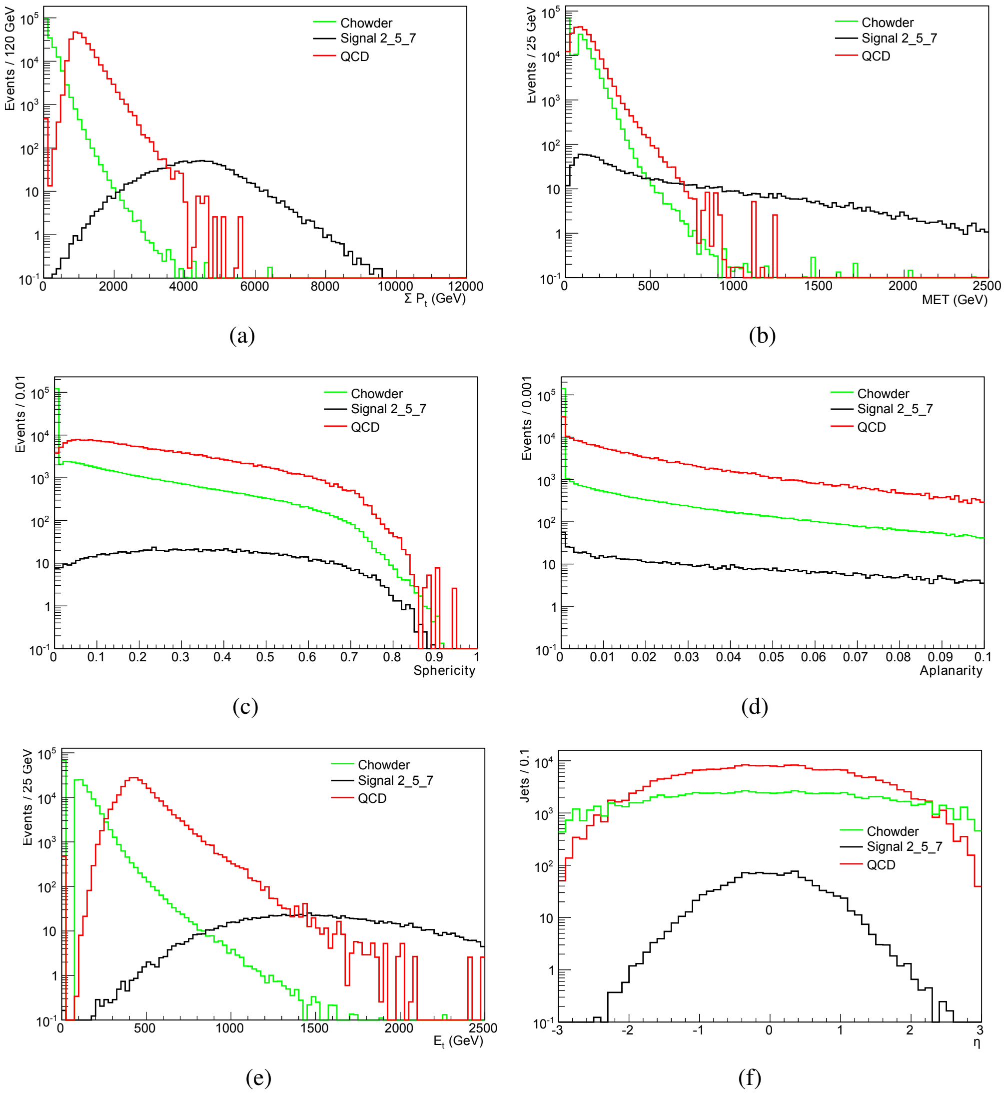

Figure 5.15: Various distributions of signal vs. background events: (a) ST, (b) MET, (c) sphericity, (d) aplanarity, (e) E_T and (f) η of the highest E_T jet in the event.

where θ_{ij} are the opening angles between particles i and j, E_{vis} the total visible energy of the event and $P_l(x)$ are the Legendre polynomials. In Fig. 5.16(a) we depict the "normalized" Fox-Wolfram moment-2 distribution, which is defined as the ratio $H_{20} \equiv H_2/H_0$.

Fig. 5.16(b) shows the Thrust distributions. Thrust is another event shape variable defined as follows [56, 57]:

$$T = \max_{|\hat{\mathbf{n}}|=1} \frac{\sum_i |\hat{\mathbf{n}} \cdot \mathbf{p}_i|}{\sum_i |\mathbf{p}_i|} \tag{5.5}$$

where $\hat{\mathbf{n}}$ is a unit vector that defines the thrust axis. Note that a back-to-back two particle event has a thrust value of 1, while a spherical event has 1/2.

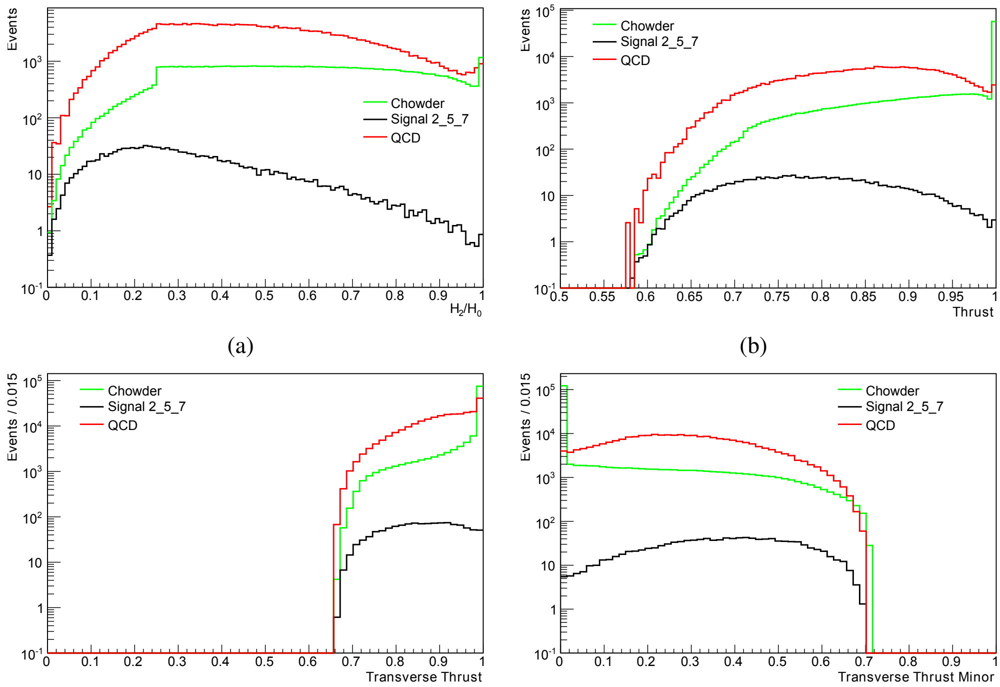

(a) (b) (c) (d)

Figure 5.16: Signal vs. background distributions of (a) the Fox-Wolfram moment H_{20}, (b) the thrust variable, (c) transverse thrust, and (d) transverse thrust minor distributions.

Transverse thrust and transverse thrust minor (Figs. 5.16(c) and 5.16(d)) are two hadronic event shape variables defined as [58]:

$$T_{\perp,C} = \max_{\hat{\mathbf{n}}_T} \frac{\sum_{i\in C} |\mathbf{P}_{\perp,i} \cdot \hat{\mathbf{n}}_T|}{\sum_{i\in C} |\mathbf{P}_{\perp,i}|}, \quad T_{m,C} = \max_{\hat{\mathbf{n}}_T} \frac{\sum_{i\in C} |\mathbf{P}_{\perp,i} \cdot (\hat{\mathbf{n}}_T \times \hat{\mathbf{n}}_{\mathrm{Beam}})|}{\sum_{i\in C} |\mathbf{P}_{\perp,i}|} \tag{5.6}$$

where $\hat{\mathbf{n}}_{\mathrm{Beam}}$ is a unit vector lying along the beam axis and $\mathbf{P}_{\perp,i}$ are the transverse momenta of the jets in the event.

α and α_T (Figs. 5.17(a) and 5.17(b)) are two other hadronic variables. They are commonly used to reject QCD dijet background as these events are characterized by two highly energetic jets.

$$\alpha \equiv \frac{E_T^{j2}}{M_{\mathrm{inv}}^{j_1 j_2}}, \ \alpha_T \equiv \frac{E_T^{j2}}{M_{\mathrm{inv},T}^{j_1 j_2}}, \tag{5.7}$$

where j_1 and j_2 are the two highest p_T jets in the event, $M_{\mathrm{inv}}^{j_1 j_2}$ is the invariant mass of the sum of their four momenta, and

$$M_{\mathrm{inv},T}^2 = m^2 + p_x^2 + p_y^2 \tag{5.8}$$

is the transverse mass. We find that these variables don't have a discriminating power for our backgrounds.

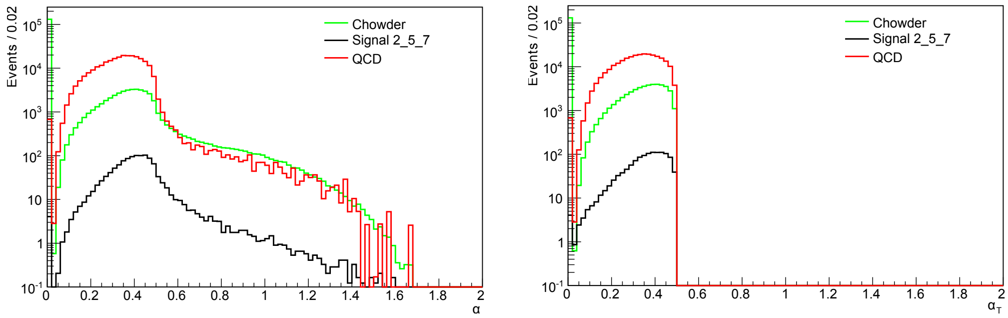

(a)

(b)

Figure 5.17: (a) α and (b) α_T variable distributions.

Hemisphere seperation is a popular method among R-parity conserving SUSY analyses. The method is useful when there are prompt particles produced (back-to-back if there are two particles) in the event, that went through a cascade decay afterwards. The method tries to split all the particles in the event to different sets as daughter particles of the initial prompt particles. We explored the possible benefits of this method for black hole signal–background discrimination.

In the current implementation of the method, we used the object pair giving maximal invariant mass to seed the seperation process, and the Lund algorithm as the association method. The angular difference distribution of hemisphere seperation is shown on Fig. 5.18(a).

Once we find the hemisphere axes and the associated particles, we calculated the thrust variable of the particles on their corresponding hemisphere axes (Fig. 5.18(b)):

$$T_{Tot} = \frac{\sum_{i_1} |\hat{\mathbf{n}}_1 \cdot \mathbf{p}_{i_1}| + \sum_{i_2} |\hat{\mathbf{n}}_2 \cdot \mathbf{p}_{i_2}|}{\sum_i |\mathbf{p}_i|} \tag{5.9}$$

where $\hat{\mathbf{n}}_1$ and $\hat{\mathbf{n}}_2$ are the two hemisphere axes, i_1 and i_2 run over hemispheres 1 and 2, while i runs over all the particles in the event.

We observe that the black holes events have lower thrust values compared to the background processes. The reason for this is black hole events being more spherical[2], which is a feature of the Hawking radiation that governs it's decay.

[2] to be more precise, elliptical, because of Lorentz contraction of the $z - axis$ due to nonzero β of the black hole

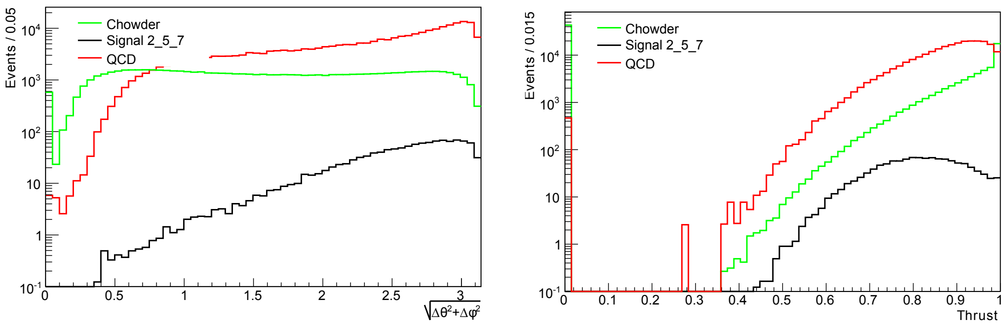

(a) (b)

Figure 5.18: (a) The angle between hemispheres as found by hemisphere seperation technique. (b) Total thrust computed on both hemisphere axes.

Unlike QCD events, black hole events are expected to have an increased b-quark activity since there are both the directly radiated b-quarks in the event, and also the ones coming from the decays of heavier particles, such as top quarks. We therefore studied the possible benefits of b-tagging algorithms to background discrimination.

For the b-tagging of jets, we used the "combinedSVJetTags" algorithm. As this study was performed, this was the most sophisticated algorithm available, that exploits all the known information about a jet, such as the impact parameter significance, the secondary vertex and jet kinematics, for identification of jets initiated by a 'b' quark. Algorithm combines these variables using a likelihood ratio technique and computes a b-tag discriminator, whose values runs in the interval 0 to 1. A high value means the jet is more likely to have an underlying b-quark. Our comparison with generator level b-quarks showed that the tagging efficiency is flat and symmetric around 0.5, we decided to tag jets having a discriminator value higher than 0.5 as b-jets. b-jet multiplicity distributions are shown on Fig. 5.19. We observe that as expected BH events have a higher occurrance of b-jets compared to the backgrounds.

Lepton emission and high event multiplicity are also important black hole decay signatures. Multiplicity distributions for signal vs. background events have been shown on Figs. 5.20(a) and 5.20(b). We observe that lepton multiplicity has a significant slope difference between signal and background. However concerning the total multiplicity, QCD processes have a similar signature with that of black hole events.

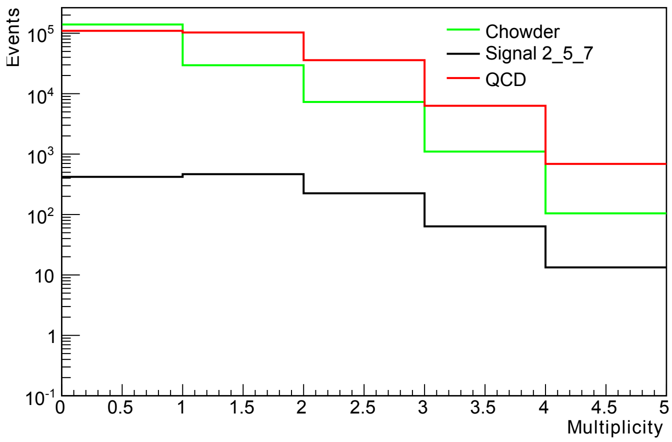

Figure 5.19: Distribution of the multiplicies of b-tagged jets for signal and background events.

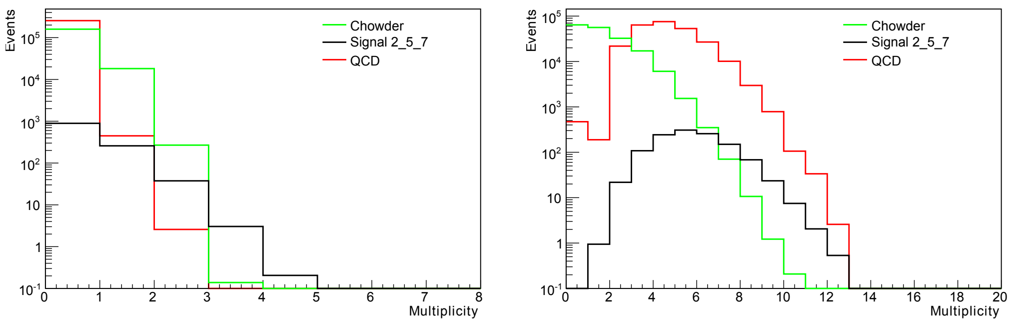

(a)

(b)

Figure 5.20: (a) Lepton, and (b) the total multiplicity distributions of signal and background events.

5.1.6 Triggering BH Events

We have tried to make a basic estimate of the possible efficiencies of an HT stream on signal and background events. Efficiency of a trigger is how efficient it accepts (triggers) interesting physics events.

As the BH events have a high level of hadronic activity, HT variable defined as the E_T sum of all the jets in the event is a convenient choice. The results that's been presented here have been found with jets that pass preselection cuts, and as we have hard E_T cuts for these objects, actual efficiencies should be higher compared to our results. In this study, we evaluated the efficiencies for the three black hole signals and two QCD background datasets. QCD dataset with low E_T has been chosen to demostrate the effect of the trigger on low HT backgrounds.

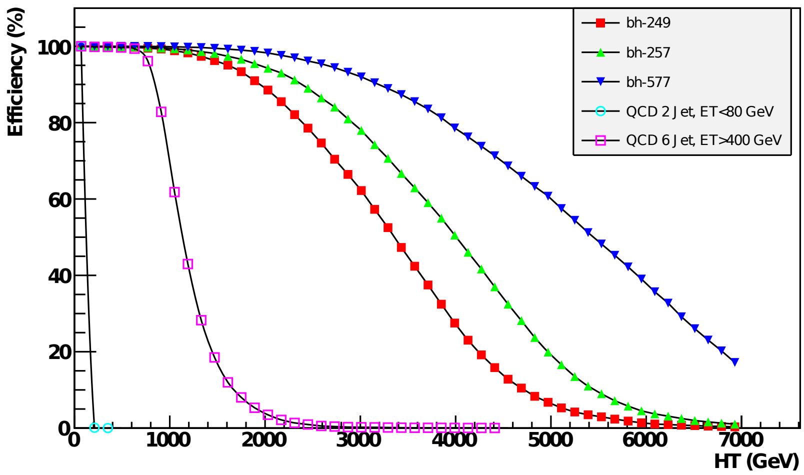

Figure 5.21: Estimated efficiencies of HT trigger for various signal and background datasets.

On the other hand, the high-E_T, 6 jet QCD processes are the ones that have the highest HT values among all of our backgrounds. These events in fact are the ones that have the most similar signatures with black hole events.

Our results have been shown on Fig. 5.21. We find that an HT trigger operating at 1 TeV has $\sim$ 99% efficiency for the signal samples and $\sim$ 70% for high E_T 6-jet QCD events. On the other hand a 1.5 TeV trigger results in an efficieny of at least 95% for the signals, and approximately 15% for 6-jet QCD events. Our conclusion is, a HT trigger operating at 1.5 TeV is a better choice which would have a fairly good efficiency for black hole events, while removing a large fraction of background events.

We would like to acknowledge Greg Landsberg and Duong Nguyen for their contributions in this study.

5.1.7 Systematic Effects

We studied a number of systematic effects that might affect our analysis results:

PDF uncertainties The black hole production cross-sections depend on the particular PDF set that's been used, and their corresponding errors. We have used the CTEQ6 PDF set [59] through the LHAPDF interface [60] to calculate the affect of these uncertainties on the black hole production cross-sections. The interface provides the central pdf values and 40 error sets. We used the modified tolerance method [61, 62] to estimate the uncertainty in the signal cross-section:

$$\Delta X^{+}_{\max} = \sqrt{\sum_{i=1}^{N}[\max(X^{+}_{i} - X_0, X^{-}_{i} - X_0, 0)]^2} \tag{5.10}$$

$$\Delta X^{-}_{\max} = \sqrt{\sum_{i=1}^{N}[\max(X_0 - X^{+}_{i}, X_0 - X^{-}_{i}, 0)]^2} \tag{5.11}$$

where X_0 is the cross-section computed with central pdf set, and X^{+}_{i} and X^{-}_{i} are the values computed with the positive and negative PDF variations. $\Delta X^{+}_{\max}$ and $\Delta X^{-}_{\max}$ are the total positive and negative variations with respect to X_0.

PDF errors are found to be asymmetric, introduce an uncertainty of about 20% into the cross-section.

Theoretical uncertainties This is the major source of uncertainties again directly affecting the production cross-sections. We computed the signal production cross-sections for 3 different Planck mass definitions and with/without the Yoshino-Rychkov correction factors. Since the different Planck mass definitions are mutually exclusive, as error we report the highest deviations.

We observe that theoretical uncertainties are the dominant source of uncertainty in our analysis results. The Yoshino-Rychkov corrections generally results in a suppression of cross-sections up to 70%. On the other hand, Planck mass definitions other than the one used in our cross-section calculations all result in higher values for cross-section. Affect on cross-sections increase with decreasing mass, predicting a one order of magnitude higher value for the lowest mass dataset.

Jet energy scale (JES) We studied the affect of a 5% uncertainty in the jet energy scale on our results by scaling up and down the four-momenta of the jets in signal events, and repeating the analysis. Difference in the number of events passing the selection cuts have been reported as an uncertainty.

We find that JES uncertainty has an effect less than $\sim$ 4% on the signal event acceptance, while it doesn't have an effect on high mass black hole events at all.

Table 5.6: Cross-sections calculated with Charybdis and corresponding PDF and theoretical errors

	bh-2_4_9 (pb)	bh-2_5_7 (pb)	bh-5_7_7 (fb)
Cross section for best fit PDF	54.05	11.90	49.96
PDF errors	$^{+8.43}_{-4.79}$	$^{+2.17}_{-1.23}$	$^{+12.30}_{-7.67}$
Yoshino-Rychkov Corrections	−35.73	−7.18	−30.13
Planck mass definition	+443.40	+40.98	+17.20
Total error in cross-section	$^{+443.48}_{-36.05}$	$^{+41.04}_{-7.28}$	$^{+21.15}_{-31.09}$

Table 5.7: Affects of a 5% uncertainty in jet energy scale on analyzed datasets.

Dataset	$\frac{\Delta\text{Events}}{\text{Events}}$ (%)	$+\frac{\Delta\text{Events}}{\text{Events}}$ (%)
bh-2_4_9	3.96	3.61
bh-2_5_7	2.02	2.02
bh-5_7_7	0	0

5.1.8 Selecting Black Hole Events

In this section we will present our event selection results for signal and background events. We will follow a cut-based method for selection. As the black hole production is a relatively high cross-section channel, discovery at the earlier stages of 14 TeV runs is possible. We have picked our selection criteria keeping in mind that simpler selection criteria are more convenient for early stages of runs. As the runs proceed and detector response to 14 TeV collisions are better understood, more sophisticated variables as discussed in Section 5.1.5 can be utilized. We will discuss our neural-network selection results, which is more convenient at later stages of the 14 TeV runs, in Section 5.1.9.

Keeping these criteria in mind, we decided that the following variables should be the most

Table 5.8: Conversion factors for Planck mass used in black hole production cross-section calculation.

Convention	Conversion
1	$M_P = (2^{n-2}\pi^{n-1})^{1/n+2} M_{Pl}$
2	$M_P = M_P$
3	$M_P = (2^{n-3}\pi^{n-1})^{1/n+2} M_{Pl}$

effective ones in start-up conditions for signal-background discrimination:

- Lepton multiplicity: We require the existence of at least one lepton (electron or muon) in the event. This cut helps reject the QCD and hadronic decaying W/Z backgrounds.
- ST: This cut is the main discriminator between the black hole signal and backgrounds since a large amount of the radiated energy from the black hole goes to the transverse plane.

The cut values of the selection variables, along with the selection results can be found on Table 5.9.

Table 5.9: Event selection results for 100 pb^{-1} integrated luminosity. Events against the cuts show the remaining events after the cut. The cut values have an average efficiency of 20% for signal events. Lepton cut happens to be very important for QCD background suppression. The ST cut point has been chosen to be efficient for all three signal points.

	bh-2_4_9	bh-2_5_7	bh-5_7_7	QCD Multijet	"Chowder"
Events (100/pb)	5405	1190	5	255700	177792
Lepton multiplicity > 0	1165	299	1	450	18449
Sum P_T > 2500 GeV	961	276	1	3	3
$S/\sqrt{S+B}$	31	16	0.38	–	–

In experimental particle physics, to be able to announce a discovery, the significance must be at least 5, and at least 10 signal events must have been observed. Our cut based selection results show that, for points in parameter space with low Planck mass, discovery criteria can be satisfied much earlier than 100/pb integrated luminosity is collected.

However this positive situation changes to negative for high Planck mass parameters. Because of low cross-section, a discovery of a parameter point in this region will take higher amount of collected data. In the next section, we will study artificial neural network selection, especially to improve the selection of such points.

5.1.9 Artificial Neural Network Selection

Artificial neural networks (ANNs) are used as a multivariate signal-background discrimination tool in experimental particle physics. It is a sophisticated, yet well understood and robust

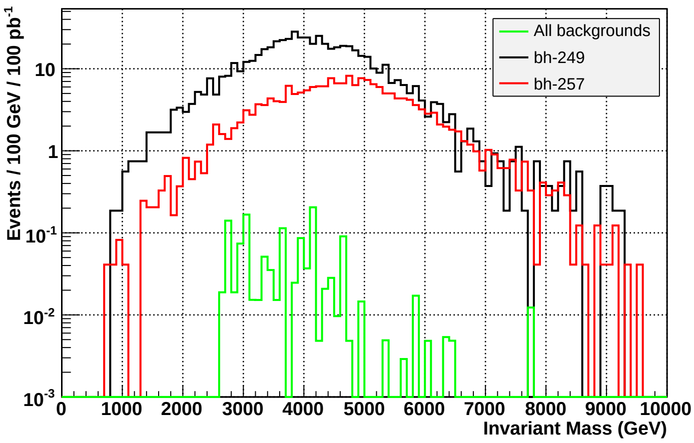

Figure 5.22: Invariant mass distributions after selection of signal and background events, for 100 pb^{-1} integrated luminosity.

method. We chose to use ANNs because it's is a powerful nonlinear method that can accept a relatively high number of variables and can handle both linear and nonlinear correlations well.

General structure of an example artificial neural network has been shown on Fig. 5.23. An ANN consists of a number of interconnected neurons organized in layers. Neurons sums their input in a predefined way, and produces an output signal. When an input is supplied to the input neurons, the network moves into a definite state, which is reflected in the response produced by the output neuron(s). Therefore, a neural network is essentially a mapping from n input variables $x_1, x_2, \ldots, x_n$, to a single, or m output variables $y_1, y_2, \ldots, y_m$.

In general, a neural network with n neurons can have a total of n^2 directional connections, however the network behavior can be better understood when the neurons are organized in layers. Neurons of each layer are only allowed to have connections with the neurons in the next layer. As the connections are directional, the first layer becomes the input layer, having one neuron per input variable. The layer from which the network response is produced is the output layer. In applications like signal-background discrimination, a single output y_{ANN} is required, so the output layer consists of a single neuron. All the other layers are called the hidden layers because they are hidden from the "outside world".

The response of the neurons is determined by the function ρ. It's assumed to be seperable

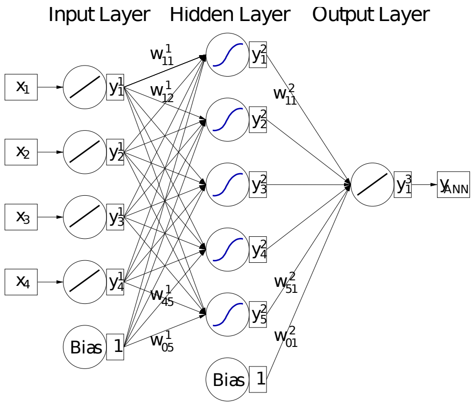

Figure 5.23: General structure of an example artificial neural network. The network above has a single hidden layer, and a single output neuron. The inputs x_i are fed to the input layer neurons linearly. Outputs y_i^1 of these neurons are transmitted to the hidden layer neurons, which are weighed with coefficients w_{ij}^1. These weights constitute the memory of the network. Each neuron in the hidden layer sums it's weighed inputs and produce a nonlinear response y_j^2. These responses are summed by the outer layer neuron and the output response y_{ANN} is produced.

to two parts, first part determining how the inputs are summed (synapse function κ), while the second determining the output with respect to this sum (the neuron activation function α). Therefore we can write $\rho = \alpha \circ \kappa$. The κ function for the j^{th} neuron of layer l may have the following forms:

$$\kappa : (y_1^l, \ldots, y_n^l | w_{0,j}^l, \ldots, w_{n,j}^l) \to \begin{cases} w_{0j}^l + \sum_{i=1}^n w_{ij}^l y_i & \text{(direct sum)}, \\ w_{0j}^l + \sum_{i=1}^n (w_{ij}^l y_i)^2 & \text{(sum of squares)}, \\ w_{0j}^l + \sum_{i=1}^n |w_{ij}^l y_i| & \text{(sum of absolutes)}, \end{cases} \tag{5.12}$$

and the possible forms of the α function are as follows:

$$\alpha : x \to \begin{cases} x & \text{(linear)}, \\ \frac{1}{1+e^{-kx}} & \text{(sigmoid)}, \\ \frac{e^x - e - x}{e^x + e^{-x}} & \text{(Tanh)}, \\ e^{-x^2/2} & \text{(radial)}, \end{cases} \tag{5.13}$$

In this study, the training of the network has been made with the BFGS algorithm [63–66]. This algorithm consists of four major steps:

1. Two vectors, D and Y are calculated. D is the vector of changes in the weights between

iteration $(k-1)$ and k, and Y is the vector of gradient errors:

$$D_i^{(k)} = w_i^{(k)} - w_i^{(k-1)}, Y_i^{(k)} = g_i^{(k)} - g_i^{(k-1)}. \tag{5.14}$$

where i is the index of synapse, g_i the gradient of the i^{th} synapse, w_i is the weight of the i^{th} synapse, and k is the iteration index.

2. Inverse of the Hessian matrix H is approximated by the following expression:

$$H^{-1(k)} = \frac{DD^T(1 + Y^T H^{-1(k-1)})Y}{Y^T D} - DY^T H + HYD^T + H^{-1(k-1)} \tag{5.15}$$

where the k^{th} iteration is implied for all the D and Y terms.

3. The D vector is estimated using the following relation:

$$D^{(k)} = -H^{-1(k)} Y^{(k)} \tag{5.16}$$

4. By applying the line search algorithm, compute a new vector of weights. In this algorithm, the error function is assumed to have a parabolic form locally. By evaluating the second derivatives, the minimum of the parabola is estimated, and the total error is evaluated at this point. To find the absolute minimum, the points along the line which is defined by the direction of the gradient in weights space are evaluated. In the next iteration, the weights at this minimum are used.

The BFGS method has the advantage of requiring smaller number of iterations compared to another popular training method, backpropagation (BP). As the computing time required per iteration is proportional to the total number of synapses, the BFGS method is not convenient for large networks (which is not the case here).

ROOT's TMVA facilities allow the decorrelation and Gaussianization transformations to be applied to the input variables before the training of the network starts. Correlations between input variables in general have a negative effect to classifier performance. The decorrelation procedure aims to transform the input variables to a new basis in which they are as uncorrelated as possible. The transformation results in completely decorrelated variables when the correlations are linear, and the variables have a Gaussian distribution. Note that in real-world problems these conditions are rarely met. Therefore first the input variables are applied the Gaussianization procedure, than they are decorrelated.

The Gaussianization transformation is performed in two steps. First, the variables are transformed into uniform distributions using their cumulative distribution functions obtained from the training data. Second, the inverse error function is used to transform these uniform distributions into the desired Gaussian shape with zero mean and a width of unity.

In summary, the transformation can be written as follows:

$$x \to x' = \sqrt{2}\,\mathrm{erf}^{-1}\left(2\int_{-\infty}^{x} \hat{x}(x')\mathrm{d}x' - 1\right) \tag{5.17}$$

where $\hat{x}$ is the probability density function associated with x.

The decorrelation transformation is a straightfoward procedure that can be summarized as follows:

1. Square-root of the covariance matrix C' is computed. TMVA finds this matrix by diagonalizing the covariance matrix C:

   $$D = S^T C S \implies \qquad C' = S\,\sqrt{D} S^T \tag{5.18}$$

   where D is the diagonal matrix, and S is symmetric. Note the C is a symmetric matrix. The square-root of a matrix C is defined as the matrix C', whose square yields the C matrix: $C = (C')^2$.

2. Decorrelation is performed by the transformation:

   $$\mathbf{x} \to \mathbf{x}' = (C')^{-1}\mathbf{x} \tag{5.19}$$

Note that both the Gaussianization and the decorrelation procedures are applied to either the signal, or background events, but not both.

Concerning the network output, a measure of "importance" of each input variable may be estimated in MLP neural networks. These values indicate how important a variable is in recognition of signal events. Importance I_i of the input variable i is calculated as follows:

$$I_i = \bar{x}_i^2 \sum_{j=1}^{n_h} \left(w_{ij}^1\right)^2, \qquad i = 1, \ldots, n_{\mathrm{var}} \tag{5.20}$$

where $\bar{x}_i^2$ is the mean of the variable x_i in the sample.

ANN's application in signal-background discrimination consists of two steps, training and selection. In the training stage, neural network is supplied both the signal and background events, and is trained to recognize the signal sample, while rejecting the backgrounds. At the selection stage, the neural network is given physics events, and is expected to provide a high efficiency discriminator for signal and backgrounds.

Table 5.10: Variables used as input to ANN and their importance rankings.

Rank	Variable	Importance
1	Jet P_T^0	40.5
2	Aplanarity	22.4
3	ST	17.3
4	Lepton multiplicity	15.6
5	Hemisphere DTheta	13.2
6	α_T	11.0
7	b-jet multiplicity	9.99
8	Alpha	7.47
9	Transverse thrust	2.87
10	Sphericity	2.64
11	Invariant mass	6.54

In this study, we used ROOT's TMVA toolkit [67], version 4.1.2. As the input variables, we used the lepton multiplicity, P_T of the highest P_T jet in the event, ST, Aplanarity, b-jet multiplicity, α, α_T, invariant mass, hemisphere $\Delta\theta$, sphericity and transverse thrust. Definitions of these variables can be found on Section 5.1.5. The importance values of the input variables have been shown on Table 5.10.

Linear correlation coefficients of our input variables for signal and background events have been shown on Fig. 5.24(a) and 5.24(b). Notable correlations can be listed as follows:

- Hemisphere $\Delta\theta$ and the invariant mass (69%),
- α_T and and the invariant mass (61%),
- Transverse thrust and sphericity (-39%),
- Sphericity and aplanarity (49%).

We observe that the linear correlation patterns in signal and background events are similar, however the correlations are in general weaker in background events. The exception to this observation is the strong correlation of α and α_T in the QCD events (83%).

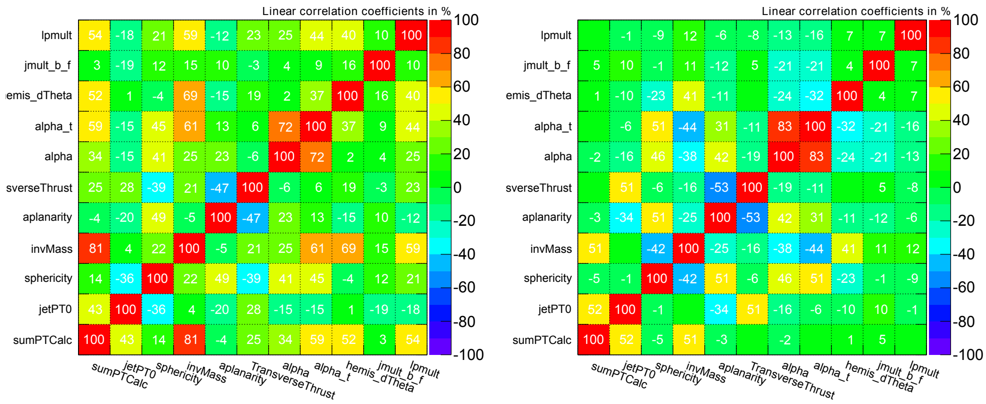

(a) (b)

Figure 5.24: Linear correlation coefficients of input variables for (a) signal events, and (b) background events.

We have studied the affect of both the number of neurons in the hidden layer, and the number of training events on the classifier performance. We used the significance values normalized to 100 pb^{-1} integrated luminosity[3] as the metric of ANN performance. We have tested a large number of neural networks with the number of neurons in the hidden layer ranging from N to $N + 25$, with N being the number of input variables. We also studied the affect of the training events, with the number of training events being 500, 1000, 2000, 3000, 4000 and 5000. In all cases we took the cut point on the ANN discriminator at 0.9 to increase the resolution of significance values. Our results have been shown on Figs. 5.25(a), 5.25(b) and 5.25(c)

All the test samples show a fluctuating significance pattern with increasing number of neurons. This is a common situation in ANNs. Fluctuations don't have a fixed period, also the correlations among different number of training event runs is minimal, therefore the only method to find the optimal value of neurons is trial-and-error.

We observe that the fluctuations decrease with increasing number of training events in general. Therefore we state that 500 and 1000 training event cases do not have enough events for the weights to be properly adjusted. On the other hand at the 2000 and 3000 training event runs we observe a decrease in fluctuation amplitudes, also giving the two highest significance values in our study, 0.65 for 2000 events and 0.64 for 3000 events. We report the former result as the optimal value in this study. Lastly, the 4000 and 5000 event runs are the flattest ones in significance. We interpret this behavior as the diminishing returns, which indicates that the

[3] we have used the significance definition $\mathcal{S} = S/\sqrt{S+B}$ throughout this study

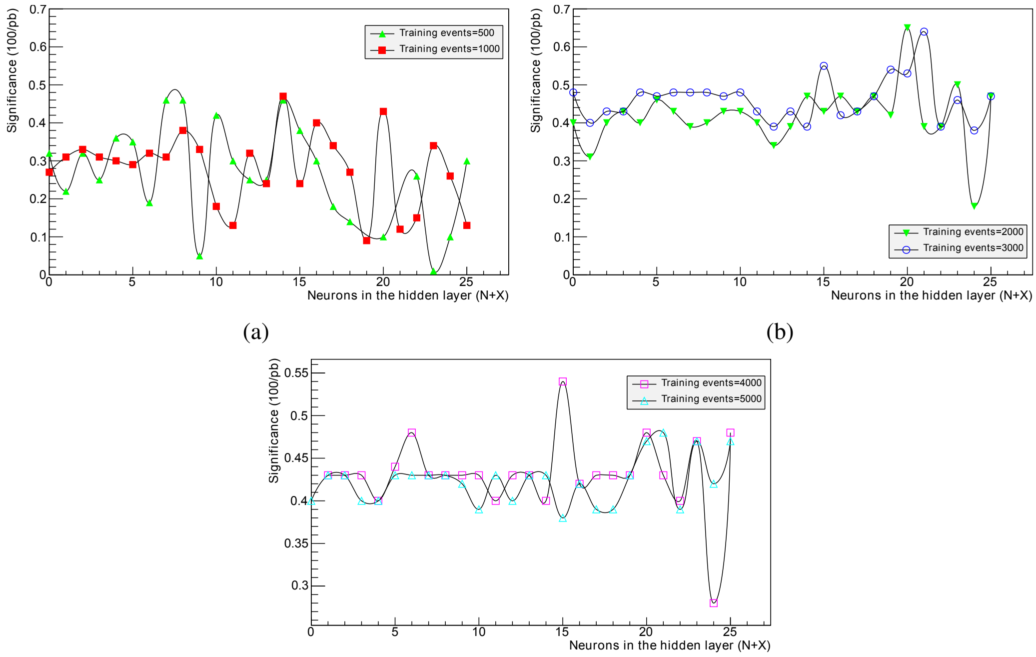

(a) (b) (c)

Figure 5.25: Dependence of significance on the number of neurons in the hidden layer $(N+X)$ for (a) 500 and 1000, (b) 2000 and 3000 and (c) 4000 and 5000 training events.

optimal value for training events has already been reached.

Once we decided the number of neurons and the number of training events, we sought for the optimal cut point on the ANN discriminator. We define this point as the point that maximizes the significance for 100 pb^{-1} integrated luminosity. Our results have been shown on Figure 5.26. At the cut point 0.985, the number of simulated background events are less than 10, which ultimately determines the precision of the cut point.

To find our final results, we run the ANN selection on all our signal and background samples. The neural network implementation in this study can be summarized as follows:

- We have a neural network with 11 input variables.
- The network has a single hidden layer which has $N + 20$ neurons (see Fig. 5.28).
- Neurons used the tanh as the response function.
- We applied a preselection cut to both signal and background events at ST> 1500 GeV to simulate the effect of the HLT.
- Network has been trained for 2000 signal and 2000 background events.

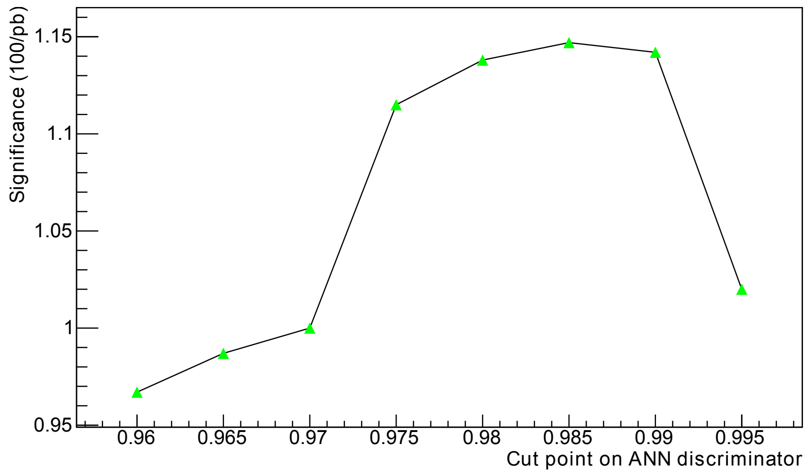

Figure 5.26: Significance values corresponding to cut points on the ANN discriminator.

- Signal events for which the network has been trained was the bh-577 dataset, while the trained background was the 6-jet QCD events with highest jet in the event having $E_T > 400$ GeV.

Dependence of signal and background efficiencies, signal purity, and the significance on ANN output has been shown on Fig. 5.27. ANN selection results can be seen on Table 5.11.

When compared with the cut based selection results (Table 5.9), we observe that ANNs are a high performance method for signal-background discrimination. For the *bh-577* dataset for which the network has been trained to recognize, the significance has increased three times. Although ANN accepts twice the amount of QCD events compared to the cut based method, it both completely rejects the other backgrounds, and also has about 4 times the efficiency for signal acceptance. What's interesting is the efficiency of ANN on the signal points it hasn't been trained for. ANN gives a slightly lower significance result for the low mass point *bh-249*, however the mid-range point *bh-257* now has a higher significance value compared to the cut-based selection.

5.2 Summary and Conclusions

Quantum black hole production at the LHC is one of the most exciting beyond the standard model processes. Such tiny black holes are predicted by both the ADD and RS type extra di-

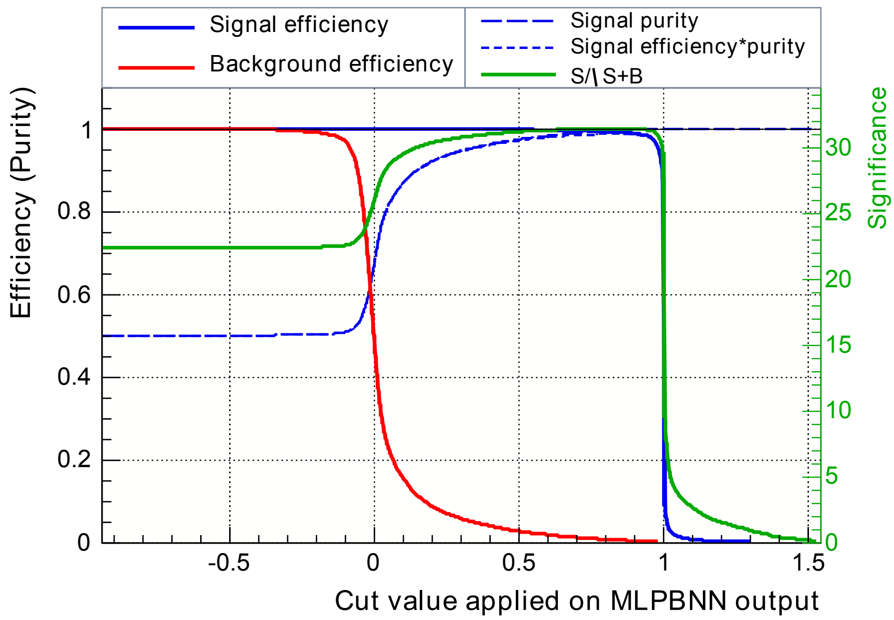

Figure 5.27: Signal vs. background efficiencies, signal purity and significance results for arbitrary integrated luminosity of MLP.

Table 5.11: Results of the ANN selection.

Cut-Dataset	2_4_9	2_5_7	5_7_7	"Chowder"	QCD Multijet
Events (100/pb)	5405	1190	5	177792	255700
MLP selection	865	381	~4	0.0	~6
(efficiency)	(%16)	(%32)	(%73)	(%0.0)	(%1.96×10^{-5})
$S/\sqrt{S+B}$	29	19	1.15	-	-

mensions, however we focused on the ADD model in this thesis. ADD is a model suggested as a solution to the hierarchy problem, with extra dimensions that can be as large as micrometers in radius. The possibility of black hole formation is based on the model assumption of stronger gravity in distance scales of the order of the extra dimension radius R.

These black holes are predicted to radiate their energies to the brane in the form of Hawking radiation, which is a thermal, purely quantum process. As the black holes have masses of the order of $\sqrt{x_1 x_2 s}$, their Hawking temperature is O(100) TeV and the corresponding lifetimes are about 10^{-26}s. In other words they are expected to evaporate very quickly.

What determines the signature of black hole decay is the Hawking radiation and the Planck stage of the decay. Hawking radiation is democratic in the sense that all SM particles are emit-

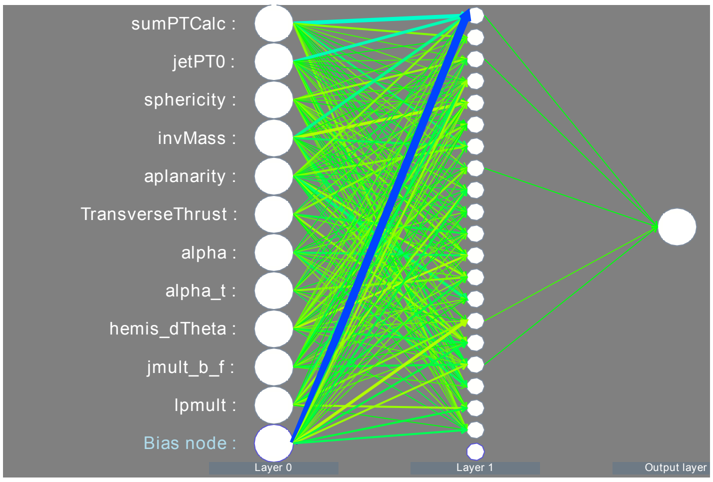

Figure 5.28: Structure of the neural network used in this analysis.

ted with almost equal probability. This means that BH decays are mostly hadronic because quarks are the most probable particle type to be emitted. Because of the Lorentz contraction of the z-direction, most of the energy is radiated to the transverse plane.

The SM backgrounds for black hole events are the W,Z,top+jets, and QCD dijet/multijet events. Among these backgrounds we found that high E_T QCD events are the ones that resemble BH events the most from the experimental point of view.

By making a trigger study using the reconstructed physics objects, we have shown that an HT trigger operating at 1500 GeV would have about a 95% efficiency for the signal events, while having about 15% for the most important background, the 6-jet QCD processes.

We have studied a number of variables in order to characterize black hole decays and to distinguish them from the SM backgrounds. We observed that the lepton multiplicity and the P_T sum of all particles in the event are the most powerful variables for rejecting backgrounds with an acceptable efficiency for the signal events. These variables are also convenient to be used at the beginning of the 14 TeV runs, because of their simplicity and robustness.

Our cut-based study aimed at early 14 TeV runs showed that for an integrated luminosity of 100/pb, we achieve significance values of the order of 100 for the low-mass, high cross-section parameter points. For the less accessible high mass points this luminosity is not enough for discovery.

In order to investigate the possible enhancements of multivariate methods to selection of low cross-section points, we studied the method of artificial neural networks. Our study showed that a MLP type neural network with a single hidden layer of $N + 20$ neurons (where N is the number of input variables) might result in up-to three times higher significance values when compared to cut-based selection. Among the two parameter points the network hasn't been trained for, one had a small drop in the significance, while the other had an increase when the ANN selection is used. We conclude that ANNs are a powerful method to enhance the selection efficiencies.

Black hole production and decay at the LHC would have a number of important consequences. First consequence would be the discovery of the Hawking radiation, and the possibility to study this mechanism in detail. Black hole decays would also allow physicists to study general relativity and quantum gravity right in the lab, because black hole decays carry significant information about the nature of spacetime. Black holes are also expected to behave as particle factories because of the democratic nature of the Hawking radiation mechanism. The most important negative consequence of black hole production is rendering probing the matter at smaller distance scales no longer possible, because all the higher energy particle collisions needed to probe smaller distance scales will end up in black holes.

In conclusion, if produced, quantum black holes will have a rather interesting phenomenology that will greatly help us learn much more about the nature of space-time.

REFERENCES

[1] Standard Model, http://en.wikipedia.org/wiki/standard_model, last accessed on 9 September 2011.

[2] S. Chatrchyan et al. Measurement of WW Production and Search for the Higgs Boson in pp Collisions at sqrt(s) = 7 TeV. Phys. Lett., B699:25–47, 2011.

[3] G. Aad et al. Limits on the production of the Standard Model Higgs Boson in pp collisions at sqrt(s) =7 TeV with the ATLAS detector. 2011.

[4] I. C. Brock. Physics of and with Leptons WS 05/06 (Lecture Notes).

[5] S. P. Martin. A Supersymmetry Primer. 1997.

[6] N. Arkani-Hamed, S. Dimopoulos, and G. R. Dvali. The hierarchy problem and new dimensions at a millimeter. Phys. Lett., B429:263–272, 1998.

[7] I. Antoniadis, N. Arkani-Hamed, S. Dimopoulos, and G. R. Dvali. New dimensions at a millimeter to a fermi and superstrings at a tev. Phys. Lett., B436:257–263, 1998.

[8] L. Randall and R. Sundrum. A large mass hierarchy from a small extra dimension. Phys. Rev. Lett., 83:3370–3373, 1999.

[9] L. Randall and R. Sundrum. An alternative to compactification. Phys. Rev. Lett., 83:4690–4693, 1999.

[10] M. Shifman. LARGE EXTRA DIMENSIONS: Becoming acquainted with an alternative paradigm. Int. J. Mod. Phys., A25:199–225, 2010.

[11] T. Kaluza. Zum unitätsproblem in der physik. Sitzungsber. Preuss. Akad. Wiss., 1921:966–972, 1921. Zum Unitätsproblem in der Physik.

[12] O. Klein. Quantentheorie und fünfdimensionale relativitätstheorie. Z. Phys., 37:895–906, 1926.

[13] R. Rattazzi. Cargese lectures on extra dimensions. oai:cds.cern.ch:968780. Particle Phys. Cosmology: the Interface, (hep-ph/0607055. CERN-PH-TH-2006-029):461–517. 56 p, Jul 2006.

[14] G. D. Kribs. Phenomenology of extra dimensions. 2006.

[15] N. Arkani-Hamed, S. Dimopoulos, and G. R. Dvali. The hierarchy problem and new dimensions at a millimeter. Phys. Lett., B429:263–272, 1998.

[16] N. Arkani-Hamed, S. Dimopoulos, and G. R. Dvali. Phenomenology, astrophysics and cosmology of theories with sub-millimeter dimensions and tev scale quantum gravity. Phys. Rev., D59:086004, 1999.

[17] D. M. Weld, J. Xia, B. Cabrera, and A. Kapitulnik. A New Apparatus for Detecting Micron-Scale Deviations from Newtonian Gravity. Phys. Rev., D77:062006, 2008.

[18] S. Chatrchyan et al. Search for New Physics with a Mono-Jet and Missing Transverse Energy in pp Collisions at sqrt(s) = 7 TeV. 2011.

[19] G. Aad et al. Search for new phenomena with the monojet and missing transverse momentum signature using the ATLAS detector in sqrt(s) = 7 TeV proton-proton collisions. 2011.

[20] S. Dimopoulos and G. Landsberg. Black holes at the lhc. Phys. Rev. Lett., 87:161602, 2001.

[21] P. T. Chrusciel. 'No hair' theorems: Folklore, conjectures, results. Contemp. Math., 170:23–49, 1994.

[22] S. M. Carroll. Lecture notes on general relativity. 1997.

[23] P. K. Townsend. Black holes. 1997.

[24] S. Carroll. Spacetime and Geometry: An Introduction to General Relativity. Benjamin Cummings, 2003.

[25] P. C. Argyres, S. Dimopoulos, and J. March-Russell. Black holes and sub-millimeter dimensions. Phys. Lett., B441:96–104, 1998.

[26] P. Kanti. Black holes in theories with large extra dimensions: a review. International Journal of Modern Physics A, 19:4899, 2004.

[27] S. B. Giddings and S. D. Thomas. High energy colliders as black hole factories: The end of short distance physics. Phys. Rev., D65:056010, 2002.

[28] J. L. Feng and A. D. Shapere. Black hole production by cosmic rays. Phys. Rev. Lett., 88:021303, 2002.

[29] L. Anchordoqui and H. Goldberg. Experimental signature for black hole production in neutrino air showers. Phys. Rev., D65:047502, 2002.

[30] J. Alvarez-Muniz, J. L. Feng, F. Halzen, T. Han, and D. Hooper. Detecting microscopic black holes with neutrino telescopes. Phys. Rev., D65:124015, 2002.

[31] M. Kowalski, A. Ringwald, and H. Tu. Black holes at neutrino telescopes. Phys. Lett., B529:1–9, 2002.

[32] S. W. Hawking. Particle creation by black holes. Commun. Math. Phys., 43:199–220, 1975.

[33] S. Hossenfelder. What black holes can teach us. 2004.

[34] H. Stoecker. Stable TeV - black hole remnants at the LHC: Discovery through di-jet suppression, mono-jet emission and a supersonic boom in the quark-gluon plasma. Int. J. Mod. Phys., D16:185–205, 2007.

[35] J. R. Ellis, G. Giudice, M. L. Mangano, I. Tkachev, and U. Wiedemann. Review of the Safety of LHC Collisions. J. Phys., G35:115004, 2008.

[36] S. B. Giddings and M. L. Mangano. Astrophysical implications of hypothetical stable TeV- scale black holes. Phys. Rev., D78:035009, 2008.

[37] G. 't Hooft. The scattering matrix approach for the quantum black hole: An overview. Int. J. Mod. Phys., A11:4623–4688, 1996.

[38] V. Khachatryan et al. Search for Microscopic Black Hole Signatures at the Large Hadron Collider. Phys. Lett., B697:434–453, 2011.

[39] O. S. Bruning, P. Collier, P. Lebrun, S. Myers, R. Ostojic, J. Poole, and P. Proudlock. LHC Design Report. CERN, Geneva, 2004.

[40] L. Evans and P. Bryant. Lhc machine. Journal of Instrumentation, 3(08):S08001, 2008.

[41] LHC Luminosity Plots for the 2011 Proton Run,
http://lpc.web.cern.ch/lpc/lumiplots.htm,
accessed on 26/07/2011.

[42] CMS Luminosity Collision Data,
https://twiki.cern.ch/twiki/bin/view/cmspublic/lumipublicresults,
accessed on 26/07/2011.

[43] G. L. Bayatian et al. CMS physics: Technical design report. CERN-LHCC-2006-001.

[44] C. M. Harris and P. Kanti. Hawking radiation from a (4+n)-dimensional black hole: Exact results for the Schwarzschild phase. JHEP, 10:014, 2003.

[45] C. M. Harris, P. Richardson, and B. R. Webber. Charybdis: A black hole event generator. JHEP, 0308:033, 2003.

[46] T. Sjostrand, S. Mrenna, and P. Skands. PYTHIA 6.4 physics and manual. JHEP, 05:026, 2006.

[47] C. D. J. et al. The new CMS data model and framework. CHEP06 Conference Proceedings, 2007.

[48] H. Yoshino and V. S. Rychkov. Improved analysis of black hole formation in high-energy particle collisions. Phys. Rev., D71:104028, 2005.

[49] S. Wynhoff. Famos: A dynamically configurable system for fast simulation and reconstruction for cms. ECONF, C0303241:THJT004, 2003.

[50] S. Agostinelli. et. al. GEANT4-A Simulation Toolkit, Nuclear Instruments and Methods in Physics Research a 506 (2003) 250-303; J. Allison et al., GEANT4 Developments and Applications, IEEE Transactions on Nuclear Science 53 No. 1 (2006) 270-278.

[51] S. Chatrchyan et al. Determination of jet energy calibration and transverse momentum resolution in cms. oai:cds.cern.ch:1369992. Jul 2011.

[52] F. Caravaglios, M. L. Mangano, M. Moretti, and R. Pittau. A new approach to multi-jet calculations in hadron collisions. Nucl. Phys., B539:215–232, 1999.

[53] M. L. Mangano, M. Moretti, and R. Pittau. Multijet matrix elements and shower evolution in hadronic collisions: W b anti-b + (n)jets as a case study. Nucl. Phys., B632:343–362, 2002.

[54] M. L. Mangano, M. Moretti, F. Piccinini, R. Pittau, and A. D. Polosa. Alpgen, a generator for hard multiparton processes in hadronic collisions. JHEP, 07:001, 2003.

[55] G. Fox and S. Wolfram. Event shapes in e^+e^- annihilation. Nuclear Physics B, 149:413, Oct. 1979.

[56] R. S. S. Brandt, Ch. Peyrou and A. Wroblewski. Phys. Lett., 12:57, 1964.

[57] E. Fahri. Phys. Rev. Lett., 39:1587, 1977.

[58] G. Dissertori, F. Moortgat, and M. A. Weber. Hadronic event-shape variables at cms, 2008.

[59] J. Pumplin et al. New generation of parton distributions with uncertainties from global QCD analysis. JHEP, 07:012, 2002.

[60] M. R. Whalley, D. Bourilkov, and R. C. Group. The Les Houches Accord PDFs (LHAPDF) and Lhaglue. 2005.

[61] P. M. Nadolsky and Z. Sullivan. PDF uncertainties in W H production at Tevatron. 2001.

[62] Z. Sullivan. Fully differential W' production and decay at next-to- leading order in QCD. Phys. Rev., D66:075011, 2002.

[63] C. Broyden. The Convergence of a Class of Double-rank Minimization Algorithms. J. Inst. of Math. and App., 6:76, 1970.

[64] R. Fletcher. A New Approach to Variable Metric Algorithms. Computer J., 13:317, 1970.

[65] D. Goldfarb. A Family of Variable Metric Updates Derived by Variational Means. Math. Comp., 24:23, 1970.

[66] D. Shannon. Conditioning of Quasi-Newton Methods for Function Minimization. Math. Comp., 24:647, 1970.

[67] A. Hoecker, P. Speckmayer, J. Stelzer, J. Therhaag, E. von Toerne, and H. Voss. TMVA: Toolkit for Multivariate Data Analysis. PoS, ACAT:040, 2007.

CURRICULUM VITAE

PERSONEL INFORMATION

Surname, Name	: Gamsızkan, Halil
Date and Place of Birth	: 7 September 1976, Eskişehir
Nationality	: Turkish (T.C.)
e-mail	: halilgamsizkan@gmail.com

EDUCATION

Degree	Institution	Year of Graduation
Ph.D.	METU, Physics	2011
M.Sc.	METU, Physics	2003
BSc.	METU, Physics	1999

WORK EXPERIENCE

Year	Place	Enrollment
1999-2011	METU, Physics	Research Assistant

FOREIGN LANGUAGES

English

PUBLICATIONS

1. The CMS Collaboration. "CMS Physics Technical Design Report, Volume II: Physics Performance". Journal of Physics G: Nuclear and Particle Physics, v34-6, p995, 2007.

2. The CMS Collaboration. "Search for Microscopic Black Hole Signatures at the Large Hadron Collider", 2010, 1012.3375, arXiv, hep-ex

3. The CMS Collaboration. "Performance of the CMS Hadron Calorimeter with Cosmic Ray Muons and LHC Beam Data", JINST, vol5, 2010, pages T03012

4. The CMS Collaboration, "Commissioning of the CMS Experiment and the Cosmic Run at Four Tesla", JINST, vol5, 2010, pages T03001